Development of ultracompact, high-sensitivity, space-based instrumentation for far-infrared and submillimeter astronomy

by

Giuseppe Cataldo

B.S., Politecnico di Milano (2007)
M.S., Politecnico di Milano (2010)
M.S., Politecnico di Torino (2010)
M.S., ISAE-SUPAERO (2010)

Submitted to the Department of Aeronautics and Astronautics
in Partial Fulfillment of the Requirements for the Degree of

Doctor of Philosophy

at the

Massachusetts Institute of Technology

June 2015

Signature of Author ..... Signature redacted
Department of Aeronautics and Astronautics
March 5, 2015

Certified by ..... Signature redacted
Jeffrey A. Hoffman
Professor of the Practice of Aeronautics and Astronautics
Thesis Supervisor

Certified by ..... Signature redacted
Kerri L. Cahoy
Assistant Professor of Aeronautics and Astronautics

Certified by ..... Signature redacted
Samuel H. Moseley
Senior Astrophysicist, NASA

Certified by ..... Signature redacted
Edward J. Wollack
Research Astrophysicist, NASA

Accepted by ..... Signature redacted
Paulo C. Lozano
Associate Professor of Aeronautics and Astronuatics
Chair, Graduate Program Committee

Development of ultracompact, high-sensitivity, space-based instrumentation for far-infrared and submillimeter astronomy

by

Giuseppe Cataldo

Submitted to the Department of Aeronautics and Astronautics
on March 30, 2015 in Partial Fulfillment of the
Requirements for the Degree of Doctor of Philosophy in
Aeronautics and Astronautics

ABSTRACT

Far-infrared (IR) and submillimeter (15 μm–1 mm) spectroscopy provides a powerful tool to probe a wide range of environments in the universe. In the past thirty years, many space-based observatories have opened the far-IR window to the universe, providing unique insights into several astrophysical processes related to the evolution of the early universe. Nonetheless, the size and cost of the cryogenic spectrometers required to carry out such measurements have been a limiting factor in our ability to fully explore this rich spectral region and answer questions regarding the very first moments of the universe. Among the key technologies required to enable this science are ultra-low-noise, far-IR, direct-detection spectrometers.

In this thesis, Micro-Spec (μ-Spec) is proposed as a novel technology concept to enable a large range of flight missions that would otherwise be challenging due to the large size of current instruments and the required spectral resolution and sensitivity. μ-Spec is a direct-detection spectrometer operating in the 450–1000–μm regime, which employs superconducting microstrip transmission lines to achieve a resolution ($\mathcal{R} \geq 1200$) and be integrated on a $\sim$ 10–cm^2 silicon chip.

The objective of this thesis is to explore the feasibility of the μ-Spec technology. First, analytical models are developed for the dielectric function of silicon compounds to be used as substrates in the transmission lines. These materials represent the ultimate source of loss in the system. The models are used to analyze laboratory spectral data of silicon nitride and oxide films and provide information on the loss within a 4% accuracy. A design methodology is then developed for the spectrometer diffractive region given specific requirements on size and spectral range. This methodology is used to explore the design space and find the optimal solutions that maximize the instrument efficiency and minimize the phase error on the focal plane. Five designs are described with different requirements and performance. Finally, analysis and calibration techniques are developed to study the properties of the superconducting materials employed in the transmission lines and detectors. These techniques are applied to laboratory data of molybdenum nitride and niobium to extract their quality factors and kinetic inductance fraction within a 1% accuracy.

Thesis Supervisor and Committee Chair:
Jeffrey A. Hoffman, Ph.D.
Professor of the Practice of Aeronautics and Astronautics
MIT Department of Aeronautics and Astronautics

Thesis Committee Member:
Kerri L. Cahoy, Ph.D.
Assistant Professor of Aeronautics and Astronautics
MIT Department of Aeronautics and Astronautics

Thesis Committee Member:
Samuel H. Moseley, Ph.D.
Senior Astrophysicist
NASA Goddard Space Flight Center

Thesis Committee Member:
Edward J. Wollack, Ph.D.
Research Astrophysicist
NASA Goddard Space Flight Center

Thesis Reader:
Robert Simcoe, Ph.D.
Associate Professor of Physics
MIT Astrophysics Division

Thesis Reader:
Omid Noroozian, Ph.D.
NASA Postdoctoral Program Fellow
NASA Goddard Space Flight Center

Acknowledgments

This thesis is dedicated to my parents, whose unconditional love and sacrifices have ultimately allowed me to achieve this and other important milestones throughout my life. Infinite thanks go to my wife-to-be, María, for taking on all the challenges of a long-distance relationship during my two years in Cambridge and supporting my endeavors through the end.

I enjoyed being part of the Man Vehicle Lab and Space Systems Lab, many of whose members shared with me overnight or weekend efforts always with a smile on their face. My involvement with the MIT community was also a unique way to develop new friendships, from being resident and secretary in The Warehouse and a member of the MIT Tech Catholic Community to sailing, skiing and scuba-diving.

Special thanks to my advisor, Prof. Jeff Hoffman, for his guidance, kindliness and constant support and to my co-advisors at NASA, Dr. Harvey Moseley and Dr. Ed Wollack, for all the helpful advice provided along these years and for pushing me to always learn more and think out of the box.

This work was supported and funded by the Massachusetts Institute of Technology's Arthur Gelb fellowship and the National Aeronautics and Space Administration's Research Opportunities in Space and Earth Sciences (ROSES) and Astronomy and Physics Research and Analysis (APRA) programs.

Table of contents

List of Figures

List of Tables

Chapter 1

Introduction

Since time immemorial man has probed the mysteries of the universe in an attempt to discover its governing laws and learn the origins of mankind. From the Phoenicians to the Egyptians to the Greeks, questions regarding how the Universe came to be, how the stars move in the sky, how life on Earth developed always drew the attention of early astronomers, mathematicians, philosophers, sailors, and engineers. A prominent role in providing answers to these and many other questions has always been played by observation. The first telescope used to study the heavens was pointed up to the sky by Galileo Galilei in 1609. It was a 92.7-cm-long refractor which collected light with a glass lens. From there followed a cascade of discoveries which began unraveling the mysteries of the universe. However, the human eye is only sensitive to a narrow range of wavelengths called visible light.

There exist countless astronomical objects in the universe such as galaxies, stars, comets or asteroids, to name a few, which emit radiation at wavelengths that the unaided eye cannot see. This has spurred the development of new tools that would enable the detection of such objects otherwise invisible to us. In particular, the infrared region of the electromagnetic spectrum proves a powerful area of research for studying the origins and evolution of the universe.

There exist several categorizations of the infrared (IR) spectrum [1,2, and others], but the one shown in Fig. 1.1 proves useful in that it is based on a combination of the atmospheric transmittance windows (i.e., the wavelengths regions in which the infrared radiation is best

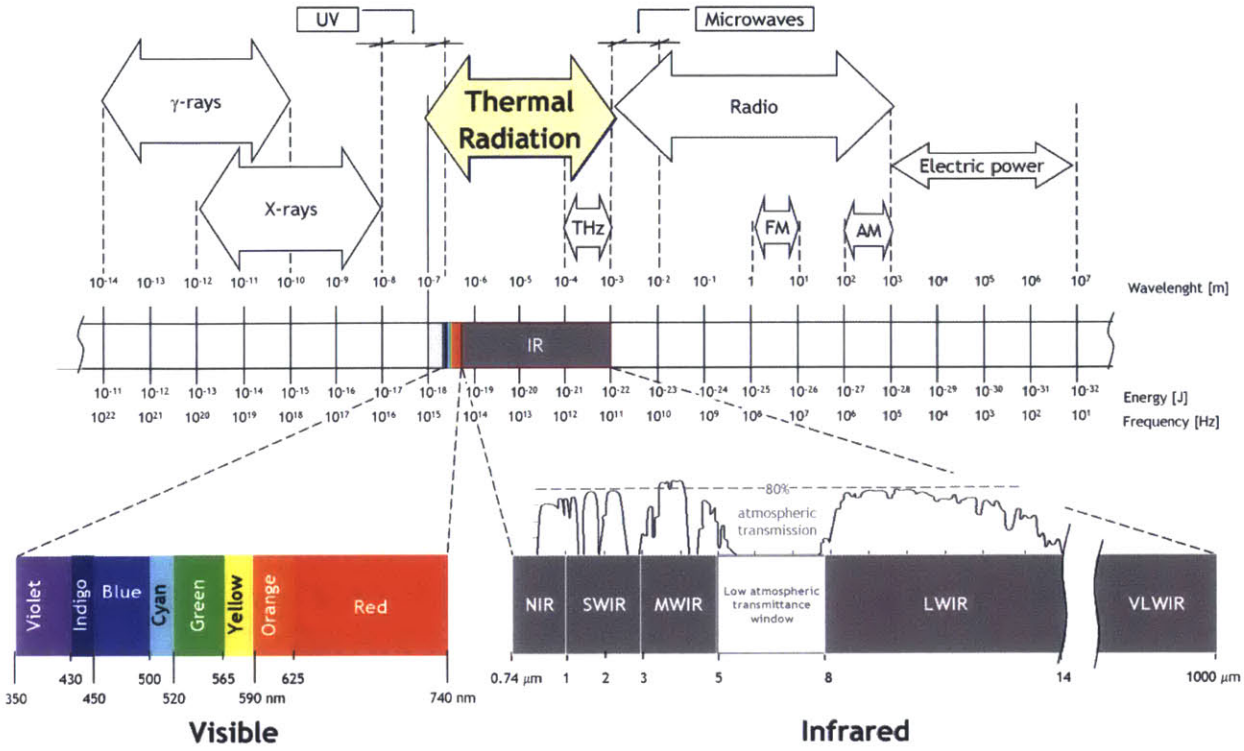

Figure 1.1: The entire electromagnetic spectrum highlighting the infrared band located between the visible and radio waves. The Earth atmosphere's transmission bands in the infrared are also displayed. Adapted from [3].

transmitted through the Earth's atmosphere), the detector materials used to build infrared sensors, and their main applications. According to [1], the IR band can be subdivided into five regions. The Near Infrared (NIR) band is mostly used in fiber-optic telecommunication systems, where silica (SiO_2) provides a low attenuation loss medium for the near infrared. The Short Wave Infrared (SWIR) band allows for long-distance telecommunications using combinations of detector materials. The Medium Wavelength Infrared (MWIR) and the Long Wavelength Infrared (LWIR) bands find applications in infrared thermography for military or civil applications, e.g. target signature identification, surveillance, non-destructive evaluation, etc. The MWIR band is preferred when inspecting high-temperature objects, while the LWIR band becomes more useful when working with near-room-temperature objects. Finally, the Very Long Wavelength Infrared (VLWIR) or Far Infrared (FIR) band is used in various kinds of spectroscopy, including astronomical spectroscopy.

1.1 The importance of infrared astronomy and the need for space telescopes

The universe is in a state of constant expansion in which every wavelength traveling through it is stretched. In particular, much of the visible and ultraviolet light released billions of years ago has been stretched into the far-infrared region of the electromagnetic spectrum, a process known as *redshift* [4]. As a consequence, the very early steps of the universe can be studied by looking at very distant celestial bodies in the far-infrared and microwave regions of the electromagnetic spectrum (Fig. 1.2).

Many of the objects of interest to astronomers and astrophysicists, such as stars and planets in the early stages of formation and the powerful cores of active galaxies [6, 7], emit most strongly in the infrared. Astronomical dust has been found in our solar system, around nearby stars with debris disks, in star formation regions and even in far-distant galaxies. A diffuse glow of infrared radiation also permeates our own Milky Way galaxy. This is generated by dust grains which absorb starlight and then reradiate that energy at infrared wavelengths [8–20].

It is in such cold and dusty environments that stellar formation processes often take place [21, 22]. While planet formation processes are still under study (e.g., [23–25]), according to the solar nebula theory and planetesimal hypothesis [26], planets are formed during the collapse of a nebula into a thin disk of gas and dust. A protostar forms at the core, surrounded by a rotating protoplanetary disk. Through accretion, dust particles in the disk steadily accumulate mass to form ever-larger bodies. Local concentrations of mass known as planetesimals form and accelerate the accretion process by drawing in additional material by their gravitational attraction. These concentrations become ever denser until they collapse inward under gravity to form protoplanets.

Dust is primarily formed in the quiescent outflows of asymptotic giant branch (AGB) stars [1] and in the stellar material explosively ejected in core-collapse supernovae (Fig. 1.3).

[1] In an AGB star, the core is so hot and its gravitational attraction on its outermost layers is so weak that those layers are expelled in a stellar wind. As each layer blows away, a hotter one is exposed and the stellar wind becomes stronger. These newly formed, fast winds slam into the old, slow winds that are still moving away from the star out in space. The process, thus, continues as more layers are exposed and ejected. These

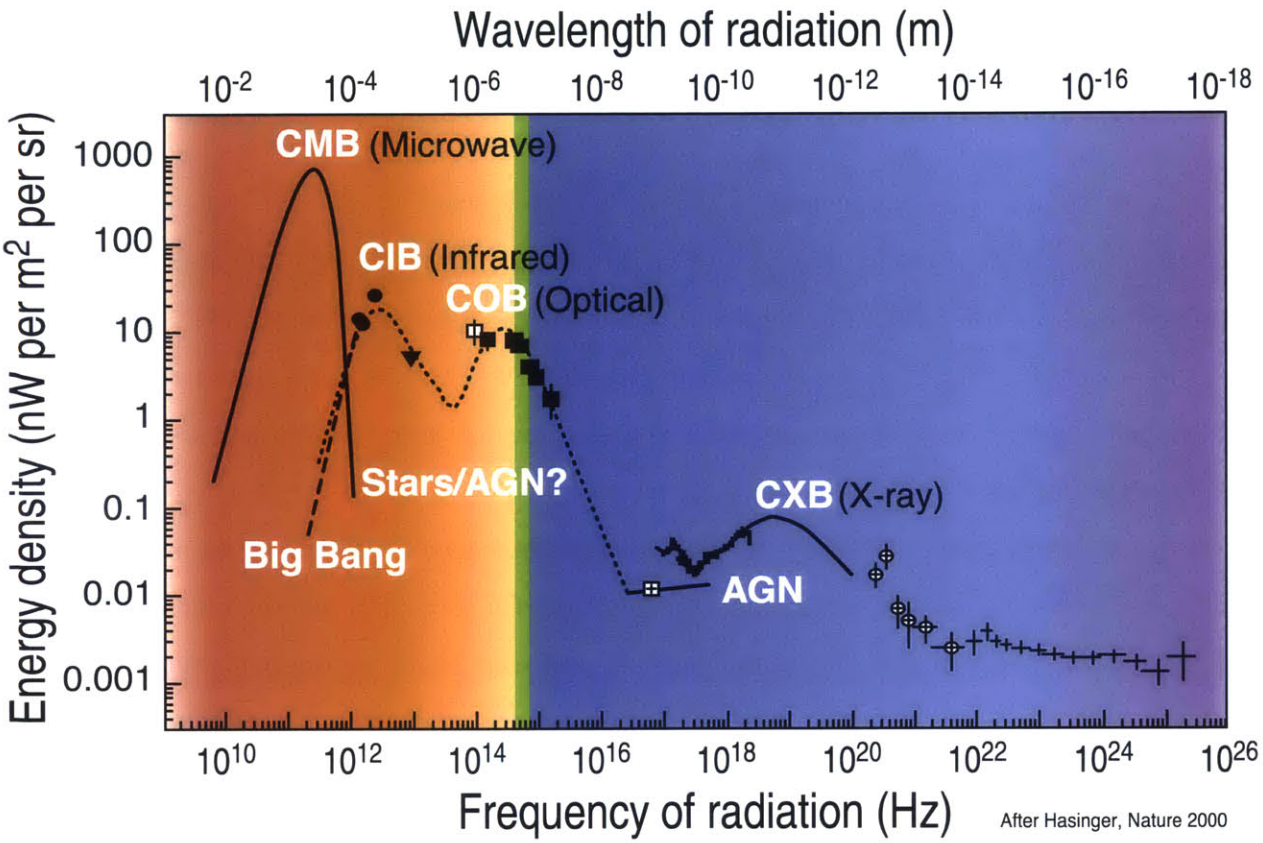

Figure 1.2: This figure captures the sense of where the energy can be found in the universe. Cosmic Microwave Background (CMB) is a form of electromagnetic radiation left over from an early stage in the creation of the universe. It is not associated with any star, galaxy, or other object, but it shows itself as a faint background glow nearly exactly the same in all directions and is largely unpolarized. It represents the main contribution to the spectrum. The CMB is well characterized below 1 THz as a thermal black-body spectrum at a temperature of ≈ 2.725 K, thus the spectrum peaks in the microwave range frequency of 160.2 GHz, corresponding to a 1.9 mm wavelength. Other forms of cosmic backgrounds are found in the infrared (CIB) and optical range (COB), which are due to stars and perhaps active galactic nuclei (AGN). The latter would be responsible for the cosmic background in the X-ray band (CXB), where the energy density is much lower. The error bars on the CMB curve are not shown as they are imperceptible on the figure presented; however, they are visible on the other curves, although they remain very small relative to other objects. Adapted from [5].

Dust that forms in the explosive ejecta of a supernova is subjected to the harsh physical environment of the young remnant, such as heating by X-rays and cosmic rays. The high velocities of this material as it is injected into the interstellar medium (ISM) also lead to reverse shocks that further process the dust grains. Standard models of interstellar dust assume a mixture of silicates, graphite (or amorphous carbon), and polycyclic aromatic hydrocarbons (PAHs)

collisions produce dense shells of gas, some of which cool to form dust [28].

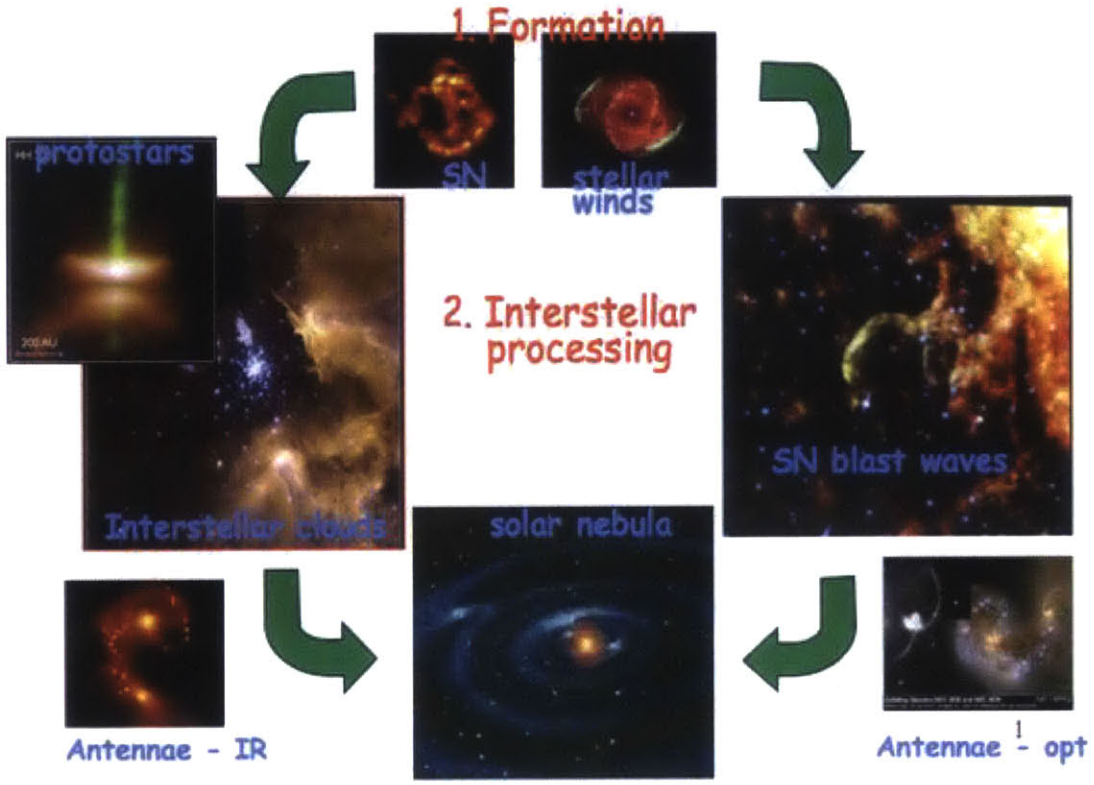

Figure 1.3: Dust forms in supernovae and in the outflows from stars, particularly evolved ones. From these sources, through the action of winds and shocks in the interstellar and circumstellar medium, as well as transportation and diffusion processes generated by turbulence, dust becomes an important component of the interstellar clouds in which stars form. Dust can also find itself in the disk around a young star, where it can coalesce with other grains to form planetesimals, and ultimately planets such as Earth. Adapted from [27].

to simultaneously fit the average interstellar extinction, thermal infrared (IR) emission, and elemental abundance constraints [29]. Furthermore, silicates and carbonaceous-type particles have varying degrees of disorder, thus acting as an archaeological record of the environment where they form and evolve [27, 30].

Dust shields sources from our view at optical wavelengths (Fig. 1.4), because dust particles are very effective at absorbing and scattering visible light, in accordance with Kirchhoff's law ("A good absorber is a good emitter") [31]. Extinction (scattering + absorption) of visible light increases approximately linearly with decreasing wavelength [9]. As a consequence, interstellar dust extinguishes blue light more efficiently than red light (Fig. 1.1), and starlight transmitted through dust is therefore reddened, similarly to what molecular and particulate constituents of the Earth's atmosphere do. Because extinction is a particle-size

Figure 1.4: New stars forming in the Carina nebula can be seen in the infrared (right) behind the pillar of gas and dust that appears in the visible-light image on the left. *Credits: NASA, ESA, and the Hubble SM4 ERO Team.*

dependent phenomenon, it was possible to infer that dust grains are small compared with optical wavelengths to be able to interact with the electromagnetic radiation and reprocess short-wavelength light to longer wavelengths [6]. Laboratory transmission measurements taken in the far-to-mid-infrared regime between 5.56 µm and 500 µm for SiO_x grains [32, 33] have allowed estimating the diameter of the particles (assumed to be spherical) to be 0.4 nm, comparable to that of the SiO_4 tetrahedra found in [34] and equal to 0.5 nm. This grain size is the same order of magnitude as predicted by most models explaining interstellar dust grain size distribution [35, and references therein].

The uniqueness of infrared instruments lies therefore in the capability of infrared wavelengths to detect and observe the emission of these dust particles, thereby enabling the observation of the above-mentioned phenomena otherwise impossible with visible light. As a consequence, infrared telescopes are crucial for understanding the distant young Universe. NASA and the European Space Agency (ESA) have recognized the importance of infrared observations, as demonstrated by infrared missions such as NASA's *Spitzer Space Telescope* [36], *Stratospheric Observatory For Infrared Astronomy* (SOFIA) [37], *James Webb Space Tele-*

scope (JWST) [38], and ESA's *Infrared Space Observatory* (ISO) [39] and *Herschel* [40]. The goal of these current and future missions is to explore a wide range of questions related to cosmology and provide the most detailed and highest quality far-infrared and submillimeter spectra of astrophysical sources yet achieved.

The importance of space-borne infrared telescopes resides also in the behavior of the Earth's atmosphere, which blocks many wavelengths of radiation and lets others through, due to its absorption bands (Fig. 1.1). For example, most infrared radiation is blocked out, except for a few narrow wavelength ranges that make it through to ground-based infrared telescopes. The atmosphere causes another problem: it itself radiates strongly in the infrared, often emitting more infrared radiation than the objects in space being observed. For these reasons, ground-based infrared observatories are usually located in deserts or plateaus, where the air is dry and the atmosphere relatively calm, or near the summits of high mountains, where it is possible to get above as much of the atmosphere as possible. Some examples in this category are the Atacama Large Millimeter Array (ALMA) [41], the Submillimeter Telescope (formerly know as the Heinrich Hertz Telescope) [42], the Submillimeter Array (SMA) [43], the South Pole Telescope (SPT) [44], and the Keck Array [45]. Telescopes in space, such as those mentioned above, and sometimes balloons flown to the high atmosphere (e.g., [46–49]) avoid all these problems and provide scientists with infrared spectra whose high (e.g., $\gtrsim 1200$) resolution enables the exploration of the physical processes in the early universe (redshift $z > 8$).

Chapter 2

Problem statement and objectives

2.1 Existing gaps and future needs

As described in Chapter 1, far-infrared and submillimeter (15 μm–1 mm, or equivalently 20 THz–300 GHz) spectroscopy provides a powerful tool to probe a wide range of environments in the universe. In the past thirty years, many space-based observatories (e.g., [36,39, 40]) have opened the far-infrared window to the universe, revealing rich line and continuum spectra from objects ranging from interplanetary dust particles to major galactic mergers and young galaxies in the early universe. Discoveries made by these observatories have provided unique insights into physical processes leading to the evolution of the universe and its contents. This information is encoded in a wide range of molecular lines and fine-structure lines. The fine-structure lines of abundant elements such as carbon, nitrogen, and oxygen are seen in the 50–200–μm rest frame, but with a spectrometer operating in the far-IR/sub-mm they can be observed in star-forming galaxies out to redshifts $z > 5$. This therefore enables tracing the obscure star formation and AGN activity into the high-redshift (and thus older) universe. Nonetheless, a number of questions remain to be answered. For example:

- What are the first galaxies? Where did they form?
- When and how did reionization occur? What sources caused it?
- How did the heavy elements form?

- What physical processes determine galaxy formation?
- How does the environment affect star formation and vice versa?
- How do protoplanetary systems form?
- What are the life cycles of gas and dust?
- How do planets form? How are habitable zones established?

The National Academies' 2010 Decadal Survey report, *New Worlds, New Horizons in Astronomy and Astrophysics* [50], recommended a suite of missions and technology development programs aimed to further our understanding in the following three areas:

- Cosmic dawn: searching for the first stars, galaxies, and black holes
- New worlds: seeking nearby, habitable planets
- Physics of the universe: understanding scientific principles

Some of the specific missions that will probe in more detail all of the above-mentioned processes might be the Wide-Field InfraRed Survey Telescope (WFIRST) [51], NASA's Explorer Program [52], the US contribution to the Japanese Aerospace Exploration Agency (JAXA) SPace Infrared telescope for Cosmology and Astrophysics (SPICA) mission [53], as well as technology development programs for ultraviolet-optical-infrared (UVOIR) space capabilities and for studying the Epoch of Inflation. These far-IR missions will require technology development in the following areas: large, cryogenic far-IR telescopes; large-format, low-noise, as well as ultra-low-noise far-IR direct detectors; photon-counting far-IR detector arrays; interferometry for far-IR telescopes; and high-performance sub-kelvin coolers. Table 2.1 illustrates the requirements for each of these areas and their potential benefits to the astrophysics community, NASA, and the aerospace industry [54].

Table 2.1: Summary of astrophysics technology needs for the 2015-2035 frame and their benefits (Adapted from [54])

Technology	**Large, cryogenic, far-IR telescopes**	**Large-format, low-noise, far-IR direct detectors**	**Ultra-low-noise, far-IR direct detectors**	**Interferometry for far-IR telescopes**	**High-performance sub-kelvin coolers**	**Photon-counting far-IR detector arrays**
Requirements	Provide light gathering power to see the faintest targets. Provide spatial resolution to see the most detail and reduce source confusion. To achieve the ultimate sensitivity, their emission must be minimized, with operating temperatures as low as 4 K. Collecting areas on the order of 50 m^2.	Optimized for the very low photon backgrounds present in space. Arrays containing up to tens of thousands of pixels to take full advantage of the focal plane available on large cryogenic telescopes. Detector sensitivity required to achieve background-limited performance, using direct (incoherent) detectors to avoid quantum-limited sensitivity.	Optimized for the very low photon backgrounds present in space for spectroscopy. Arrays containing up to thousands of pixels to take full advantage of the spectral information content available. Detector sensitivity required to achieve background-limited performance, using direct (incoherent) detectors to avoid quantum-limited sensitivity.	Provide spatial resolution to see the most detail and reduce source confusion. Structurally connected or free-flying interferometric telescope systems required for far-future missions in far-IR. Telescopes operated at temperatures as low as 4 K.	Be compact, low-power, and lightweight to provide cooling for space flight conditions which require temperatures of operation in the order of tens of millikelvin.	High quantum efficiency and fast response time.
Benefits	Provide spatial resolution and sensitivity necessary to follow up on discoveries with current generation of space telescopes. Low-cost, lightweight, cryogenic optics.	Sensitivity reduces observing times from many hours to a few minutes ($\sim$ 100 times improvement). Array format increases areal coverage by 10 to 100 times. Overall mapping speed can increase by factors of thousands.	Sensitivity reduces observing times from many hours to a few minutes ($\sim$ 100 times improvement). Overall mapping speed can increase by factors of thousands.	40-m baselines required to provide the spatial resolution needed to follow up on discoveries with current and next generation of space telescopes.	Enable the use of far-IR telescopes in the next decade and of certain X-ray detectors.	Missions will operate $\sim$ 100 times faster. Distant missions beyond the Zodiacal dust cloud [55, 56] will observe $>$ 10 times faster even in imaging applications.

The ability to fully explore this rich spectral region has been limited by the size, mass, power constraints, limitations in sensitivity, and cost of the cryogenic spectrometers required to carry out these measurements. The work presented in this thesis specifically addresses the need for **integrated, ultra-low-noise, far-IR, direct-detection spectrometers**, whose specific requirements are expected to be satisfied by Technology Readiness Level (TRL) 6-level technologies in the 2015-2035 frame [57]. These are shown in Table 2.2 and compared against the current state of the art.

Table 2.2: Summary of requirements for far-IR spectrometers and detector arrays and comparison with current state of the art [57]

Metric	**State of the art**	**Requirements**
Wavelength, λ	250–700 μm	220–2000 μm
Noise Equivalent Power, NEP	$\sim 10^{-18}$ W/$\sqrt{\text{Hz}}$	$< 10^{-20}$ W/$\sqrt{\text{Hz}}$
Resolving power, $\mathcal{R}$	≥ 100	≥ 1200
Detective quantum efficiency, DQE	$\sim 15\%$	$> 90\%$
Temperature, T	< 1 K	< 0.05 K
Time constant, τ	100 ms	< 10 ms

In Table 2.2, the required wavelength range is dictated by the type of science discussed in Chapter 1 and needed to answer the cosmological questions posed at the beginning of this section: high-redshift galaxy evolution, physical conditions of the interstellar medium in normal and star-forming galaxies across cosmic time, study of elemental abundances, etc. [50].

The Noise Equivalent Power (NEP) is a measure of the sensitivity of a photodetector or detector system and is defined as the signal power that gives a signal-to-noise ratio (SNR) of 1 in an output bandwidth $\Delta f = 1\,\text{Hz}$ [58]. An output bandwidth of 1 Hz is equivalent to half a second of integration time, $t = 1/(2\Delta f) = 0.5$ s, from the Nyquist-Shannon sampling theorem. A smaller NEP corresponds to a more sensitive detector. For example, a detector with a NEP of 10^{-18} W/$\sqrt{\text{Hz}}$ can detect a signal power of 1 attowatt (aW) with a SNR of 1 after one half second of averaging. The SNR improves as the square root of the averaging time, and hence the SNR in this example can be improved to 10 by averaging for 50 seconds. The NEP values shown in Table 2.2 are determined by the requirement to be background-limited and not detector-limited, that is, the noise thermally generated by the detectors must be lower than that presented by the astronomically observed background flux. This is defined

as background-limited performance (BLIP). Because the far-IR/sub-mm wavelength range is mainly characterized by the cosmic microwave background (CMB, see Fig. 1.2) with a NEP on the order of 10^{-18} W/$\sqrt{\text{Hz}}$ [59], the detectors' BLIP is required to be lower than this.

The resolving power, $\mathcal{R}$, of a spectrometer is a measure of its ability to resolve spectral features and is defined as $\mathcal{R} = \lambda/\Delta\lambda$, where $\Delta\lambda$ is the smallest difference in wavelengths that can be distinguished at a wavelength λ. For example, with a resolving power of 1000 at a wavelength of 600 µm, a spectrometer can resolve features 0.6 µm apart. A resolving power greater than 1200, as shown in Table 2.2, is again imposed by the type of science previously described, and in particular by the need of resolving exoplanets around stars.

The quantum efficiency (QE) is the flux absorbed in the detector divided by the total flux incident on its surface and is a measure of a device's electrical sensitivity to light. Since the energy of a photon is inversely proportional to its wavelength, the QE is often measured over a range of different wavelengths to characterize a device's efficiency at each photon energy level. This definition of quantum efficiency, however, refers only to the fraction of incoming photons converted into a signal in the first stage of a detector. In fact, in an ideal scenario, the signal-to-noise ratio attained in a measurement is controlled entirely by the number of photons absorbed in the first stage. However, additional steps in the detection process can degrade the information present in the photon stream absorbed by the detector, either by losing signal or by adding noise. The detective quantum efficiency (DQE) describes this degradation in terms of the square of the ratio of the actually observed signal-to-noise ratio to the signal-to-noise ratio of the incoming photon stream [60, Ch. 1].

Cryogenic temperatures are necessary to achieve background-limited performance by reducing the telescope and instrument thermally-generated noise. For example, away from the galactic plane, the background would be determined by the CMB, associated with a temperature of $\approx$ 2.725 K, while in the galactic plane it would be dominated by the infrared emission of dust, as previously discussed (see Fig. 1.2). Cryogenic temperatures also allow for the use of superconducting materials with critical temperatures below 13 K (e.g., niobium and molybdenum nitride) and which are practical from an engineering standpoint.

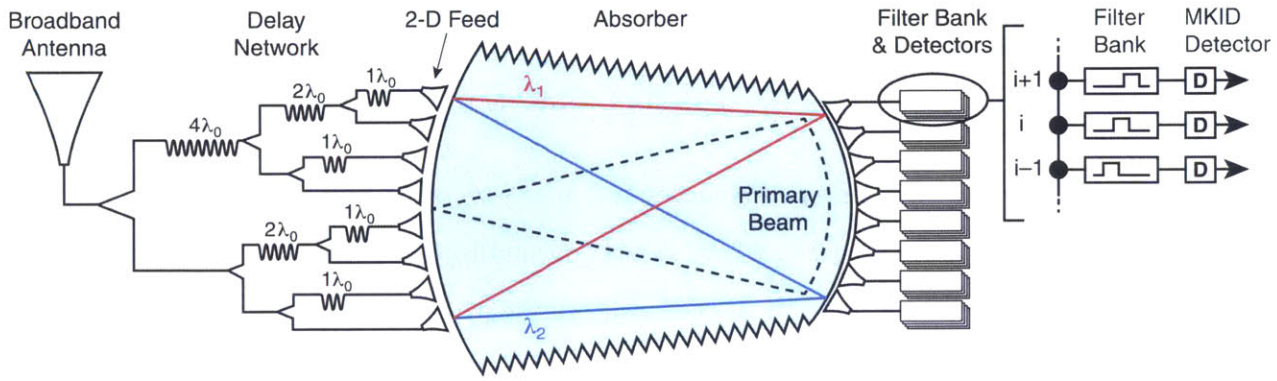

Figure 2.1: Layout of the μ-Spec module. The radiation collected by the telescope is coupled into the instrument using a broadband antenna (left). It is then transmitted through a low-loss superconducting transmission line to a divider and a phase delay network, which creates a retardation across the input to the multimode region (in light blue). The feed horns will radiate a converging circular wave, which will concentrate the power along the focal surface, with different wavelengths at different locations. The outputs are connected to a bank of order-sorting filters to disentangle the various orders [61].

Finally, the time constant, τ, represents the minimum interval of time over which the detector can distinguish changes in the photon arrival rate. A smaller time constant implies a detector with a faster response and ability to capture variations in the photon flux dynamics, as long as it does not impact the spacecraft performance (e.g., data rate, avionics, etc.).

2.2 Filling the gaps with Micro-Spec

To attain the goals outlined in Table 2.2 and fill in the gaps in the current state of the art, a high-performance integrated spectrometer module, μ-Spec, is being developed for use on space-borne telescopes such as SPICA [53] or high-altitude balloon-borne far-IR payloads.

More in detail (Fig. 2.1), μ-Spec operates in the 450–1000–μm (300–650–GHz) spectral range. In μ-Spec, the incoming radiation collected by the telescope is coupled to the spectrometer through a broadband dual-slot antenna used in conjunction with a hyper-hemispherical silicon lens and directed to a series of power splitters and a delay network made of superconducting microstrip transmission lines. The delay network creates a retardation across the input to a planar waveguide multimode region which has two internal phased arrays, one for transmitting and one for receiving the radiation as a function of wavelength. Ab-

sorber structures lining the multimode region terminate the power emitted into large angles or reflected from the receiver antenna array. The radiation is coupled to the multimode region via an array of planar feed structures, which concentrate the light along the focal surface with different wavelengths at different locations. The outputs are connected to a bank of order-sorting filters which terminate the power in an array of microwave kinetic inductance detectors (MKIDs) for detection. Read-out is done using conventional homodyne techniques and commercial field-programmable gate array (FPGA)-based software-defined radios (SDRs) [62, 63]. μ-Spec can be used in a modular fashion by assembling several identical spectrometers to perform multi-object spectrography.

One of the techniques adopted for μ-Spec is the use of monocrystalline silicon combined with superconducting materials, which reduce losses to a minimum. This provides a necessary prerequisite to attain the required background-limited sensitivity (NEP $< 10^{-20}$ W/$\sqrt{\text{Hz}}$) at a resolution $\mathcal{R} \geq 1200$, thus potentially making μ-Spec four orders of magnitude more sensitive than its most capable predecessors (Fig. 2.2).

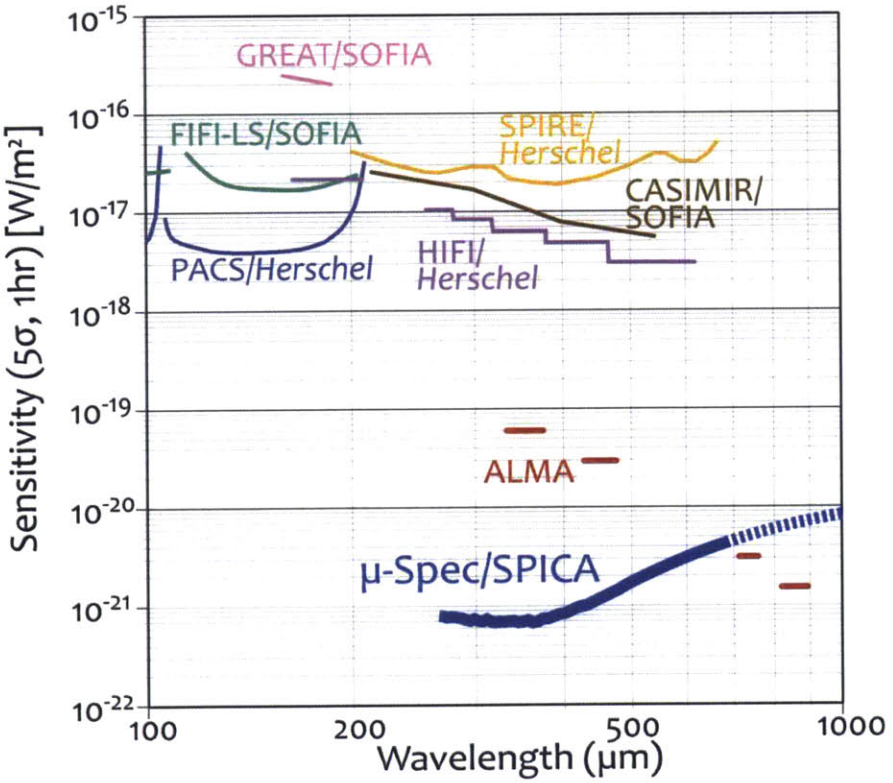

Figure 2.2: Sensitivities of state-of-the-art ground and space telescopes. Adapted from [64].

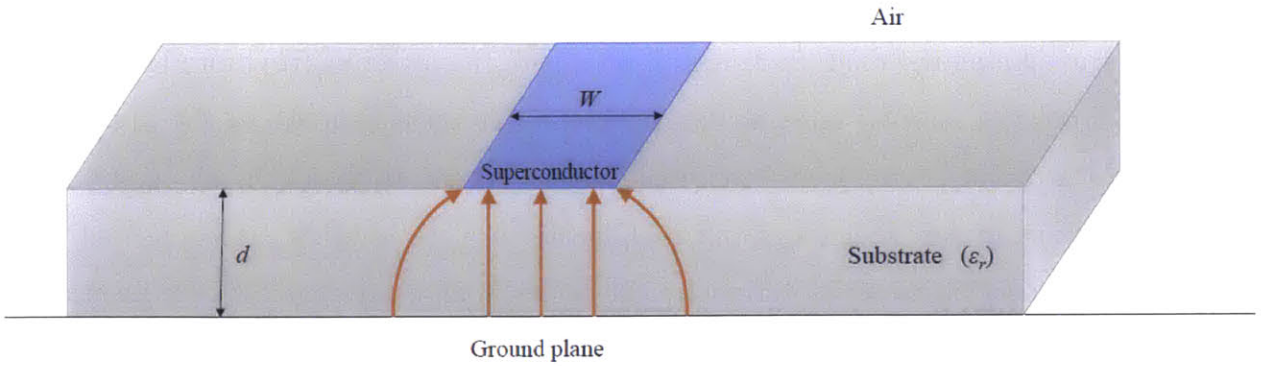

Figure 2.3: Geometry of a microstrip transmission line. In orange are the electric field lines indicating their dominant modal symmetry.

The instrument is integrated on a 100–mm–diameter silicon chip. This size reduction is achieved through the use of single-mode microstrip transmission lines, which can compactly be folded on the silicon wafer and reduce the required physical line length by a factor of the material's effective refractive index. Specifically, a transmission line is a distributed-parameter network whose dimensions are on the order of microwave or submillimeter wavelengths. Because of this, the phase of a voltage or current varies greatly over the physical extent of the transmission line. This is opposed to the behavior at lower frequencies, where the wavelengths are large enough that there is insignificant phase variation across the dimension of the electrical component (a lumped-element circuit). At higher frequencies, instead, the wavelengths are much shorter than the dimensions of the device and Maxwell's equations simplify to the geometrical optics regime [65]. A microstrip line is a type of planar transmission line, whose geometry can be seen in Fig. 2.3. A conductor of width W is printed on a grounded dielectric substrate of thickness d and relative permittivity ε_r. This structure can be fabricated by photolithographic processes and integrated with other active or passive microwave devices. The material's effective dielectric function, $\varepsilon_{r,\text{eff}}$, is a weighted combination of the dielectric functions of both the substrate and the air around the structure: $\varepsilon_{r,\text{eff}} = q_\epsilon\, \varepsilon_r(\text{substrate}) + (1 - q_\epsilon)\, \varepsilon_r(\text{air})$, where q_ϵ represents the dielectric filling fraction of the substrate. The effective dielectric function can be interpreted as the dielectric function of a homogeneous material that replaces both the air and the substrate [65]. The dielectric filling fraction is defined as $q_\epsilon = (F + 1)/2$, where F depends only on the substrate thickness and the superconductor width, but not on the substrate dielectric function, $\varepsilon_{r,\text{eff}}$ [66].

As for the choice of the instrument operational spectral range, apart from being of scientific interest for all of the reasons described in Chapter 1, it also lies below the gap frequency of the superconductors that are being considered for the development of the transmission lines. These include niobium (Nb), niobium-titanium nitride (NbTiN), and molybdenum nitride (MoN), with critical temperatures of 9.3 K, 17.1 K, and 5 to 12 K, respectively. In particular, unless a low-loss superconductor with a gap larger than NbTiN becomes available, the technology is confined to wavelengths $\lambda > 250$ µm.

The predicted sensitivity of the instrument can be achieved by employing an array of low-noise $\left(\text{NEP} < 10^{-20}\text{W}/\sqrt{\text{Hz}}\right)$ direct (incoherent) detectors and reducing the stray light falling on the detectors. Direct detectors are promising because they are not affected by quantum noise caused by spontaneous photon emission. In our case, because the infrared thermal background is their dominant source of noise, they are background-limited and photon counting is possible at least in principle [67]. In addition, superconducting materials exhibit extremely low losses below their critical temperature, and thus represent a crucial element for this type of technology, as explained above.

The reduction in stray light is accomplished by coupling the spectrum efficiently to the optical system via a hyperhemispherical lens (Fig. 2.1). Since the only input to the instrument is through its broadband antenna, it provides unique protection of the low-NEP detectors from their surrounding environment. In other words, µ-Spec will be an **integrated** spectrometer as it has this feature designed in from its conception, thereby overcoming the challenge of controlling undesired radiation in this type of sensitive detectors.

Finally, augmenting the number of µ-Spec modules will allow for multi-object spectroscopy as each module can independently analyze the light coming from different objects. As for the maximum number of modules that can be accommodated, the limiting factor is the power constraints as well as the efficiency and volume available for the electronics, both warm and cold. The warm electronics requires further study as no flightworthy electronics systems for the instrument detectors has been built. High electron mobility transistor (HEMT) amplifiers for use in space can be produced with noise temperature of 3 K for about 2 mW of power dissipation at 4 K [68–70]. With 1000 resonators per GHz, this would be

sufficient for a few thousand detectors. In order to increase the number of detectors, studies will be necessary to explore alternatives for minimizing power dissipation. This, however, is beyond the scope of the work described here and can be addressed when more information becomes available on the specific type of mission that will require to fly the μ-Spec technology (e.g., a space telescope or an atmospheric balloon).

2.3 Thesis objectives

Figure 2.4 below is a simplified representation of Fig. 2.1, which shows the different subsystems of μ-Spec. The specific contributions of this thesis work look at the delay network, the multimode region, and the detector subsystems.

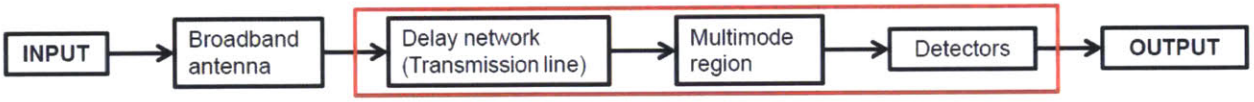

Figure 2.4: Block diagram of the μ-Spec module. The filter banks have been omitted in the Detectors box for clarity. The red box identifies the three subsystems object of this thesis work.

The primary technical questions which must be answered to enable the μ-Spec technology are the following:

1. What is the dielectric loss in the microstrip transmission lines over the required spectral range (300–650 GHz)? How does it differ for amorphous and monocrystalline materials? Which materials would be best suited to maximize the coupling efficiency in the system?

2. Does there exist a feasible design of a spectrometer that meets the requirements in Table 2.2? What are the trade-offs involved in this design? How can the instrument performance be optimized in terms of coupling efficiency and spectral purity?

3. What are the propagation properties of the microstrip transmission lines made of superconductors such as molybdenum nitride and niobium? These parameters are needed for the design of the detectors and read-out system. Can the determination and accuracy of these parameters be improved, and how?

The main objective of this thesis is to explore the feasibility of this new technology concept and develop the necessary tools to answer these questions. The approach followed is summarized below.

1. To study the loss of dielectric materials to be used as substrates in the microstrip transmission lines, analytical models and numerical algorithms have been developed to extract the dielectric function of these materials from laboratory transmission data as a function of frequency. The final result is a database of infrared dielectric properties of silicon-based materials with applications in spectrometry and detectors development, such as silicon nitride, silicon oxide, and single-crystal silicon.

2. To find feasible designs for an ultracompact (10–cm^2) spectrometer that satisfy the requirements in Table 2.2, an optical design methodology has been developed for the spectrometer diffractive region over the 450–1000–μm wavelength range. This methodology is used to explore the design space and find optimal solutions that simultaneously maximize the instrument throughput and minimize the phase error on the focal plane. Several designs have been found and the following five case studies are examined in detail:

   - A proof of concept of a low-resolution ($\mathcal{R} = 65$), first-order design to be used to build and test a spectrometer prototype
   - Four medium/high-resolution ($\mathcal{R} > 250$), higher-order designs optimized to yield a nearly 100% throughput and maximize the focal plane utilization for potential use on flight missions

3. To study the properties of the superconducting materials employed in the transmission lines and detectors, analysis and calibration techniques have been developed for superconducting resonators commonly employed in MKIDs, with particular attention to what causes performance degradation (e.g., two-level systems mentioned in Chapter 5).

2.4 Thesis outline

The presentation of this thesis will guide the reader through each of the three subsystems illustrated in Fig. 2.4. Each chapter will be articulated as follows: question(s) to be answered, brief review of the state of the art, summary of specific current technology gaps, description of the found solution with details of the adopted methodology, and review of the results.

Chapter 3 will address Question 1 by describing the models developed and used to extract the dielectric properties of two amorphous materials, namely, silicon nitride and silicon oxide. Their derived loss is compared to that of single-crystal silicon data from the literature to show that low-loss monocrystalline materials will be necessary in the transmission lines.

Chapter 4 will address Question 2 and will describe in detail the design of the μ-Spec multimode region with all the trade-offs involved. A discussion of the numerical methods used will also accompany the discussion as a complement to the challenges encountered to solve large complex systems of equations.

Chapter 5 will address Question 3 by presenting novel analysis and calibration techniques for superconducting resonators that compose the μ-Spec detectors. A phenomenological model is first presented for the computation of the resonators' quality factors and central frequencies. An ABCD-matrix approach is then proposed to validate the phenomenological model and extract more detailed information on the resonators' internal structure.

Finally, Chapter 6 will summarize the main findings of this thesis work and discuss possibilities for future work.

Chapter 3

μ-Spec transmission lines: materials characterization

Question 1: What is the dielectric loss in the microstrip transmission lines over the required spectral range (300–650 GHz)? How does it differ for amorphous and monocrystalline materials? Which materials would be best suited to maximize the coupling efficiency in the system?

The μ-Spec power divider, delay network, and detectors are all realized through microstrip transmission lines (Fig. 2.4). As shown in Section 2.2, these are generally characterized by a dielectric substrate holding a thin layer of conducting material etched in the substrate surface through photolithographic processes. To reduce materials losses in such high-sensitivity systems, it is crucial to employ superconducting materials and single-crystal dielectric substrates.

In superconductors, electrical currents can flow without resistance below a characteristic critical temperature, thereby minimizing losses in the energy through the material. Examples of superconductors are aluminum, molybdenum, niobium, titanium, mercury, zinc, or alloys such as niobium-titanium, molybdenum-nitride, and magnesium diboride, each characterized by its own critical temperature usually below 40 K. Niobium, niobium-titanium-nitride, and molybdenum nitride have been chosen as possible candidates for μ-Spec, because their conduction bands lie within the spectral range of interest, their critical temperatures are

attainable without requiring sophisticated cooling systems, and they can be handled safely.

In single-crystal dielectrics, the crystal lattice of the entire solid is continuous and without grain boundaries. The grain boundaries are defects in the crystal structure which tend to decrease the electrical and thermal conductivity of the material and are important to many of the mechanisms of creep. The absence of similar defects confers monocrystalline materials unique mechanical, optical, and electrical properties, making them an important resource for many industrial applications, especially in electronics and optics. In addition, they are suited to reach optimal sensitivities because they reduce losses and noise associated with two-level systems typically found in amorphous (non-crystalline) materials (see Sec. 5.1).

This chapter will address the characterization of the dielectric properties of amorphous silicon compounds through the derivation of their complex dielectric functions over the frequency range of interest (the far-infrared, in this case) from measured transmission data. These complex dielectric functions will then be compared with those of single-crystal silicon samples that were previously analyzed by the author [71, 72] or that can be found in the literature [73, 74]. This will serve as a comparison of materials with distinct properties and applications, and it will show the superiority of monocrystalline silicon.

To perform this study, the transmission of these materials samples was measured in the infrared through Fourier Transform Spectroscopy (FTS). Appropriate mathematical models were then used to fit these data and extract the materials' complex dielectric functions. The mathematical models and numerical methods employed to analyze the transmission measurements have been developed by the author and discussed in [32, 33, 75, 76]. The next two sections report specifically on the characterization of amorphous silicon-nitride samples, as described in [75] (Sec. 3.2), and silicon-oxide membranes (Sec. 3.3). The characterization of the superconducting materials is addressed in detail in Chapter 5, since it requires different measurement approaches and analysis techniques.

3.1 The complex dielectric function

The electromagnetic response of a material as a function of frequency, ω, is represented by its relative permittivity, $\hat{\varepsilon}_r(\omega) = \varepsilon'_r(\omega) + i\,\varepsilon''_r(\omega)$, defined as the ratio of the material's complex

absolute permittivity (or complex dielectric function), $\varepsilon(\omega)$, to the vacuum permittivity, ε_o. From a physical perspective, the absolute permittivity defines the material's polarizability (i.e., the average dipole moment per unit volume) relative to the incident electric field. Its real part determines the phase velocity in the material, while its imaginary part the attenuation of electromagnetic waves passing through the medium.

The real and imaginary components of the complex refractive index, $N = n + i\kappa$, can readily be derived from those of the complex dielectric function as follows:

$$n = \sqrt{\frac{\sqrt{\varepsilon_r'^2 + \varepsilon_r''^2} + \varepsilon_r'}{2}}, \qquad \kappa = \sqrt{\frac{\sqrt{\varepsilon_r'^2 + \varepsilon_r''^2} - \varepsilon_r'}{2}}, \tag{3.1}$$

assuming the material to be nonmagnetic ($\mu = \mu_o$).

H. A. Lorentz developed a classical theory for the complex dielectric function, in which electrons and ions are treated as harmonic oscillators subject to an elastic force, a damping force, and the driving force of the applied electromagnetic field. The model assumes the atoms to be a collection of identical, independent, isotropic, harmonic oscillators with a certain mass and charge. The equation of motion of these oscillators can therefore be expressed as a second-order differential equation. The oscillatory solution, with the same frequency as the driving field, can readily be related to the material's polarizability, and thus to the complex dielectric function. A more in-depth description of this theory is provided in [6], where other models are also discussed, such as the Drude model for free-electron metals or the Debye relaxation model for polarizing matter with permanent (as opposed to induced) electric dipoles. More models exist in the literature [77, 78], some of which will be described in the next sections.

3.2 Analysis of the dielectric properties of silicon nitride thin films

The study of the infrared dielectric properties of silicon nitride thin films was presented by the author and collaborators in [75]. It is reported in the remainder of this section as found

in this reference, with minor edits to improve clarity.

"Silicon nitride films are amorphous, highly absorbing in the mid-IR [79], and their general properties are functions of composition [80, 81]. Silicon nitride thin films are commonly employed in the microfabrication of structures requiring mechanical support, thermal isolation, and low-loss microwave signal propagation [82–85]. The optical tests were performed on samples having membrane thicknesses of 0.5 and 2.3 μm with an uncertainty of 3%.

The dielectric response is represented as a function of frequency, ω, by the classical Maxwell-Helmholtz-Drude dispersion model [77]:

$$\hat{\varepsilon}_r(\omega) = \hat{\varepsilon}_\infty + \sum_{j=1}^{M} \frac{\Delta\hat{\varepsilon}_j \cdot \omega_{T_j}^2}{\omega_{T_j}^2 - \omega^2 - i\omega\Gamma'_j(\omega)} \tag{3.2}$$

where M is the number of oscillators and $\hat{\varepsilon}_r = \varepsilon'_r + i\,\varepsilon''_r$ is a complex function of $(5M + 2)$ degrees of freedom, which are as follows: the contribution to the relative permittivity $\hat{\varepsilon}_\infty = \hat{\varepsilon}_{M+1}$ of higher lying transitions, the difference in relative complex dielectric constant between adjacent oscillators $\Delta\hat{\varepsilon}_j = \hat{\varepsilon}_j - \hat{\varepsilon}_{j+1}$ which serves as a measure of the oscillator strength, the oscillator resonance frequency ω_{T_j}, and the effective Lorentzian damping coefficient Γ'_j, for $j = 1, ..., M$. For the silicon nitride films analyzed, the following functional form was used to specify the damping:

$$\Gamma'_j(\omega) = \Gamma_j \exp\left[-\alpha_j \left(\frac{\omega_{T_j}^2 - \omega^2}{\omega\Gamma_j}\right)^2\right] \tag{3.3}$$

where α_j allows interpolation between Lorentzian ($\alpha_j = 0$) and Gaussian wings ($\alpha_j > 0$) similar to the approach in [86]. The form indicated above enables a more accurate representation of relatively strong oscillator features.

The impedance contrast between free space and the thin-film sample forms a Fabry-Perot resonator. The observed transmission can be modeled [87] as a function of the dielectric response [Eq. (3.2)], thickness, and wavenumber. The dielectric parameters were solved by means of a non-linear least-squares fit of the transmission equation to the laboratory FTS data. Specifically, a sequential quadratic programming (SQP) method with computation of

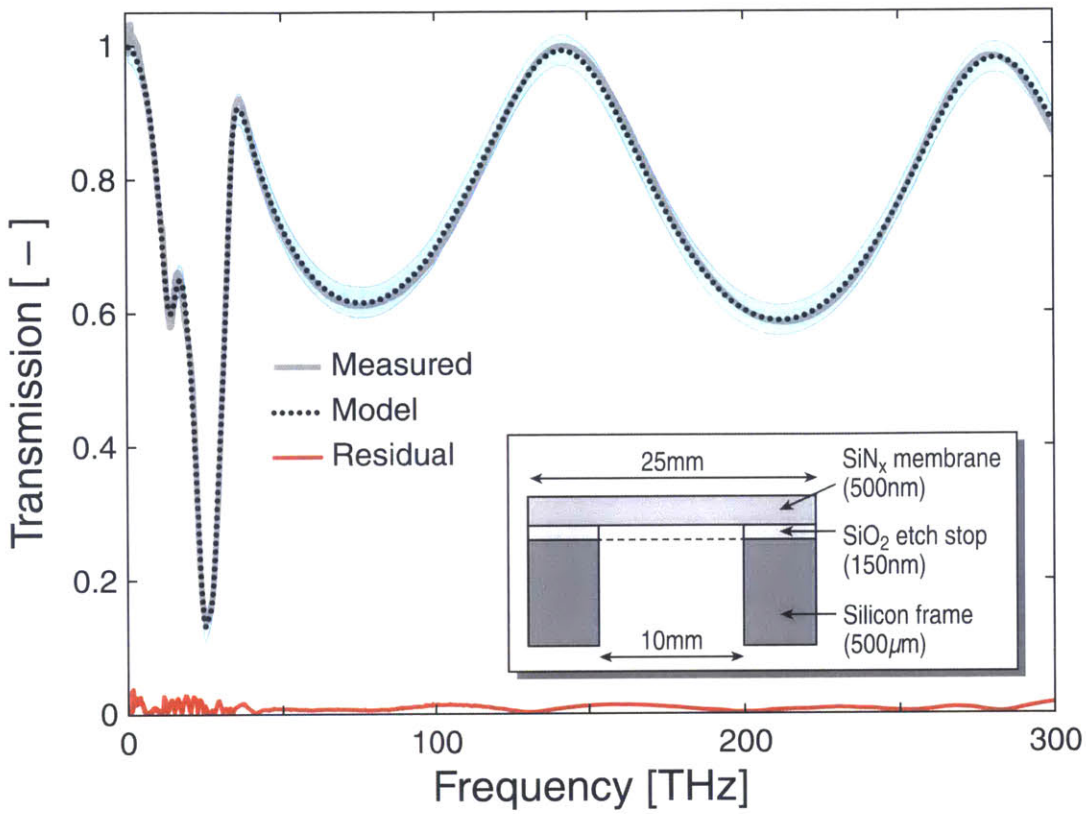

Figure 3.1: Room-temperature transmission of a silicon nitride sample 0.5 µm thick: measured (grey), model (black dotted), and residual (red). The shaded band's width delimits the estimated 3σ measurement uncertainty. A 30 GHz (1 cm^{-1}) resolution is employed for the measurement. The insert depicts the geometry of the SiN_x membrane and micro-machined silicon frame. Adapted from [75].

the Jacobian and Hessian matrices [88, 89] was implemented. The merit function, χ^2,was used in a constrained minimization over frequency as follows:

$$\min_{\text{DOF}} \chi^2 = \min_{\text{DOF}} \sum_{k=1}^{N} \left[T(\hat{\varepsilon}_r(\omega), h) - T_{\text{FTS}_k} \right]^2 \tag{3.4}$$

where N is the number of data points, T the modeled transmittance, T_{FTS} the measured transmittance data, and h is the measured sample thickness. We are guided by the Kramers-Kronig relations in defining constraints for a passive material: $|\hat{\varepsilon}_j| > |\hat{\varepsilon}_{j+1}|$, $\varepsilon_j'' > 0$ and $\hat{\varepsilon}_r(0) = \hat{\varepsilon}_1$ [90].[1] [The Kramers-Kronig relations ensure causality, so that the light cannot be reflected or absorbed by a system before the arrival of the primary light wave.] For accurate parameter determination the sample should have uniform thickness, be adequately

[1]The transmission cannot be zero, because if it were the field must vanish throughout the space. This would not be possible when a multilayered stack, as is the case here, is illuminated by a plane wave [91].

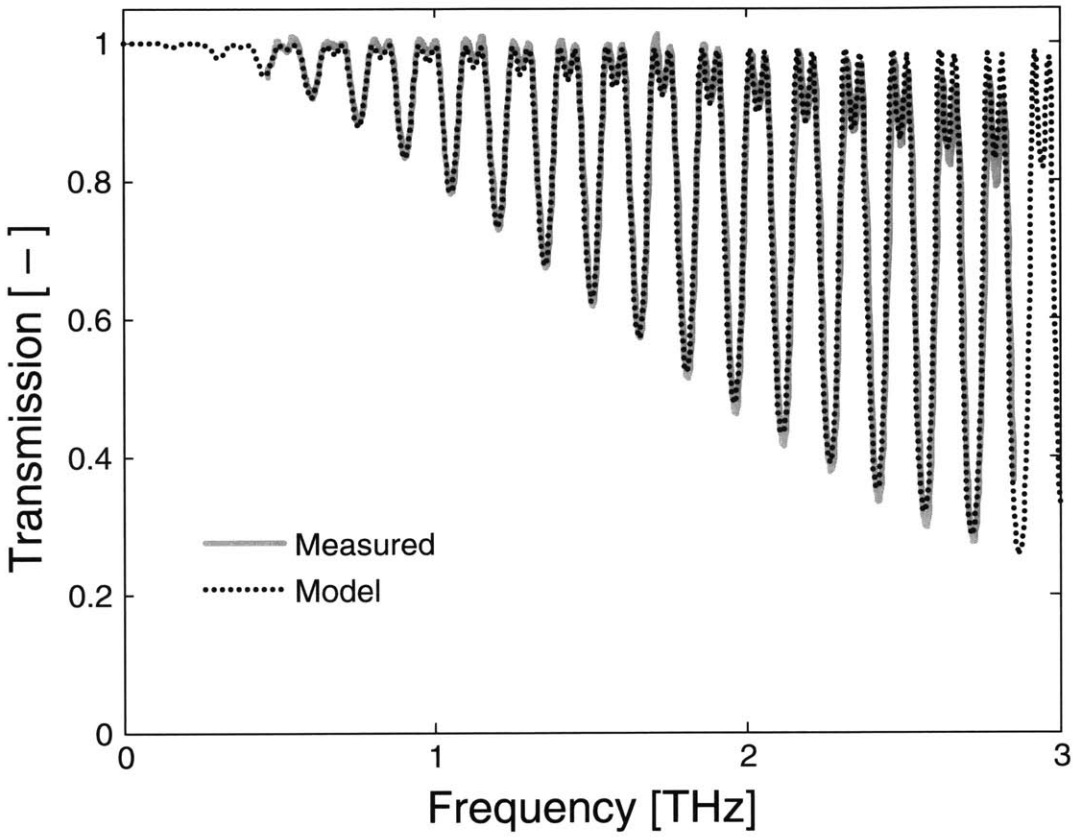

Figure 3.2: Measured (solid grey) and model (black dotted) transmission for a 3-layer stack of silicon nitride samples 2.3 µm in thickness with 998-µm intermembrane delays which complements the data shown in Fig. 3.1. The sample response in the far-infrared was acquired with a resolution of 3 GHz (0.1 cm^{-1}). Adapted from [75].

transparent to achieve high signal-to-noise, and have diffuse scattering as a sub-dominate process. The method requires an *a posteriori* numerical verification for Kramers-Kronig consistency. In the example presented here, a numerical Hilbert transform [92] of $\varepsilon_r''(\omega)$ reproduces $\varepsilon_r'(\omega)$ to within 2% (Fig. 3.3). An alternative method employing reflectivity and phase allows *a priori* Kramers-Kronig consistent results [93]. However, given the details of the thin-film samples and available instrumentation, this approach was not implemented.

Figure 3.1 illustrates the measured and modeled results obtained from the analysis of a 0.5-µm-thick sample. The peak residual in the transmittance is less than 3% and the $3\sigma = 0.023$ uncertainty band indicated corresponds to the 99.7% confidence level. The standard deviation adopted for the measured data, σ, was estimated assuming the errors as

a function of frequency are uniform and have a reduced χ^2 equal to unity. An additional uncertainty in the FTS normalization influences the dielectric response function at the 1% level. In addition to the channel spectra, the observed spectrum shows two predominant features at 12 THz and 25 THz. Simulations with $M = 2$ oscillators lead to a peak residual on transmission of 5% and do not enable recovery of the resonance at 25 THz. Using 5 oscillators satisfactorily recovers the observed transmittance and reduces the peak residual by a factor of 4.4. When the resonator's quality factor, $Q_{eff_j} = \omega_j/\Gamma'_j$, is greater than 5, the data were not reproducible by either a pure Lorentzian oscillator or Eq. (4.6) in [86]. In these regions, the peak transmission residuals were decreased by a factor ~ 2 through the use of Eq. (3.3).

In Fig. 3.3 the values of the real and imaginary components of the dielectric function are illustrated as a function of frequency. The uncertainty in $\hat{\varepsilon}_r$ was propagated and computed as described in [94]. Table 3.1 contains a summary of the best fit parameters for 5 oscillators, which can be used to reproduce the data shown in Fig. 3.3.

Table 3.1: Fit parameter summary for the analyzed silicon nitride sample (Adapted from [75])

j [−]	ε'_j [−]	ε''_j [−]	$\omega_{T_j}/2\pi$ [THz]	$\Gamma_j/2\pi$ [THz]	α_j [−]
1	7.582	0	13.913	5.810	0.0001
2	6.754	0.3759	15.053	6.436	0.3427
3	6.601	0.0041	24.521	2.751	0.0006
4	5.430	0.1179	26.440	3.482	0.0002
5	4.601	0.2073	31.724	5.948	0.0080
6	4.562	0.0124			

In order to characterize the long-wavelength portion of the dielectric function, Fabry-Perot resonators were realized from 1-, 2-, and 3-layer samples. Representative data for the 3-layer resonator stack is presented in Fig. 3.2. A multilayer transfer matrix analysis [87] is used to extract the dielectric function using the measured SiN_x (2.3 μm) and silicon spacer (998 μm) thicknesses. The circular symbols at 1.5 THz and 2.5 THz indicated in Fig. 3.3 were computed from a composite analysis of the 3 Fabry-Perot measurement sets. The horizontal range indicates the data used in each fit. The best estimates are $\hat{\varepsilon}_r \approx 7.6 + i\,0.08$ over

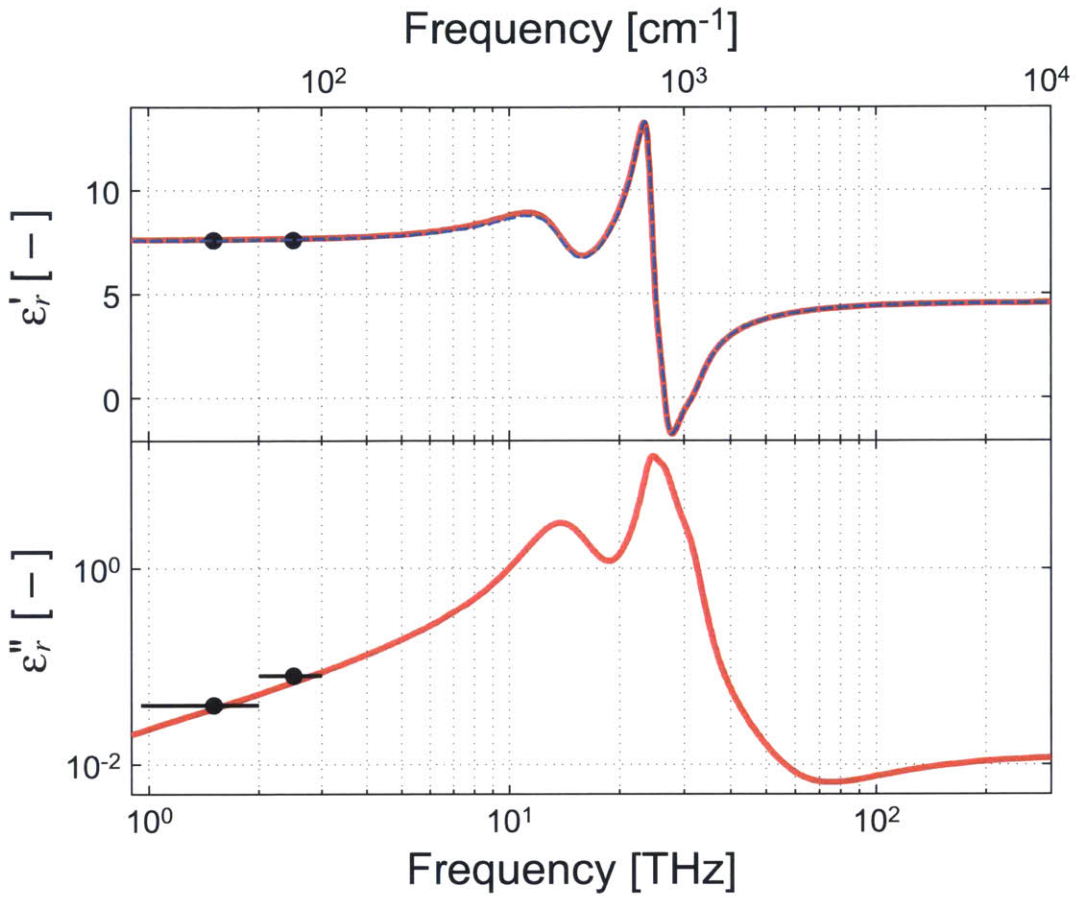

Figure 3.3: Real and imaginary parts (solid red lines) of the dielectric function of silicon nitride as extracted from the data shown in Fig. 3.1. The line thickness is indicative of the propagated $\sim 4\%$ error band. The numerical Hilbert transform of the modeled $\varepsilon_r''(\omega)$ is indicated in the upper panel (dashed blue line) to facilitate comparison with $\varepsilon_r'(\omega)$. The filled symbols indicate the parameters derived from the data presented in Fig. 3.2. Adapted from [75].

the range 2-3 THz and $\hat{\varepsilon}_r \approx 7.6 + i\,0.04$ over 0.4-2 THz. The real component of the static dielectric function derived from the data is in agreement with prior reported parameters for this stoichiometry [85]. As shown in Fig. 3.3, the measurements are internally consistent and represent roughly a factor-of-three reduction in uncertainty relative to prior infrared SiN_x measurements identified by the authors [79–81]. The dielectric parameters reported here are representative of low-stress SiN_x membranes encountered in our fabrication and test efforts." [75]

3.3 Analysis of the dielectric properties of silicon oxide membranes

Amorphous silicon oxide is commonly used as a microwave dielectric medium due to its relatively low loss, insulating properties, and compatibility with microfabrication processing [95, and references therein]. A 1-µm-thick silicon oxide membrane was employed in an experiment to measure its transmission properties. The transmission data are shown in Fig. 3.4, where several large and strong resonators can be seen at frequencies below 40 THz along with some smaller resonators between 40 and 100 THz.

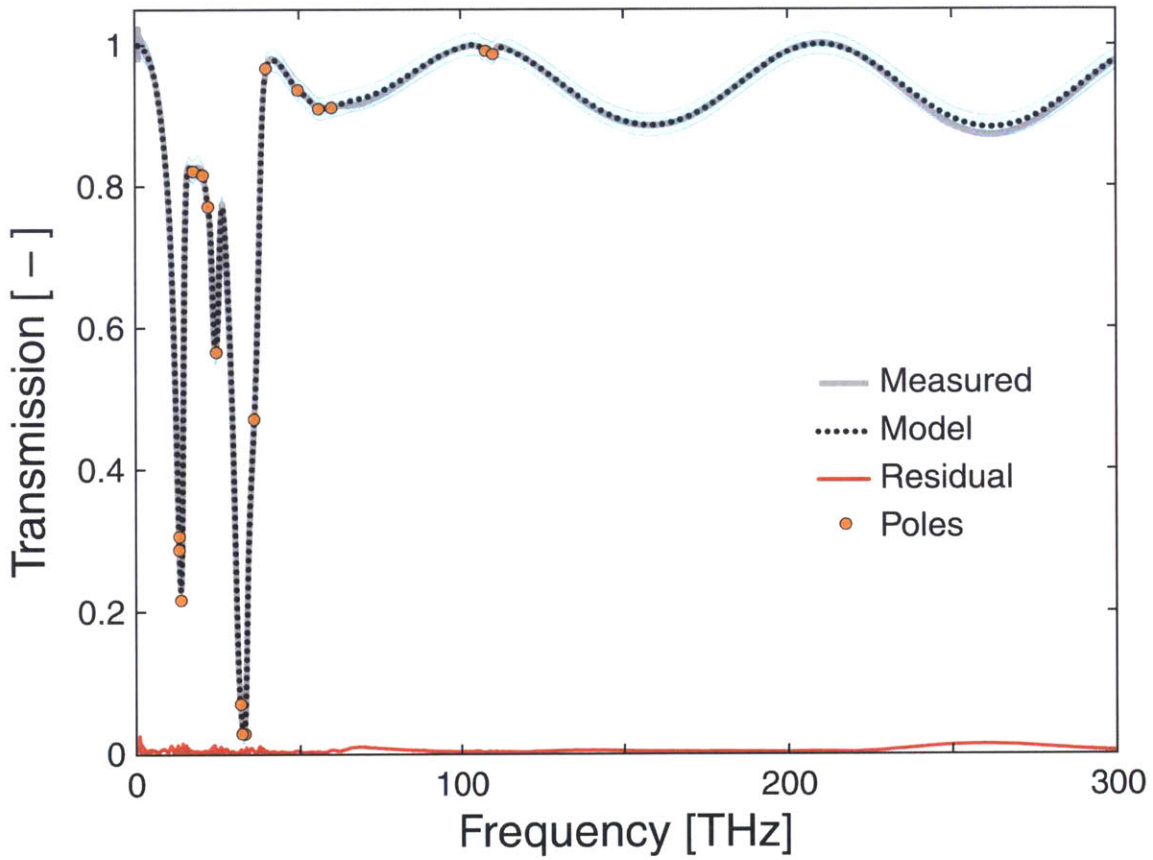

Figure 3.4: Room-temperature transmission of a silicon oxide sample 1.0 µm thick: measured (grey), model (black dotted), and residual (red). The shaded band's width delimits the estimated 3σ measurement uncertainty. The orange dots represent the location of the 17 resonators used in the model. A 30 GHz (1 cm^{-1}) resolution is employed for the measurement.

The model presented in Section 3.2 was initially used for the analysis of this dataset, but singularities were seen in the extracted dielectric function's imaginary component at

approximately 40 and 110 THz. These singularities translated into cusps (i.e., changes in the first derivative) in the transmission function in Fig. 3.4 at those same frequencies. For the dataset analyzed, this behavior was found to be caused by the following factors:

1. Values of $\alpha_j \gtrsim 10^{-5}$. Figure 3.5 illustrates simulated dielectric-function data for $\alpha = 10^{-5}$. It can be seen that the dielectric function (blue line) loses support as its wings fall off rapidly and fail to cover the spectral range of interest.

2. $\mathcal{I}m\{\Delta\hat{\varepsilon}_j\} = \Delta\varepsilon_j'' \gtrsim 10^{-4}$. This was found to have the same effect as α_j discussed above and would sometimes lead to resonators with a negative imaginary component. The set of constraints that enforce a positive imaginary part for each of the M resonators in Eq. (3.2) reads as follows:

$$\begin{cases} \dfrac{\Delta\varepsilon_j''}{\Delta\varepsilon_j'} \cdot \dfrac{\omega_{T_j}^2 - \omega^2}{\omega\Gamma_j'(\omega)} \geq -1, & j = 1, \ldots, M \\ \Delta\varepsilon_j' \geq 0, & j = 1, \ldots, M \end{cases} \tag{3.5}$$

   It can be seen from the first of Eqs. (3.5) that the ambiguity in the solution arises from the second-order terms in the numerator $(\omega_{T_j}^2 - \omega^2)$ having both positive and negative roots. These roots, if left unconstrained, could in principle violate Eqs. (3.5), which ensure that the material is passive. This is opposite to what happens in the damping coefficient defined in Eq. (3.3), where the terms $(\omega_{T_j}^2 - \omega^2)$ are squared and the sign of these roots is uninfluential.

Imposing the above-mentioned lower bounds on α_j and the constraints expressed in Eqs. (3.5), however, increased the computational time enormously and made it impractical to improve the fit to the transmission data when working with more than 6 resonators.

The Brendell-Bormann model [78] was found to be capable of reproducing the large and strong resonators without running into similar computational problems. Its advantages lie in the ability to generate bell-shaped (= larger), asymmetrical resonators whose wings can fall off at different rates imposed by Γ and whose imaginary component is always positive by construction. This is achieved by replacing a Lorentzian oscillator with a superposition

of an infinite number of resonators as follows:

$$\hat{\varepsilon}_r(\omega) = \hat{\varepsilon}_\infty + \sum_{j=1}^{M} \frac{1}{\sqrt{2\pi}\sigma_j} \int_{-\infty}^{+\infty} \exp\left[-\frac{(x-\omega_{T_j})^2}{2\sigma_j^2}\right] \times \frac{f_j \omega_{T_j}^2}{(x^2-\omega^2)+i\omega\Gamma_j}\,\mathrm{d}x. \qquad (3.6)$$

The σ_j parameter enables a continuous change in the absorption line shapes which range from a purely Lorentzian when $\sigma_j \approx 0$ to a nearly Gaussian for $\Gamma_j \approx 0$. The strength of each resonator is given by f_j and its resonance frequency by ω_{T_j}. In Eq. (3.6), Γ_j is a real number and does not depend on frequency. The Brendell-Bormann model satisfies the Kramers-Kronig relations by construction. A comparison is given in Figs. 3.5 and 3.6 of the three discussed dielectric function models, i.e., a pure Lorentzian as given by Eq. (3.2) with $\Gamma'(\omega) = \Gamma$, the modified Lorentzian with Eq. (3.3), and the Brendell-Borman model given by Eq. (3.6). The two latter models degenerate into a pure Lorentzian when $\alpha_j = \Delta\varepsilon_j'' = 0$ and $\sigma_j \approx 0$, respectively[2]. Similarly, it was verified that they can replicate each other with an appropriate choice of parameters.

The integrals in Eq. (3.6) can be calculated analytically through Eqs. (5)-(6)-(7) found in [78]. The analysis of the measured transmission data in Fig. 3.4 was done by minimizing the same merit function defined in Eq. (3.4) and performing a non-linear least-squares fit of the transmission equation to the laboratory data with 17 resonators. A sequential quadratic programming (SQP) algorithm was implemented with finite-difference computation of the Jacobian and Hessian matrices. In addition, given the variables differ from each other by several orders of magnitude, a scaling of the variables and constraints was done at each iteration to condition the problem and speed convergence.

The modeled results for the transmission are shown in Fig. 3.4 with the measured data. The peak residual in the transmission is less than 1.3% and the $3\sigma = 0.0134$ uncertainty band indicated corresponds to the 99.7% confidence level. The standard deviation adopted for the measured data, σ, was estimated assuming that the errors as a function of frequency are uniform and have a reduced χ^2 equal to unity. An additional uncertainty in the FTS normalization influences the dielectric response function at the 1% level. In Fig. 3.7 the values of the real and imaginary components of the dielectric function are illustrated as a

[2]Equation (3.6) degenerates when $\sigma_j = 0$.

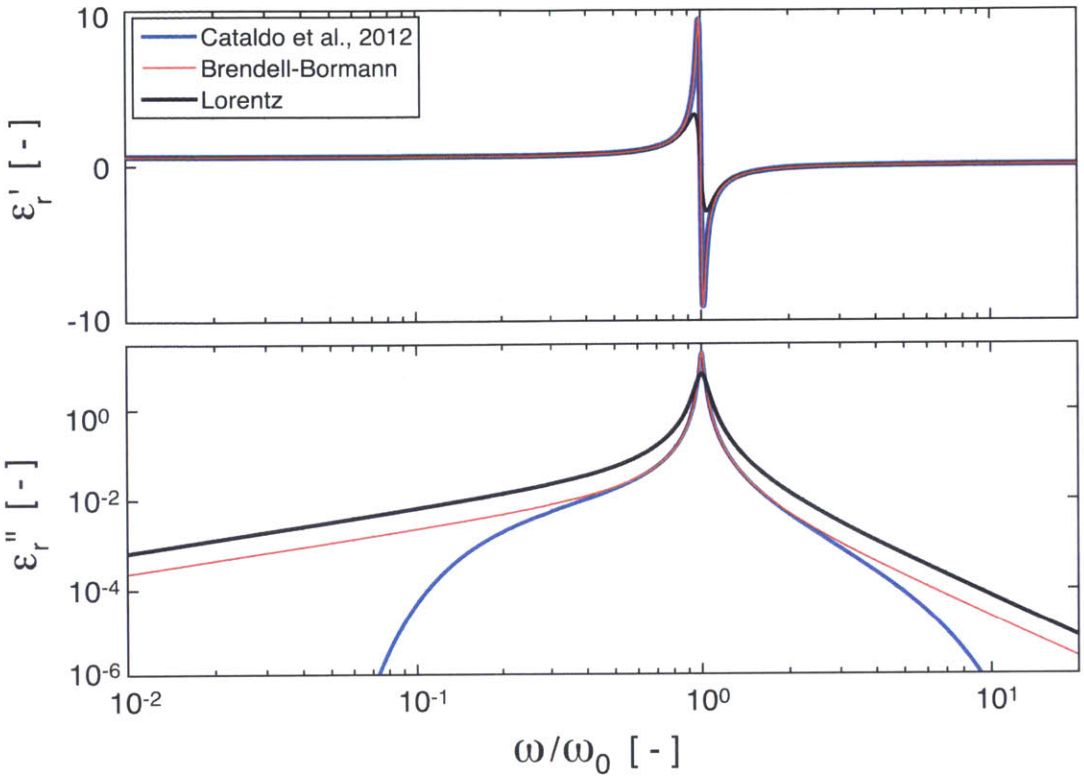

(a) $\alpha = 10^{-5}$, $\sigma = 1$, $\Gamma/\Gamma_0 = 1/3$, where Γ_0 refers to the Lorenztian (black).

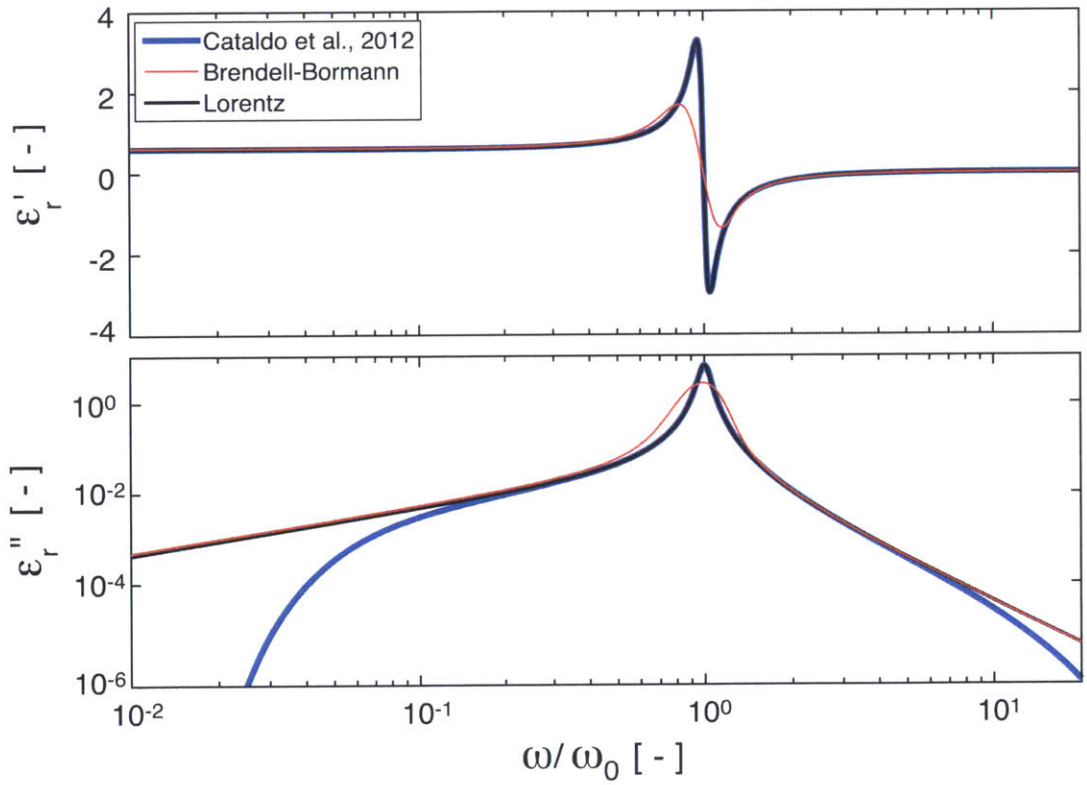

(b) $\alpha = 10^{-5}$, $\sigma = 300$, $\Gamma/\Gamma_0 = 1$, where Γ_0 refers to the Lorenztian (black).

Figure 3.5: Real and imaginary parts of simulated dielectric functions for the three models discussed.

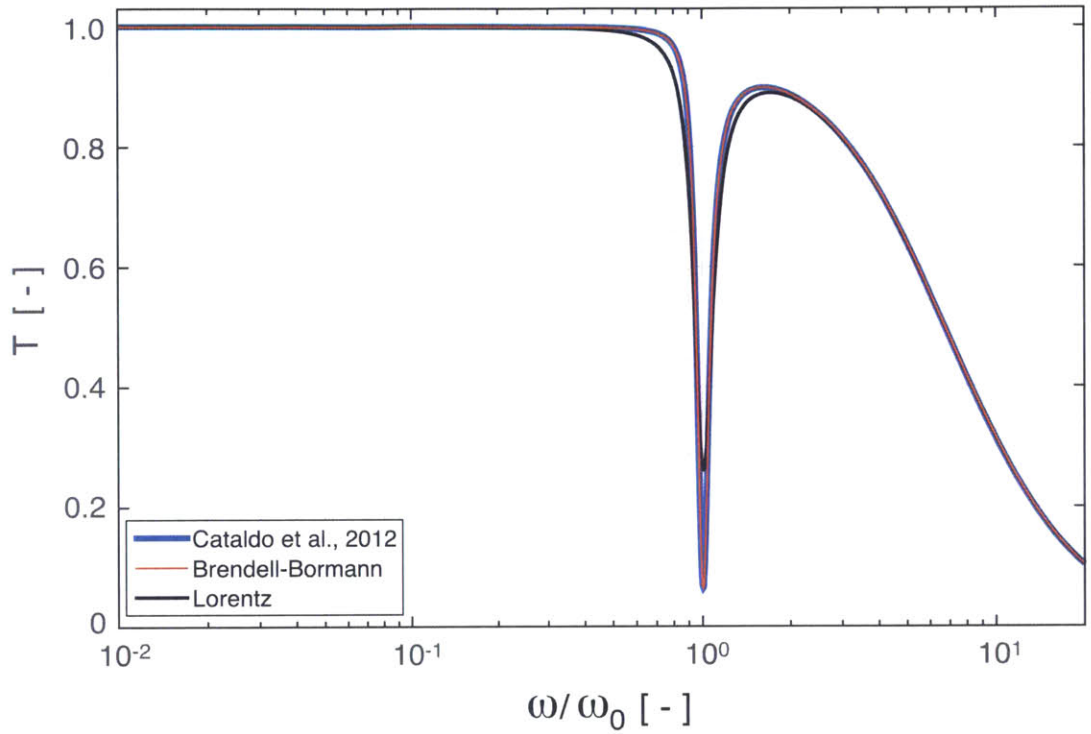

(a) $\alpha = 10^{-5}$, $\sigma = 1$, $\Gamma/\Gamma_0 = 1/3$, where Γ_0 refers to the Lorenztian (black).

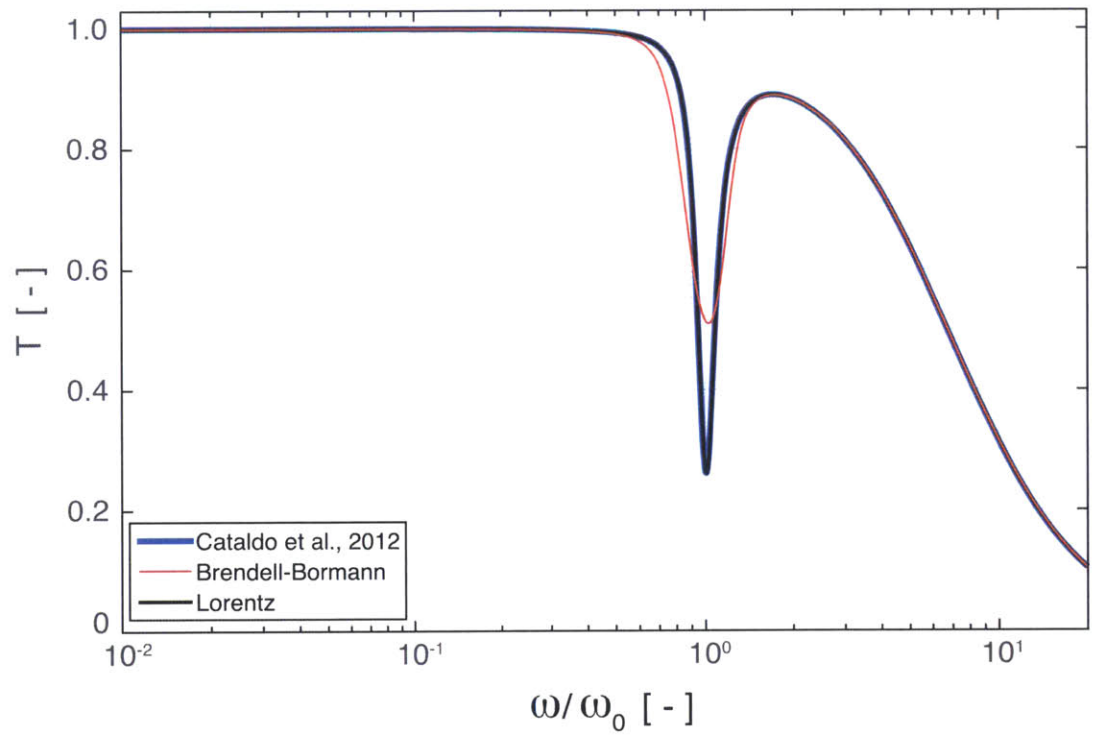

(b) $\alpha = 10^{-5}$, $\sigma = 300$, $\Gamma/\Gamma_0 = 1$, where Γ_0 refers to the Lorenztian (black).

Figure 3.6: Simulated transmission functions for the three models discussed.

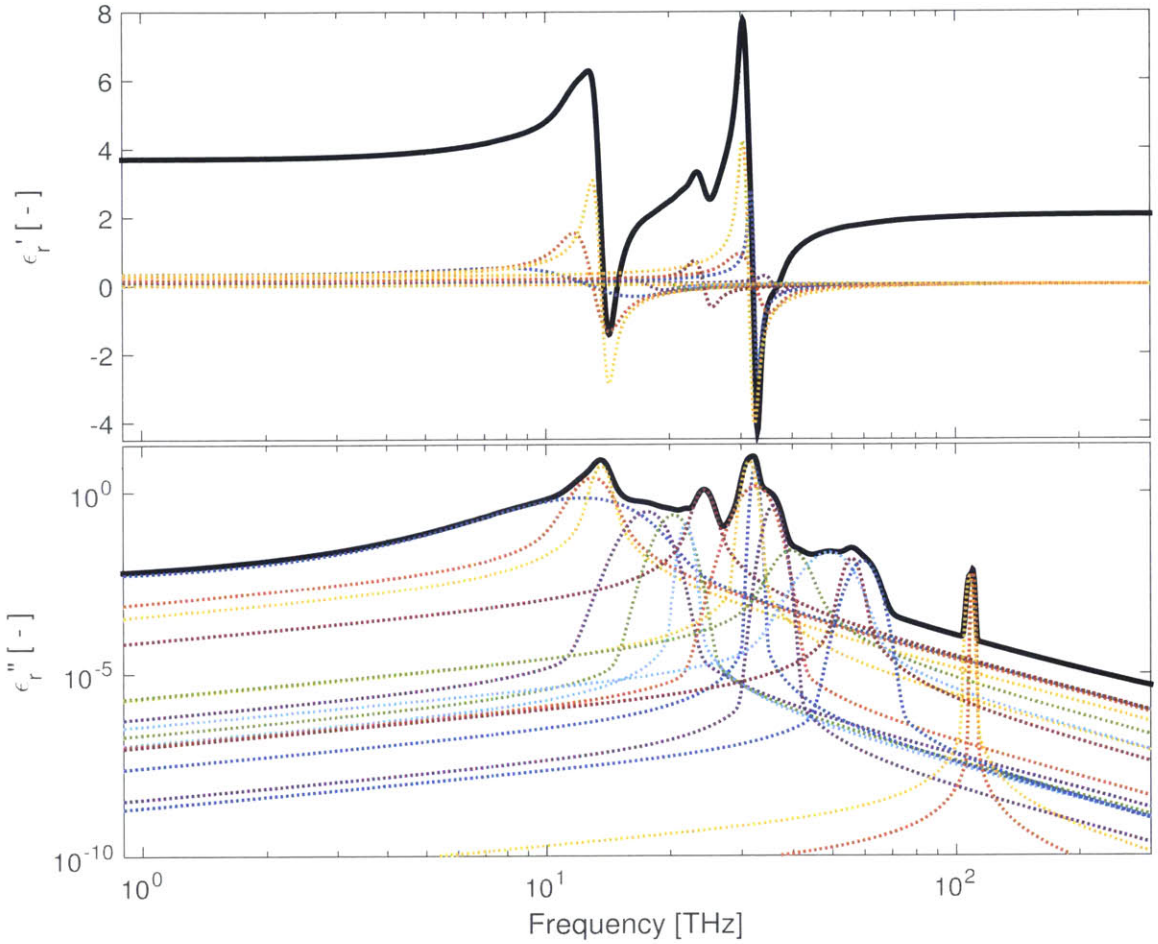

Figure 3.7: Real and imaginary parts of the dielectric function of silicon oxide as extracted from the data shown in Fig. 3.4. The line thickness is indicative of the propagated $\sim 3\%$ error band. Each of the 17 resonators used to fit the model to the measured data is shown.

function of frequency. The uncertainty in $\hat{\varepsilon}_r$ was propagated and computed as described in [94]. The complex refractive index was computed through Eq. (3.1) and its real and imaginary components, n and κ respectively, are shown in Fig. 3.8.

A comparison of these n and κ values with data in the literature [95, and references therein] shows that above 100 THz the absorption index, κ, is nearly one order of magnitude higher (Fig. 3.8). This may be ascribed to two factors. First, from an analysis perspective it was noticed that, without constraints on the resonator widths, Γ_j, the algorithm would converge to acceptable solutions by making the strongest resonators, namely, those below 40 THz (see Fig. 3.7), too wide. From Fig. 3.5a, this is equivalent to having slowly-dying

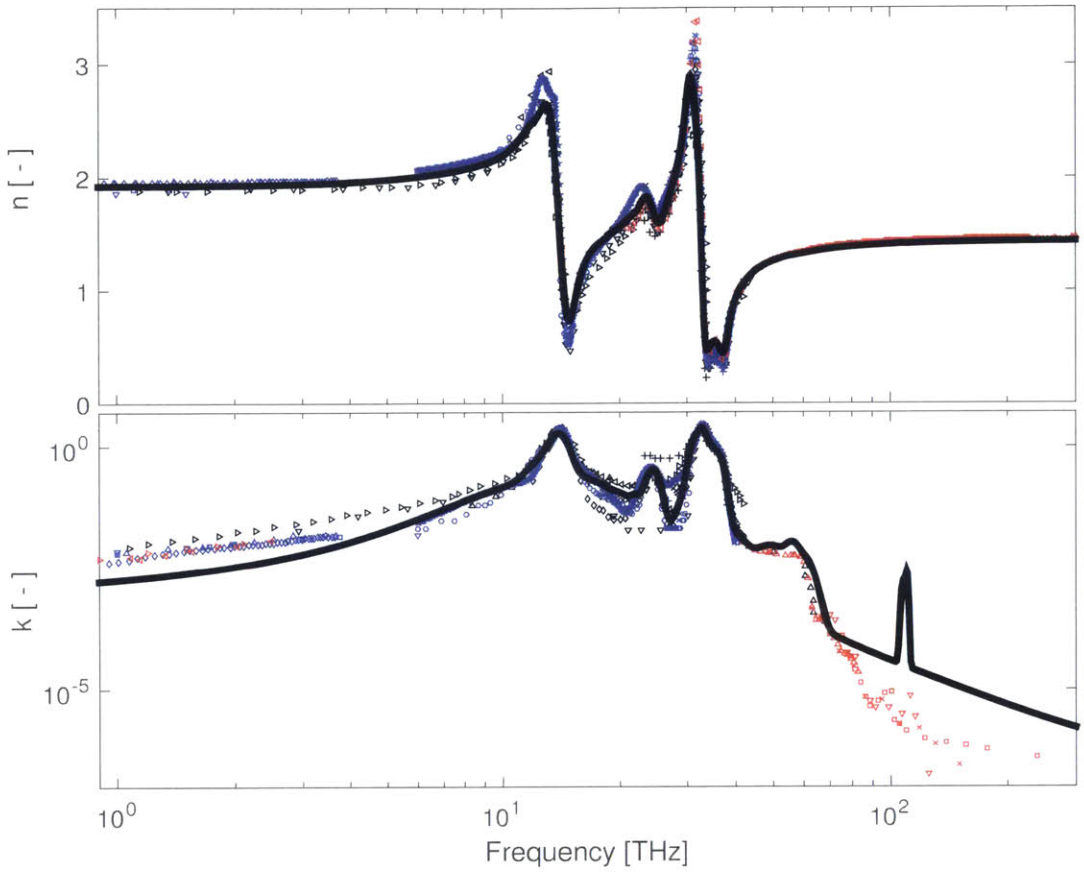

Figure 3.8: Real and imaginary parts of the complex refractive index of silicon oxide as extracted from the data shown in Fig. 3.4. Data from the literature [95, and references therein] are overlaid for comparison. The differences between each dataset are to be ascribed to sample diversity among the various authors.

wings. In this initial unconstrained optimization with 9 resonators, the wings were too high to even achieve ε_r'' values less than 10^{-3} above 100 THz. To enable the wings of such resonators to die out faster, their widths were given appropriate upper bounds so as to make the resonators narrower. Consequently, the number of resonators was increased from 9 to 17 to maintain the residual on the transmission data in Fig. 3.4 below 2%. This strategy enabled achieving the results presented in Figs. 3.7 and 3.8, where the wings of ε_r'' and κ appear to vary within an order of magnitude from the data reported in the literature. Further increasing the number of resonators did not lead to substantial improvements, while making the computational effort larger. The second factor to keep in mind when comparing data with those available in the literature is that the samples used in this type of experiments may

differ from one another in terms of stoichiometric composition and level of purity. This can certainly affect the resulting measurements and extracted parameters, leaving one without any expectation of perfect matching between two or more datasets. Considering the spectral range defined in Table 2.2, however, only data below 10 THz are useful for the purposes of this thesis work or other terahertz applications.

3.4 Summary of findings

Models were developed and used to compute the complex dielectric function of amorphous materials. The numerical properties of the algorithms implemented were studied in detail and used to guide convergence toward physically meaningful solutions.

The complex dielectric functions of the silicon nitride and silicon oxide samples analyzed in this chapter exhibit several spectral features which are associated with transition modes and provide insights into each material's behavior. Over the frequency range analyzed, silicon nitride shows fewer narrower lines than silicon oxide, but it is important to note that all these features do not vary substantially with temperature, given the amorphous nature of the materials.

Conversely, over the same frequency range (1–300 THz), monocrystalline silicon is characterized by a complex dielectric function with a constant real part approximately equal to 11.67 and an imaginary part no greater than $\approx 10^{-3}$ at room temperature [71–74]. The dominant spectral features in the silicon's dielectric function are in fact further removed in frequency than those found in silicon oxide and silicon nitride for the millimeter wave band of interest. In addition, the spectral line widths decrease and their sharpness increases with decreasing temperature, a characteristic which play a crucial role at cryogenic temperatures when looking for low-loss materials.

In conclusion, given these low loss values and the uniformity in the material's response, single-crystal silicon substrates are to be preferred over silicon nitride and silicon oxide when developing such high-sensitivity technologies as μ-Spec. The spectrometer itself can be used to measure the single-crystal silicon's spectral features previously mentioned at cryogenic temperatures.

Chapter 4

μ-Spec multimode region: design and analysis

Question 2: Does there exist a feasible design of a spectrometer that meets the requirements in Table 2.2? What are the trade-offs involved in this design? How can the instrument performance be optimized in terms of coupling efficiency and spectral purity?

To answer these questions, a design methodology was developed to efficiently generate solutions that satisfy given requirements on spectrometer size and spectral range. This methodology allows one to explore the trade-space of all feasible solutions and select those that optimize specific figures of merit. In addition, a model was developed to compute the instrument coupling efficiency and derive other parameters of interest, such as the interchannel power isolation and antenna directivity. This chapter will first present a review of previous spectrometer technologies and will illustrate how μ-Spec differs from them. The reader will then be guided through the details of the design methodology and its application to five case studies.

4.1 Literature review of spectrography

μ-Spec is a transmission spectrometer whose function can be compared to a grating spectrometer [96], where a plane wave is reflected from a grating, which is an optical component with a periodic structure that splits the wave into its spectral components and diffracts them into beams traveling in different directions (Fig. 4.1). Gratings usually consist of rulings and the phase of each partial wave scattered from the rulings is a linear function of position across the grating. This approach is defined as passive spectroscopy because the radiation is observed without changing it, as opposed to active spectroscopy in which the radiation is perturbed to enhance or alter its emission.

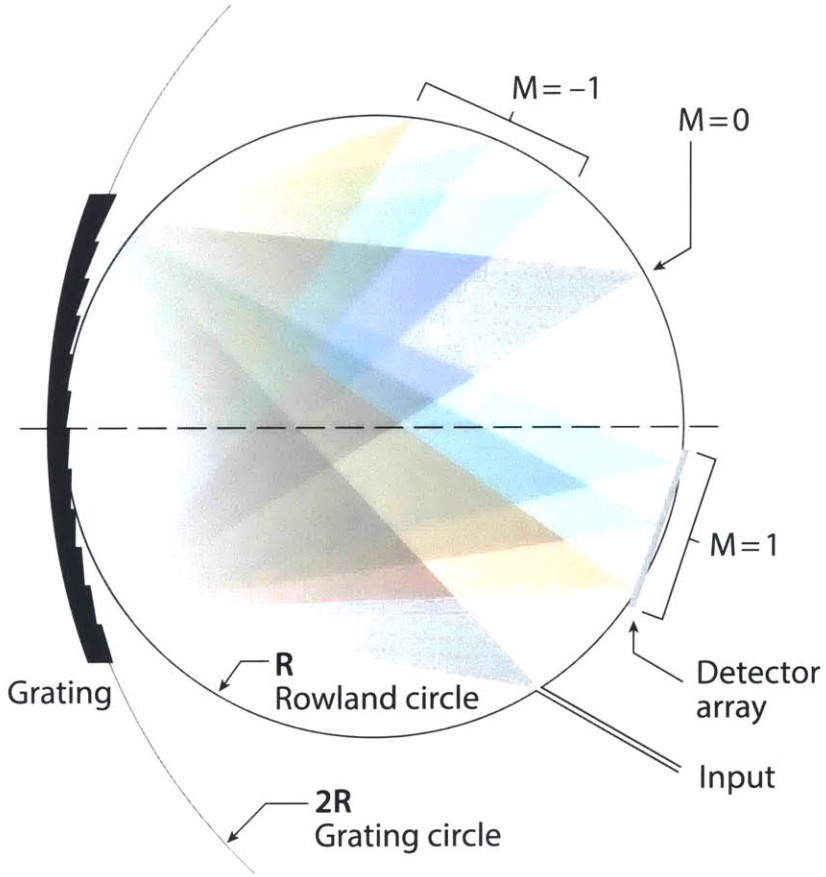

Figure 4.1: Geometry of the Rowland grating. The primary beam (grey) enters the Rowland circle through an input and is diffracted and dispersed by a grating. The beams associated with different orders ($M = 0, 1, -1, \ldots$) are seen on the focal plane, where a detector array is located to intercept the first-order beams.

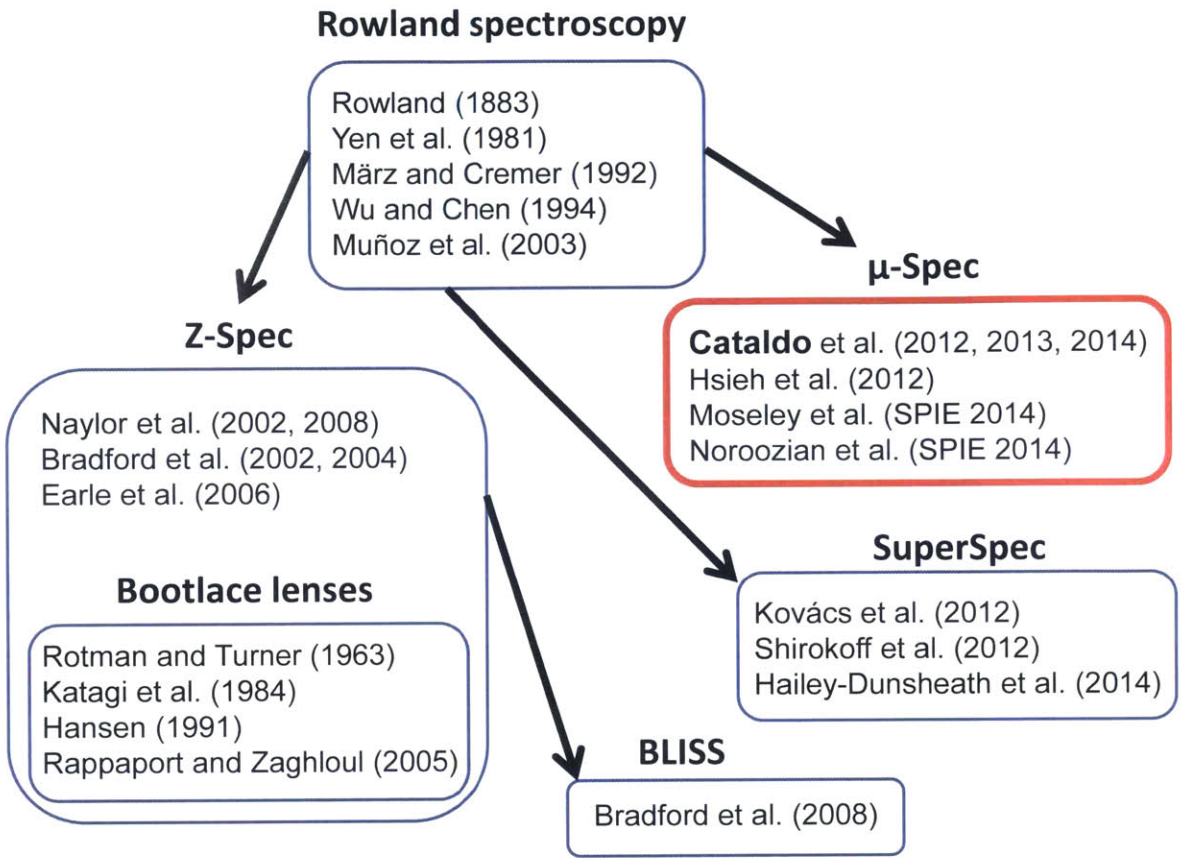

Figure 4.2: Review of the main literature in spectrography

Though remaining a passive spectrometer, μ-Spec does not have rulings. These are replaced by planar feed structures and transmission lines which set the phase delay at the input of its diffractive (multimode) region. Such planar feed structures do not alter the incoming radiation. Figure 4.2 shows an overview of past and current spectrometric technologies, which will be reviewed in detail in the remainder of this section.

In a Rowland spectrometer [96], the light from an input illuminates the grating, whose facets are positioned on a circle of radius $2R$ (Fig. 4.1). The grating diffracts and focuses the radiation to an arc (the focal curve or focal plane) lying approximately on a circle of radius R, called the Rowland circle. The detectors are located on the focal plane to analyze the diffracted light. The required phase retardation is generated by reflection from the grating grooves, which can therefore be positioned in such a way as to provide perfect

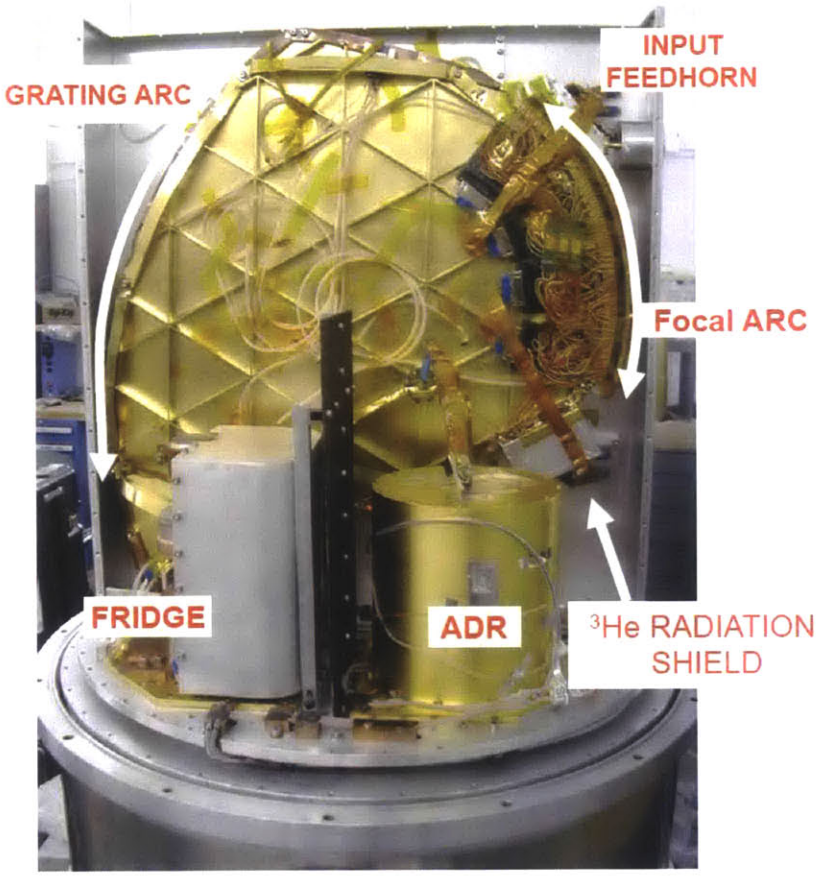

Figure 4.3: Z-Spec is a broadband, millimeter-wave, direct-detection spectrometer. The grating design is based on the Rowland architecture but is more compact (< 60 cm across) because of the use of a parallel-plate waveguide propagation medium. Adapted from [101].

(stigmatic) performance (i.e., zero phase error) at specific frequencies on this detector arc. In the Rowland design [96,97], the grating facets are equally spaced, but higher performance can be achieved by allowing their position to vary and be optimized so that for two stigmatic frequencies the change in path length from one facet to the next results in a phase shift of exactly 2π [98–100].

An example of planar Rowland grating architecture is Z-Spec [102–105], in which the propagation of light occurs in parallel-plate waveguides. Specifically (Fig 4.3), Z-Spec is a broadband, millimeter-wave, direct-detection spectrometer which uses 160 silicon-nitride micromesh bolometers and is cooled to < 100 mK to achieve background-limited performance with a resolution of about 300. Parallel-plate waveguides consist of two flat plates (or

strips) separated by a distance much smaller than their width; a dielectric material fills the region between the two plates. The use of a parallel-plate waveguide propagation medium, therefore, allows Z-Spec to be much more compact than a Rowland spectrometer, though it still remains $\sim$ 55 cm wide. Z-Spec has been proposed for use in the Background-Limited Infrared-Submillimeter Spectrograph (BLISS). BLISS employs transition-edge-sensor (TES) bolometers and is characterized by the following performance [106]: $\lambda \sim 38$–430 µm, $\mathcal{R} \sim 700$, NEP $\sim 5 \times 10^{-20}$ W/$\sqrt{\text{Hz}}$. With this performance characteristics, BLISS promises to optimize capability for spectroscopic follow-up of distant galaxies with unknown redshifts and become an important capability for SPICA [53]. However, this performance levels do not appear to fully meet the requirements for new astrophysical technology development shown in Table 2.2. In addition, its large size determined by the Z-Spec modules makes BLISS sub-optimal when compared with more compact spectrometers.

A last comparison can be made with one-dimensional bootlace lenses found in microwave practice [107–110]. A bootlace lens is made of a feed array, an inner surface array, and a radiating array whose elements are connected to those of the inner surface array by transmission lines. µ-Spec builds upon this technology for submillimeter wave applications.

To conclude this review of spectrography's state of the art, it is worth mentioning the development of narrow-band filter-bank spectrometers, which are used at millimeter wavelengths and do not rely on optical interference as in grating or Fabry-Perot spectrometers. Examples are SuperSpec [111–113], the Delft SRON High-redshift Mapper (DESHIMA) [114, 115], the CAMbridge Emission Line Surveyor (CAMELS) [116], and similar alternatives realized in rectangular waveguides (e.g., W-Spec [117]).

4.2 Design methodology

The design of the spectrometer multimode region was performed by building upon existing methods. Specifically, in the case of the Rowland spectrometer [96], two points on the focal surface can be chosen with wavelengths assigned to them. The x and y positions of the grooves in the grating can be selected to provide zero phase error at each of these points on the focal plane, which are called stigmatic points (see for example [102]). A similar constructive

approach can be used in the case of μ-Spec, where each emitter has an additional degree of freedom, the phase shift at the radiator, which allows generating a third stigmatic point. When the position of the stigmatic points on the focal plane is not preselected but left as another degree of freedom, designs with four stigmatic points become possible.

In order to answer Question 2 presented at the beginning of this chapter, the design methodology for 2-stigmatic-point configurations was generalized to accommodate such additional degrees of freedom and employed to generate different designs. The following sections will describe the steps adopted and will illustrate five case studies.

4.3 Low-resolution 3-stigmatic-point solution

The design methodology was first developed for a prototype version with spectral resolution $\mathcal{R} = 65$ in first order ($M = 1$). This is described in detail in [61] and is reported in almost its entirety in the remainder of this section (4.3) as found in the aforementioned reference, with minor edits to improve clarity.

"A prototype version with three stigmatic points was initially designed that would fit four spectrometers in a 100-mm silicon wafer, each in a 25-mm × 25-mm region, with a maximum radius $R = 1.25$ cm. This choice is not optimal but enables several designs to be experimentally studied within a single mask set as well as the development of the required fabrication process. The overall design was therefore carried out with the parameters shown in Table 4.1, where values for an initial design (R65A) and its optimized version (R65B) here adopted as the baseline are shown.

The location of the three stigmatic points on the focal plane was fixed. As an initial step, one point was chosen at the center of the focal surface and two which are about 15% in from each end of the focal surface (Fig. 4.4). In the case of the Rowland grating, the selection of the wavelengths at the two stigmatic points determines the dispersion of the grating. In μ-Spec, the selection of the wavelengths of the three stigmatic points determines both the dispersion and the linearity of the dispersion of the system. A constraint on the selection is required if linear dispersion is desired. In the case described here, the stigmatic points and their associated wavelengths were picked to provide relatively linear dispersion

Table 4.1: Spectrometer parameter summary (Adapted from [61])

Global Design Parameters:			
Minimum frequency, $f_1 = c/\lambda_{o1}$		450	[GHz]
Maximum frequency, $f_2 = c/\lambda_{o2}$		650	[GHz]
Silicon, relative permittivity, ε_r		11.7	
Maximum wavelength in silicon, $\lambda_1 = \lambda_{o1}/\sqrt{\varepsilon_r \mu_r}$		195	[µm]
Minimum wavelength in silicon, $\lambda_2 = \lambda_{o2}/\sqrt{\varepsilon_r \mu_r}$		135	[µm]
Blaze point wavelength in silicon, $\lambda_B = \sqrt{\lambda_1 \lambda_2}$		164	[µm]
Resolving power, $\mathcal{R}$		65	
Grating Order, M		1	
Design Variation:	A	B	
Number of emitters, N_e	65	65	
Number of receivers, N_r	47	65	
Antenna array element spacing or pitch, p	179	161	[µm]
Multimode region, physical radius, R	1.25	1.05	[cm]

Note: speed of light in vacuum, $c = 3.0 \times 10^8$ m/s.

and good imaging over the wavelength range of interest. The positions and wavelengths of the stigmatic points are free parameters and can be selected to optimize aspects of the instrument performance. A reasonable choice, which is adopted here, is to select points that minimize the overall root-mean-square (RMS) phase error for all spectrometer outputs.

Having chosen these nine parameters, i.e., the x and y coordinates of the three stigmatic points and their wavelengths, it is then possible to proceed with the determination of the locations and phase shifts of the radiators. The geometry of a Rowland spectrograph is taken as a starting point, with the radiators on a surface of radius $2R$, and the detectors on a circle of radius R at a distance of $2R$ from the center of the radiators. The spacing of the radiators is not constrained and will be chosen to limit diffraction losses. The procedure begins with a first radiator near the center of the radiator circle. Next, after choosing an adjacent radiator, its position and differential phase are perturbed, which results in arriving at each of the three stigmatic points. This procedure is continued for the radiators on each of the delay lines. This method results in good optical performance, with zero phase error at the stigmatic points by construction, low RMS phase errors between the stigmatic points, and diffraction-limited performance in the multimode region over the design spectral range.

With these parameters, the design procedure described was implemented in MATLAB

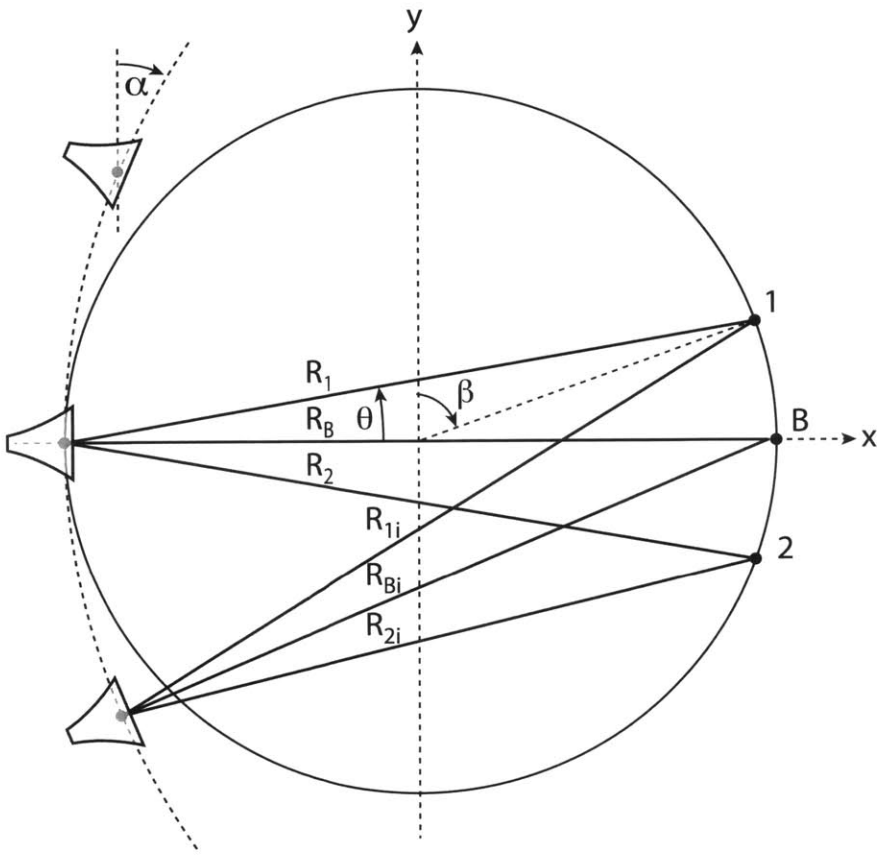

Figure 4.4: Simplified representation of the grating geometry. On the left side three radiators can be seen, which point to the blaze point, B. The path from each radiator's phase center to the first and second stigmatic points are also indicated by solid lines for the array's i^{th} and central reference feed. Adapted from [61].

through the goal attainment method of Gembicki [118]. This method was chosen because its implementation enables the resolution of vectorial equations subject to non-linear constraints which arise in the case presented in this paper. The following set of equations describes the propagation of light through the spectrometer,

$$F_m(\mathbf{x}) = F_m^*, \quad m = 1, ..., 3N_e, \tag{4.1}$$

where F_m represents the electrical delay which must be equal to F_m^*, an integer multiple of the wavelengths, at the three stigmatic points. N_e represents the number of radiators and $3N_e$ equations are needed to calculate the electrical delay of all radiators at each of the three stigmatic points. The vector of the unknowns, $\mathbf{x}$, consists of the coordinates x_i and y_i of the N_e

emitters' centers, and the electrical path lengths in silicon, R_i^e, for each feed horn delay line.

Constraints are necessary to limit the search of the solution in the correct parameter space. In fact, each of the system's equations is of order 2 and the search of the solution was restricted within $\lambda_1/40$ from the geometric optics solution for the grating solution (the $2R$ dotted arc on the left side of Fig. 4.4). Using a numerical as opposed to an analytical solution thus allows us to analyze and incorporate the channel isolation and higher-order diffractive response into the optimization (see Sec. 4.3.1). Indeed, while the feed phase centers reside on the position of the analytical solution, it will be shown that the array response is not uniform in angle.

All quantities in Eq. (4.1) are defined as follows:

$$F(\mathbf{x}) = \begin{bmatrix} R_i^e + R_{1i}^e - R_1^e \\ R_i^e + R_{2i}^e - R_2^e \\ R_i^e + R_{Bi}^e - R_B^e \end{bmatrix} \quad i = 1, ..., N_e$$

is the light path function matrix ($3N_e \times 1$), whose first $2N_e$ rows are associated with stigmatic points 1 and 2 respectively, and the last N_e rows with the blaze point B. All quantities in the $F(\mathbf{x})$ matrix represent electrical lengths in the transmission medium. For example, the terms in the first N_e rows associated with stigmatic point 1 are indicated below:

- R_i^e is the electrical path length of the i-th silicon microstrip delay line;
- $R_{1i}^e = \left[\sqrt{(R\sin\beta_1 - x_i)^2 + (R\cos\beta_1 - y_i)^2}\right] \times \sqrt{\varepsilon_r \mu_r}$, is the electrical path length of the i-th feed horn from stigmatic point 1 in the silicon parallel-plate waveguide multimode region;
- $R_1^e = \left[R\sqrt{(1+\sin\beta_1)^2 + \cos^2\beta_1}\right] \times \sqrt{\varepsilon_r \mu_r}$, is the reference electrical path length of stigmatic point 1 from the central feed horn $[i = (N_e+1)/2]$, in the silicon multimode region.

A 0.45-μm-thick monocrystalline silicon dielectric substrate is employed on the chip. The electrical length in the parallel-plate waveguide region is computed from the product of the index of refraction in the medium and the physical length defined by the geometry in Fig. 4.4.

For example, $R_{1i}^{e} = R_{1i}\sqrt{\varepsilon_r \mu_r}$, where ε_r and $\mu_r \approx 1$ are the effective relative permittivity and permeability specifying the propagation in the guiding medium. The parallel-plate waveguide conductor and ground plane are well approximated and modeled as perfect electric conductors (PEC). A surface reactance was assigned to the superconductor (niobium) to account for the kinetic inductance and model its influence on the impedance and propagation constant in the microstrip transmission line structures. The superconducting material was modeled as a 0.2-μm-thick layer with a London penetration depth $\lambda_L = 95$ nm [119]. Similar definitions apply to stigmatic point 2 and the blaze point B. Finally,

$$F^* = \begin{bmatrix} \left(i - \frac{N_e+1}{2}\right) M\lambda_{o1} \\ \left(i - \frac{N_e+1}{2}\right) M\lambda_{o2} \\ \left(i - \frac{N_e+1}{2}\right) M\lambda_{oB} \end{bmatrix} \quad i = 1, ..., N_e$$

where $M = 1$ represents the order of the grating chosen for this design and λ_o the free-space wavelengths of the three stigmatic points. Here, the presence of subscript "o" signifies the radiation wavelength in free space and without indicates in the dielectric medium as defined in Table 4.1. In order to maximize the instrument efficiency, the emitters are tilted by an angle α so as to point to the center of the focal surface (Fig. 4.4):

$$\alpha_i = -\arctan\left(\frac{y_i}{|x_i| + R}\right). \tag{4.2}$$

A particular solution is found when placing the emitter antennas on the $2R$ circle, using an axisymmetric configuration, and placing the blaze point on the optical axis. This provides a partial diagonalization of the problem, as in [107]. Under these hypotheses, indeed, the last N_e equations of (4.1), which refer to the blaze point, can be explicitly rewritten as shown below:

$$R_i^e + \left[\sqrt{(R\sin\beta_B - x_i)^2 + (R\cos\beta_B - y_i)^2} - R_B\right] \times \sqrt{\varepsilon_r \mu_r} = \left(i - \frac{N_e+1}{2}\right) M\lambda_{oB}, \tag{4.3}$$

where β_B is the angle between the y axis and the line from the center of the Rowland circle

to the blaze point (Fig. 4.4). Here $\beta_B = \pi/2$, which yields:

$$R_i^e + \left[\sqrt{(R - x_i)^2 + y_i^2} - R_B\right] \times \sqrt{\varepsilon_r \mu_r} = \left(i - \frac{N_e + 1}{2}\right) M \lambda_{oB}. \tag{4.4}$$

Now, the terms $\sqrt{(R - x_i)^2 + y_i^2}$ express the distance of the i-th feed horn from the blaze point. Because the emitters lie on the $2R$ circle, this quantity is exactly equal to $2R$. Also R_B is equal to $2R$ given the axisymmetric configuration of the instrument and the particular location chosen for the blaze point. Therefore, these two terms cancel out and one readily obtains:

$$R_i^e = M \lambda_{oB} \left(i - \frac{N_e + 1}{2}\right), f \tag{4.5}$$

which is a linear relation between the electric length in silicon, R_i^e, and the feed horn number, i.

To find the precise spacings of the emitters along the grating circle needed in order to satisfy the stigmatic equation for the pair of symmetric off-axis stigmatic points at the specified high and low wavelengths, our numerical solution method shows that the spacing between adjacent antennas is not a constant but grows quadratically as a function of position. In design R65A, a change of ~ 13 µm from the nominal design value, $p = 179$ µm, is observed. This is the same behavior found by Rotman and Turner [107], who derived an analytical solution for the analogous design of a bootlace lens, and found that the problem reduces to solving an ordinary quadratic equation, from which one can determine the antenna positions.

As mentioned in the beginning of this section, the diffractive solution can be found by restricting the algorithm to searching for radiator positions within a limited distance from the ideal Rowland circle. The constraint reads:

$$\left|\sqrt{(x_i - R)^2 + y_i^2} - (2R + z)\right| \leq \lambda_1/40, \tag{4.6}$$

where z is the phase center correction provided by finite-element simulations ($z = 15$ µm, see Sec. 4.3.2) and $\lambda_1/40 \sim 5$ µm is chosen to provide the upper and lower bounds. This is equivalent to a phase error of $(2\pi/\lambda_{o1}) \times (\lambda_{o1}/40)$ rad $\sim 1/6$ rad.

The RMS phase error, φ_{RMS}, is illustrated in Fig. 4.5 for design R65A and it was cal-

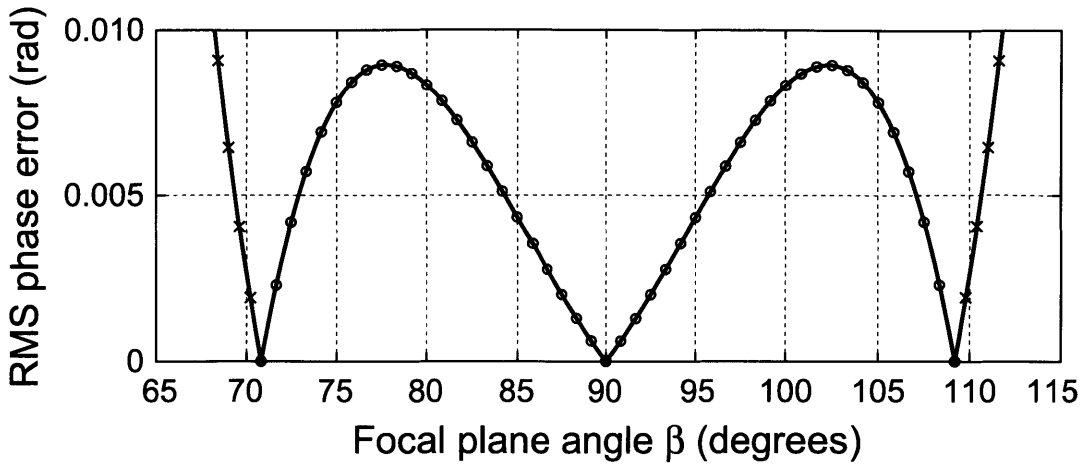

Figure 4.5: RMS phase error between the average and the phase of all other transmit feed paths evaluated as a function of receiver position with the design parameters in Table 4.1 for design R65A. The RMS phase error vanishes at the three stigmatic points by construction and remains low in between. This ensures diffraction-limited performance over the power combiner's design spectral range. The feed positions for the receive array in this design configuration are indicated by circular symbols in the figure. Addition of the radiators indicated by crosses can be used to improve the throughput in future implementations. Adapted from [61].

culated by assuming a uniform weight for each radiator at each point on the focal plane:

$$\varphi_{RMS}(\theta_j) = \left[\sum_{i=1}^{N_e} \frac{(\varphi_{ij} - \langle\varphi(\theta_j)\rangle)^2}{N_e}\right]^{1/2}. \tag{4.7}$$

Here, φ_{ij} is the relative phase of each transmitter, $\langle\varphi(\theta_j)\rangle = 0$ is the relative phase of the central transmitter (this is zero by construction as the central radiator is used as a reference, i.e., $F^*_{(N_e+1)/2} \equiv 0$), N_e is the number of transmitters, and θ_j represents the angle corresponding to each of the points in which the focal plane was discretized. The phase between the i-th transmitter and the j-th point on the receiver focal plane is defined as $\varphi_{ij} = 2\pi\sqrt{\varepsilon_r\mu_r}/\lambda_{oj} \times F_i$ and λ_{oj} is the free-space wavelength." [61] The relation between the two angles, θ and β, is readily derived from geometric considerations (Fig. 4.4) and is as follows:

$$\tan\beta = \frac{\cos\theta}{1+\sin\theta}, \text{ for } \theta > 0, \tag{4.8}$$

$$\tan(\pi-\beta) = \frac{\cos\theta}{1+\sin\theta}, \text{ for } \theta < 0. \tag{4.9}$$

4.3.1 Antenna feed response

"Conceptually, each microstrip feed structure is a two-dimensional analog of an adiabatic feed horn. To achieve the desired performance, the feed needs to match impedance, modal shape, and angular resolution over the design frequency band. An adiabatic impedance taper [120] for the input microstrip line width to the output is achieved via a Hecken taper [121], which is a near-optimum matching section in the sense that it approaches an "equal-ripple" response without the use of abrupt discontinuities. These properties lower its sensitivity to fabrication variations and tolerances. This feed section serves as a transition between microstrip lines and parallel-plate TEM waveguide regions. The latter is commonly referred to as the parallel-plate guide, and the microstrip planar waveguide model [65] can be used to compute its propagation and impedance properties. The transformer ratio, effective dielectric constant, and desired return loss set the necessary length of the impedance taper and were synthesized from readily available analytical forms and the response numerically simulated. A diagram of the feed aperture and spacing geometry is provided in the insert of Fig. 4.6 (left). In illuminating the multimode dielectric-filled parallel-plate waveguide region, the microstrip outputs play the role of the antenna apertures and need to be sized to minimize diffraction at the upper band edge.

When used as a two-dimensional antenna element, the aperture geometry not only sets the radiation pattern but also plays a role in determining the return loss [122]. This can be seen by the following consideration: the angular acceptance of the structure is constant over the band since the wavelength in the medium is less than the effective aperture width, w. Considering the scaling of the reflection amplitude as a function of feed size [123], the desire for a low return loss at the low end of the band is in tension with the needs to limit diffraction ($w < \lambda_o/\sqrt{\varepsilon_r \mu_r}$) and efficiently radiate ($w > \lambda_o/2\sqrt{\varepsilon_r \mu_r}$). This behavior effectively determines the smallest aperture size which can effectively radiate [124]. The reflection from the end of the microstrip taper scales as a power of the wavelength over the microstrip width in two dimensions and is larger than that arising from the impedance taper, which can readily be made sub-dominant by increasing the transformer's length. Thus, to address the reflection from the aperture, the output geometry of the aperture was apodized

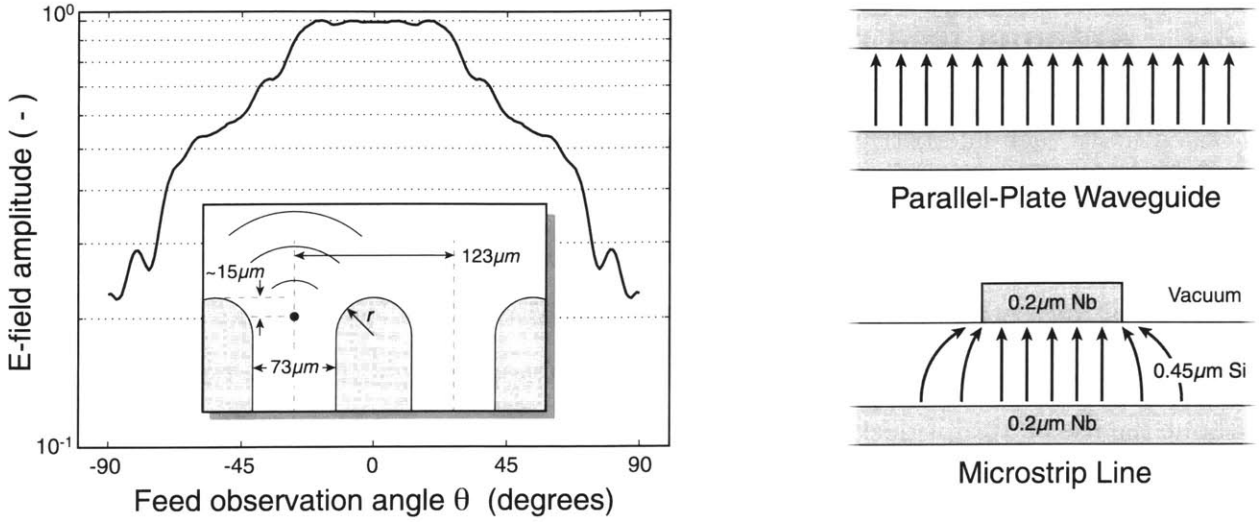

Figure 4.6: (Left) The computed feed horn angular response at 430 GHz. The response of an emitting feed (aperture size 73 μm) is evaluated in the far field ($\|\mathbf{r}\| \sim 6\lambda = 438$ μm) and normalized to the magnitude of the E field at zero degrees. The feed array geometry is provided in the figure insert. The feed's phase center is indicated by a black filled circle. (Right) Cross section of the parallel-plate waveguide (upper) and microstrip (lower) transmission line geometries. The electric field is depicted with arrows to indicate the dominant modal symmetry. An adiabatic transition serves as a mode converter between these modes and defines the feed's angular response in the multimode power combined region. Adapted from [61].

by adding a constant radius flare [125]. The resulting radiator element return loss, > 20 dB, is achieved over a 2:1 bandwidth. Over the wavelength range where $2p < \lambda$, only the first-order diffraction occurs [109]. The influence of higher-order diffraction is mitigated through the feed apodization, the coupling geometry of arrays, and the use of absorbing boundaries on the multimode region walls." [61]

4.3.2 Antenna array response

"An efficient and accurate expression is desired for the evaluation of the structure's response during numerical optimization. To evaluate the antenna array's response, a classical phased array analysis approach is used in which the emitters and receivers in the multimode region can be considered as a pair of opposing 2-dimensional antenna arrays. By considering the Poynting vector as a function of spatial dimension, d, the following expression for the electric

field is adopted for the computation of the array's response:

$$\mathbf{E}(\mathbf{r}) = \sum_{i=1}^{N_e} \frac{E_0(\theta_j)}{\left[1 + \left(\frac{\|\mathbf{r}\|}{w}\right)^2\right]^{(d-1)/4}} \cdot e^{j(\mathbf{k}\cdot\mathbf{r} - \varphi_{ij})}. \tag{4.10}$$

Here, $\mathbf{r}$ is the separation distance vector between the center point of the i-th emitter and a point in the multimode region, E_0 is the E-field amplitude from the beam pattern angular distribution (θ_j) at the center of the i-th feed horn (Fig. 4.6), w is the effective width of the feed horns, $\mathbf{k} = (2\pi\sqrt{\varepsilon_r\mu_r}/\lambda_o) \cdot \mathbf{n}_i$ is the wavenumber vector in the medium, and $\mathbf{n}_i$ is the unity vector normal to the i-th emitter. The phase φ_{ij} includes the contributions arising from the feed aperture's phase, the phase delay, and the reference to the central emitter.

The field amplitude's dependence on radial separation is physically motivated by the behavior of the fields in transitioning from the near to the far field [126]. Close in to the feed aperture the fields are essentially constant, and in going to large distance the amplitude decreases with distance. Physically useful limiting cases to consider are $d = 3$, which yields a scaling of the E-field inversely with distance for a spherical wave, and $d = 1$, which yields a scaling independent of distance for a lossless transmission line. For $d = 2$, the case of primary interest here, it is important to note that the E-field amplitude scales as the square root of the separation distance, $\|\mathbf{r}\|$, and is anticipated for a cylindrical geometry from the asymptotic form of the Hankel functions. This expression conserves power flow, is analytic over the parameter range of interest, and is a computationally efficient representation of the structure's behavior during synthesis of the array response. The functional form and scaling indicated in Eq. (4.10) were validated by High-Frequency Structure Simulation (HFSS) finite-element simulations of the structure's response with distance. These simulations were used to derive the feed aperture's effective width, w, and to determine the location of the phase center for radiation emitted by the structure.

The power is then computed from

$$P(\mathbf{r}) = \frac{1}{2\eta}\mathbf{E}^*(\mathbf{r}) \cdot \mathbf{E}(\mathbf{r}), \qquad \eta = \left(\frac{\mu_r}{\varepsilon_r}\right)^{1/2} \eta_o, \tag{4.11}$$

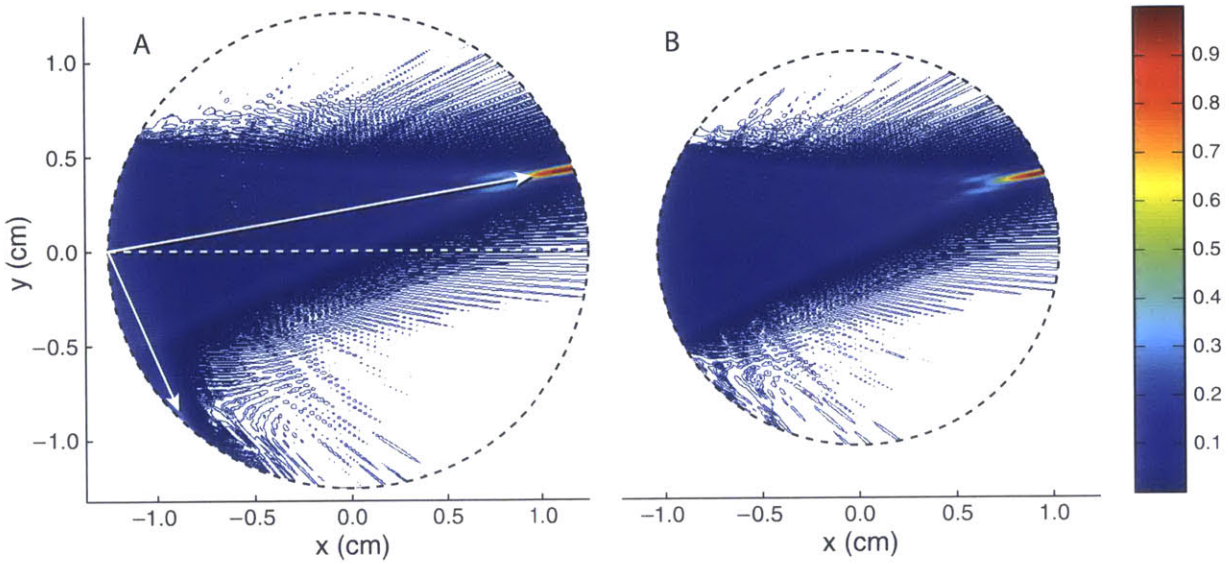

Figure 4.7: Power distribution in the multimode region at a frequency of 450 GHz. On the left (Design R65A), the first-order peak is visible at an angle $\theta \approx 10\,^\circ$, whereas the second-order diffraction peak shows up at $\theta \approx -66\,^\circ$ (θ is defined in Fig. 4.4). In the optimized version (Design R65B) on the right, the higher-order diffraction peak has now disappeared and the throughput is as high as 87%. Adapted from [61].

where $\eta_o = 377\ \Omega$ is the wave impedance of free space." [61] Equation (4.11) also allows one to calculate the coupling efficiency between receivers and transmitters for any given design, as well as the ratio of the power in each receiver to the power in the first receiver. This gives an estimate of the isolation between channels, thereby suggesting the correlation existing between adjacent spectrometer channels. These parameters will be useful for checking whether the structure's optical throughput is maximized under the assumption that the design fully samples the spectrum, and will provide answers to the second part of Question 2 at the beginning of this chapter: What are the trade-offs involved in this design? How can the instrument performance be optimized in terms of coupling efficiency and spectral purity?

"Figure 4.7 illustrates the power distribution at 450 GHz, as was calculated from Eqs. (4.11) and (4.10). On the left side, it can be seen that the power peaks at the first stigmatic point as required, and then it quickly drops to zero along the rest of the focal plane. At separations from the feed elements greater than ~ 2 mm, the field transitions to the far field and the electric field amplitude is observed to asymptotically fall as $\|\mathbf{r}\|^{-1/2}$. Simulations show the power is conserved throughout the multimode region. In design example R65A, the ratio

of the power emitted by the feed horns to the power received by the antennas is equal to $\sim 30\%$. The feed response which is not intercepted by the antenna arrays is terminated by the absorber structures on the sides of the multimode region. This also enables any residual reflected power to be terminated in a controlled manner. In addition, a second-order diffraction peak, visible in the lower lefthand quadrant near the emitters, is responsible for part of this loss.

Improved performance can be achieved with different trade-offs between the antennas and the array geometry, which increase the throughput and reduce the effects of diffraction (see Table 4.1, Design R65B). If the two stigmatic points are moved away from the blaze point on the optical axis along the Rowland circle by 4.2%, the instrument reaches its highest efficiency of 87% when the following applies: the radius is decreased by 16% ($R = 1.05$ cm), the number of receivers is increased by 18 ($N_r = 65$), and the emitter pitch, p, is set to 161 µm. The resulting increase in the receiver array acceptance angle is better matched to capture the transmitted beams given the apodization function of the radiators. This is the primary reason for the multimode coupling-efficiency increase observed in this example. As an aside, this change in array geometry reduces the magnitude of the second-order diffraction peak and moves it out of the range of angles of interest. For additional detail, see Fig. 4.7, rightmost inset.

Fig. 4.8a shows the emitter antenna array's normalized power response evaluated at the three stigmatic wavelengths for the optimized multimode region design. Table 4.2 summarizes the coupling efficiency between receiver and transmitter antenna arrays for the two design variations considered in this section. The inter-channel power isolation is presented in Fig. 4.8b for the center channel of the optimized design. The observed finite isolation, < 0.48, arises from the design goal to fully sample the spectrum and maximize the structure's optical throughput. The resulting signal correlation can be addressed in calibration of the spectrometer response. Finally, the RMS phase error now reaches a maximum of 0.011 at $\beta = 75.8°$ and 104.3°, and vanishes at the three stigmatic points ($\beta = 67.8°$, 90° and 112.2°)." [61]

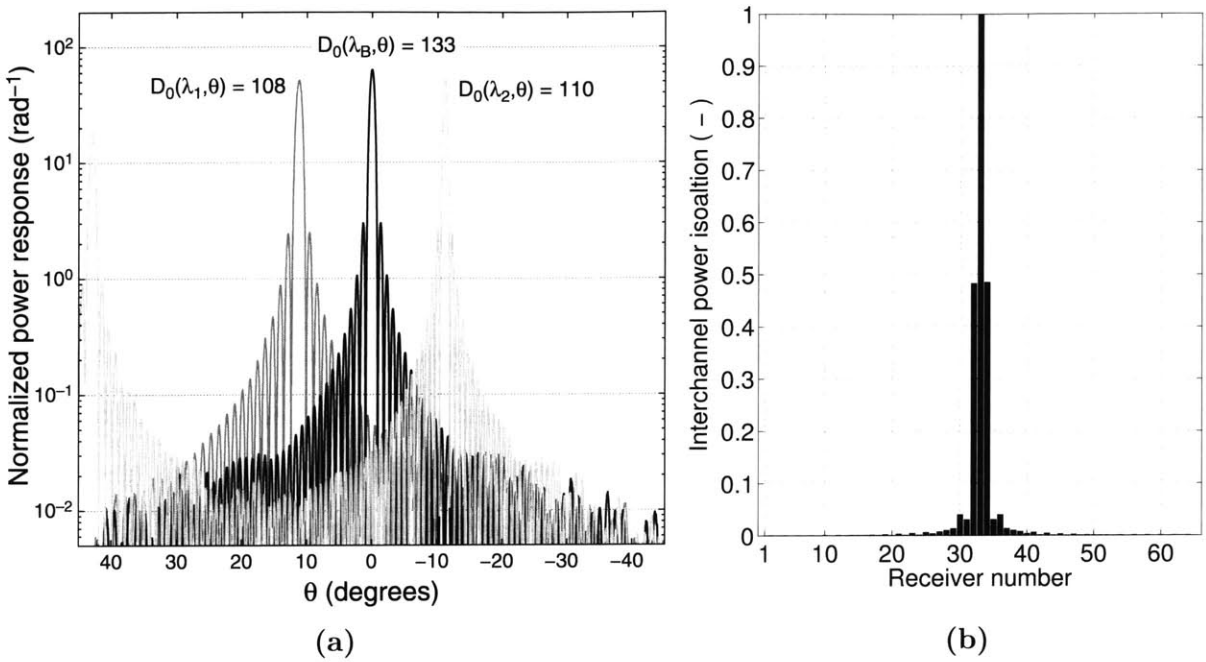

Figure 4.8: Design R65B angular response. (a) The emitter antenna array's angular power response is normalized by the total radiated power and plotted for the three stigmatic wavelengths. The peak directivity $D_0(\lambda, \theta)$ is the angular response of the array relative to an isotropic radiator and is indicated on the plot. (b) Power isolation between the receiver channels computed for $\lambda_o \sim 560$ µm, where the power in each channel is normalized to the power in the central channel. Adapted from [61].

Table 4.2: Computed coupling efficiency ($2p > \lambda$) (Adapted from [61])

Signal frequency [GHz]	Guide wavelength [µm]	Coupling efficiency Design R65A [−]	Coupling efficiency Design R65B [−]
450	$\lambda_1 = 195$	0.30	0.91
541	$\lambda_B = 164$	0.30	0.87
650	$\lambda_2 = 135$	0.34	0.55

4.3.3 The R65 built hardware

The R65A design was used to build and test a prototype at NASA's Goddard Space Flight Center. The hardware is shown in Fig. 4.9, where all the subsystems can be seen, including, from left to right, the power divider, the delay network, the multimode region, and the MKIDs.

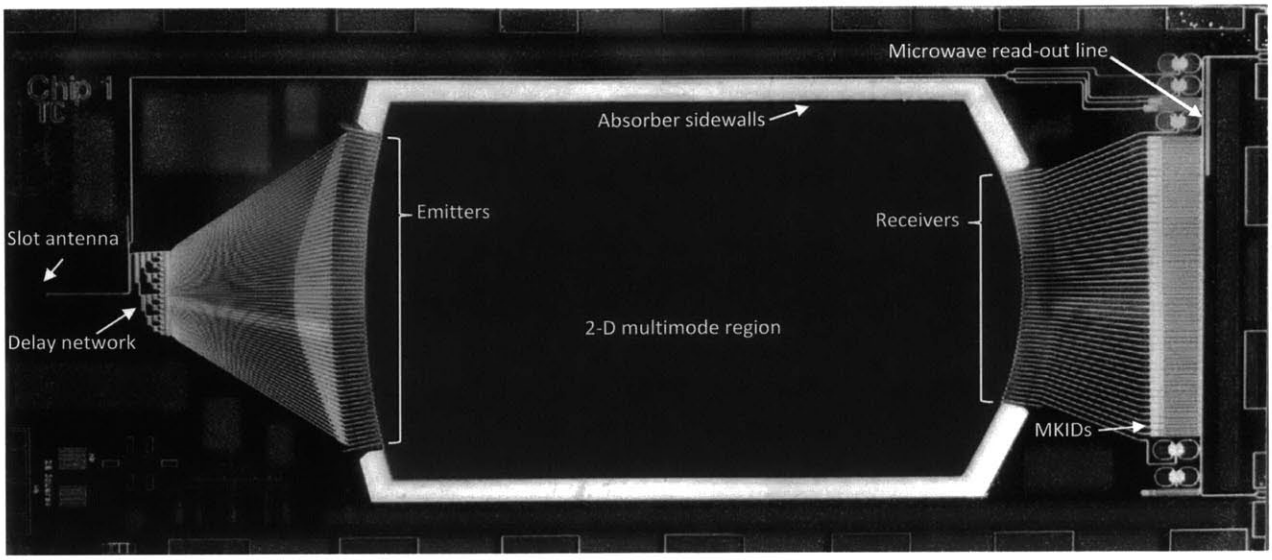

Figure 4.9: The built version of the Micro-Spec R65 spectrometer based on the design described in Section 4.3.

4.4 Higher-resolution 3-stigmatic-point solutions

In this section, designs are presented for $\mathcal{R} = 260$ (Design R260) and $\mathcal{R} = 520$ (Design R520) in higher order ($M > 1$) with zero phase error at three preselected stigmatic points. These designs were obtained through a multi-step optimization process described in detail in [127] and reported below in Sections 4.4.1–4.4.4 with minor edits to improve clarity.

4.4.1 Problem formulation

"As explained in [61], the design variables are the x and y coordinates of the N_e emitters' centers and the electrical path lengths in silicon, R_i^e, for each feed's electrical delay. The resolving power is explicitly defined as

$$\mathcal{R} = M \cdot N_e, \tag{4.12}$$

where M is the order of the spectrometer and N_e is some power of 2, given the structure of the power divider network (see Fig. 2.1). The first step of the design consists of finding the maximum achievable resolving power, $\mathcal{R}_{max}$, as a function of M and the relative emitter

pitch, $\eta = p/\lambda_B$ (p = emitter pitch, λ_B = wavelength associated with the central stigmatic point on the x axis – see Fig. 4.4), given specific requirements on spectrometer radius, R, and operating spectral range as well as certain constraints on performance.

The formulation of this mixed integer non-linear problem is as follows:

$$\begin{aligned}
\max \mathcal{R}_{max}(M,\eta) &= M/\eta \cdot R/\lambda_B && (4.13)\\
\text{subject to} \quad H_e(M,\eta) &\leq R && (4.14)\\
H_r(M,\eta) &\leq R && (4.15)\\
\mathcal{R}_{max}(M,\eta) &> 64 && (4.16)\\
p(M,\eta) &= s(M,\eta) && (4.17)\\
\eta &> 0 && (4.18)\\
1 \leq M &\leq 10, \quad M \text{ integer} && (4.19)
\end{aligned}$$

Equations (4.14)–(4.15) ensure that aberration will be fine by imposing that the width of the the emitter, H_e, and receiver, H_r, arrays be less than or equal to the spectrometer radius, R. Equation (4.16) allows looking for solutions whose maximum resolving power is greater than 64, while [Eq. (4.17) was used to simplify the positioning of the receivers on the focal plane by imposing that the receiver pitch be equal to the emitter pitch. This constraint may be removed in future designs. The entire problem was solved with a Branch and Bound algorithm [128] using the open-source Interior Point OPTimizer (IPOPT) [129] and Coin-or Branch and Cut (CBC) [130] solvers.]

The objective spaces as a function of M and η for the two cases, $\mathcal{R} = 260$ and $\mathcal{R} = 520$, are shown in Figs. 4.10–4.11, respectively. On the left (Figs. 4.10a–4.11a), it is possible to visualize the feasible objective space of the optimization problem described above for $\mathcal{R}_{max}$ along with the active constraints, Eq. (4.15) (blue area) and Eq. (4.17) (black lines). The optimal solution to Problem (4.13) is thus given by the intersection of the contour plot representing the feasible values of $\mathcal{R}_{max}$ and Constraint (4.17) (lower black line).

Table 4.3 shows the requirements on spectrometer size and spectral range for the two cases. The minimum and maximum frequencies are associated with stigmatic points 2 and

1 respectively, whereas the average frequency, computed as their geometric mean, is associated with the blaze point, B (Fig. 4.4). Table 4.4 shows the values of the design variables associated with the optimal solutions as well as the values of the constraints, which are all satisfied.

Once this problem is solved, it is then possible to compute $N_e = \mathcal{R}_{max}/M$ and round this down to a power of 2. According to Eq. (4.12), this causes the actual resolving power, calculated with this updated value of N_e, to be lower than $\mathcal{R}_{max}$. The plots in Figs. 4.10b-4.11b show the values of the actual resolving power $\mathcal{R}$ (red line) and the values of M and η that would make such realizations possible.

Table 4.3: Requirements on spectrometer size and spectral range (Adapted from [127])

Parameter	**Symbol**	**Unit**	**Value (R260)**	**Value (R520)**
Multimode region radius	R	cm	1.25	1.25
Minimum frequency	f_{min}	GHz	570.0 ($M = 4$)	605.0 ($M = 8$)
Maximum frequency	f_{max}	GHz	650.0 ($M = 4$)	650.0 ($M = 8$)
Average frequency	f_{avg}	GHz	608.7 ($M = 4$)	627.1 ($M = 8$)
Minimum frequency	f_{min}	GHz	142.5 ($M = 1$)	302.5 ($M = 4$)
Maximum frequency	f_{max}	GHz	162.5 ($M = 1$)	325.0 ($M = 4$)
Average frequency	f_{avg}	GHz	152.2 ($M = 1$)	313.5 ($M = 4$)

Table 4.4: Optimal solutions of Problem (4.13) for designs R260 and R520 (Adapted from [127])

Variable	**Symbol**	**Unit**	**Value (R260)**	**Value (R520)**
Spectrometer order	M	-	4	8
Emitter diameter	η	-	1.1634	1.1809
Maximum resolving power	$\mathcal{R}_{max}$	-	297.83	604.60
Emitter array width	H_e	cm	1.0912	1.0751
Receiver array width	H_r	cm	1.1297	1.2154
Emitter/receiver pitch	$p = s$	cm	0.0165	0.0163
Number of emitters	N_e	-	65	65
Number of receivers	N_r	-	87	91
Resolving power	$\mathcal{R}$	-	**260**	**520**

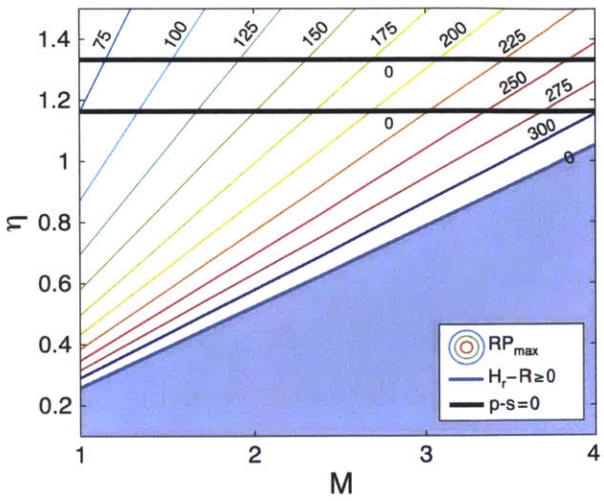

(a) The contour plot represents all feasible values of $\mathcal{R}_{max}$ and shows that the optimal solution is $\mathcal{R}_{max} \simeq 300$ for $M = 4$ and $\eta = 1.1634$.

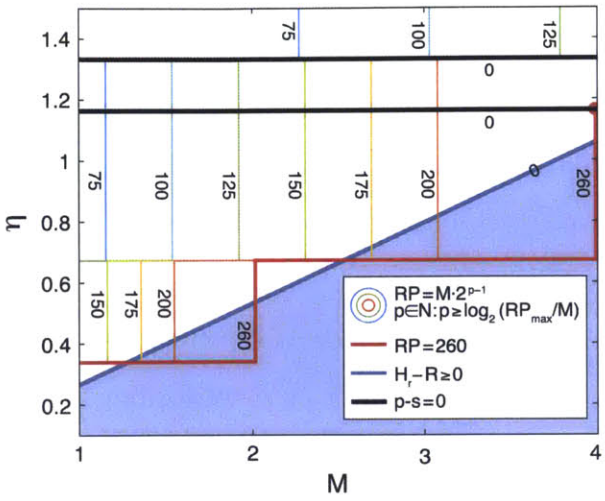

(b) The contour plot represents the feasible values of $\mathcal{R}$ for all orders given as powers of 2. The optimal solution for $M = 4$ and $\eta = 1.1634$ is associated with a resolving power $\mathcal{R} = 260$.

Figure 4.10: Objective spaces of Problem (4.13) for Design R260. The active constraints are Eq. (4.15) (blue area) and Eq. (4.17) (black lines). Both plots show that, for each order M, two feasible solutions exist which are associated with the two η values determined by Eq. (4.17) (black lines) with different resolving powers. Adapted from [127].

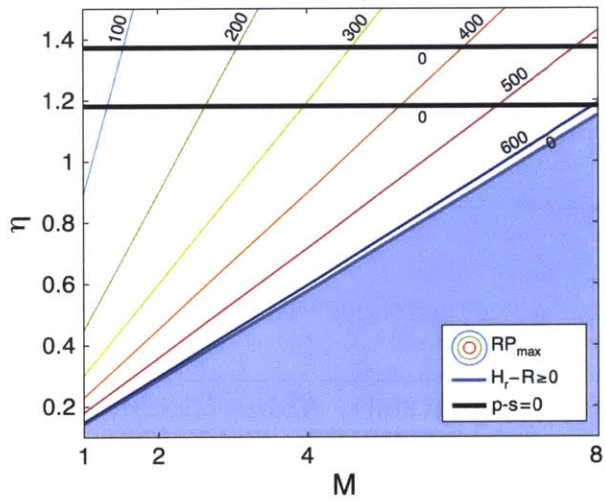

(a) The contour plot represents all feasible values of $\mathcal{R}_{max}$ and shows that the optimal solution is $\mathcal{R}_{max} \simeq 600$ for $M = 8$ and $\eta = 1.1809$.

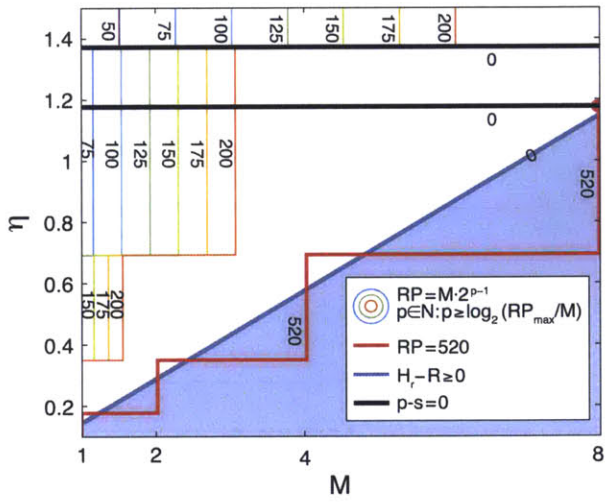

(b) The contour plot represents the feasible values of $\mathcal{R}$ for each order given as powers of 2. The optimal solution for $M = 8$ and $\eta = 1.1809$ is associated with a resolving power $\mathcal{R} = 520$.

Figure 4.11: Objective spaces of Problem (4.13) for Design R520. The active constraints are Eq. (4.15) (blue area) and Eq. (4.17) (black lines). Both plots show that, for each order M, two feasible solutions exist which are associated with the two η values determined by Eq. (4.17) (black lines) with different resolving powers. Adapted from [127].

The second step consists in minimizing the overall RMS phase error, φ_{RMS}, on the focal plane in order to determine the optimal solution in terms of the above-mentioned design variables.

$$\min \int_{\theta_1}^{\theta_2} \varphi_{RMS}\, \mathrm{d}\theta = \int_{\theta_1}^{\theta_2} \sqrt{\sum_{i=1}^{N_e} \frac{[\varphi_{ij}(x_i, y_i, R_i^e, \theta_j) - \langle\varphi(\theta_j)\rangle]^2}{N_e}}\, \mathrm{d}\theta \tag{4.20}$$

$$\text{subject to} \begin{cases} \varphi_{i1}(x_i, y_i, R_i^e, \theta_1) = 0 \\ \varphi_{i2}(x_i, y_i, R_i^e, \theta_2) = 0, \quad i = 1, ..., N_e \\ \varphi_{iB}(x_i, y_i, R_i^e, \theta_B) = 0 \end{cases} \tag{4.21}$$

Here, φ_{ij} is the relative phase of each transmitter, $\langle\varphi(\theta_j)\rangle = 0$ is the relative phase of the central transmitter (this is zero by construction as the central radiator is used as a reference) and θ_j represents the angle corresponding to each of the points in which the focal plane was discretized. θ_1, θ_2 and θ_B are associated with the three stigmatic points as depicted in Fig. 4.4." [127]

4.4.2 Optimization results

The solutions to the system of equations (4.20)-(4.21) for the two cases discussed in Sec. 4.4.1 were found with a sequential quadratic programming (SQP) algorithm with analytical computation of the constraints' Jacobian, and can be seen in Fig. 4.12. "The emitters' positions are indicated in red and present several characteristics which are worth discussing. First, they do not lie on the grating circle but on a curve that is tilted leftwards and intersects the grating circle at the central emitter before ending up inside the multimode region. It was verified that the shape of this curve only approximates a circle with a radius $\sim 2.2R$, is not symmetric and is caused by the imposition of zero RMS phase error on the blaze point, B, given by the last constraint in Eqs. (4.21). It was verified that if such a constraint is removed, the emitters lie exactly on the grating circle, as shown in the literature [96, 102]. In our previous work [61], this tilting effect was explicitly avoided by constraining all the emitters to lie within $\lambda_1/8$ from the $2R$ circle. Figure 4.12b shows also that it is less accentuated for the configuration in order $M = 8$.

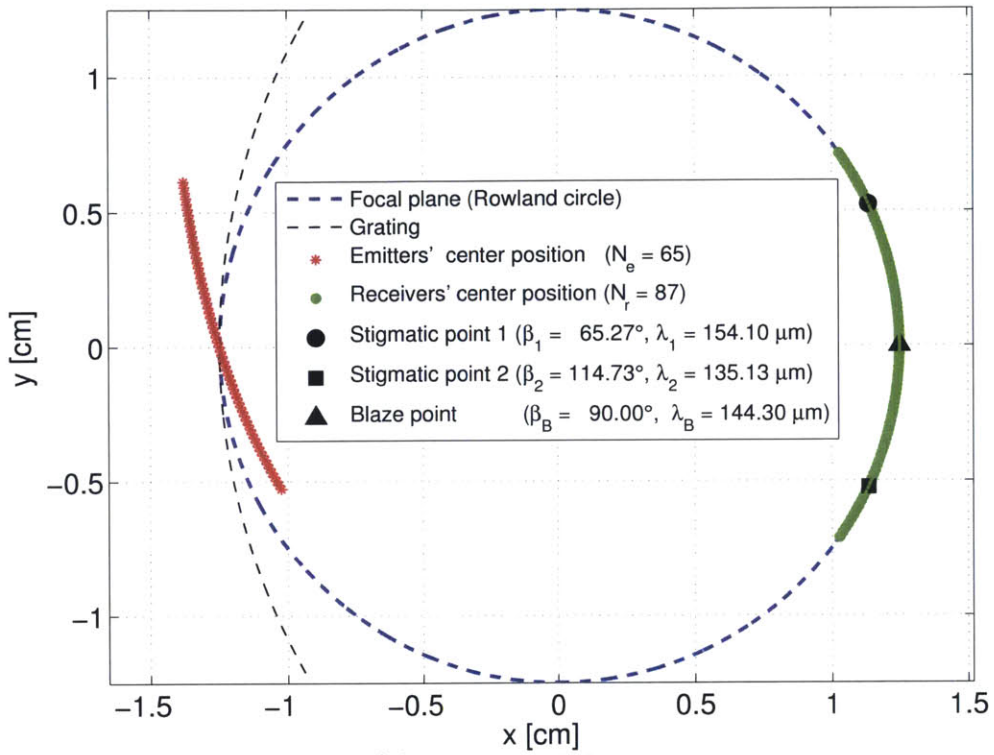

(a) $M = 4$ and $\mathcal{R} = 260$

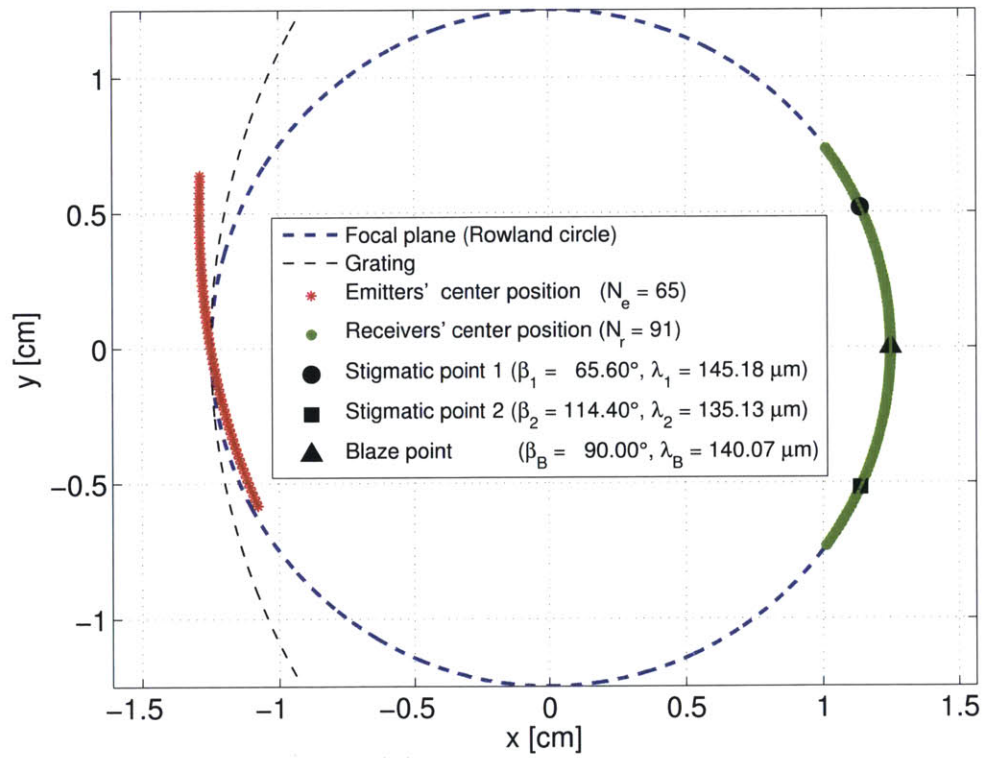

(b) $M = 8$ and $\mathcal{R} = 520$

Figure 4.12: Multimode region design for the two cases discussed above. Adapted from [127].

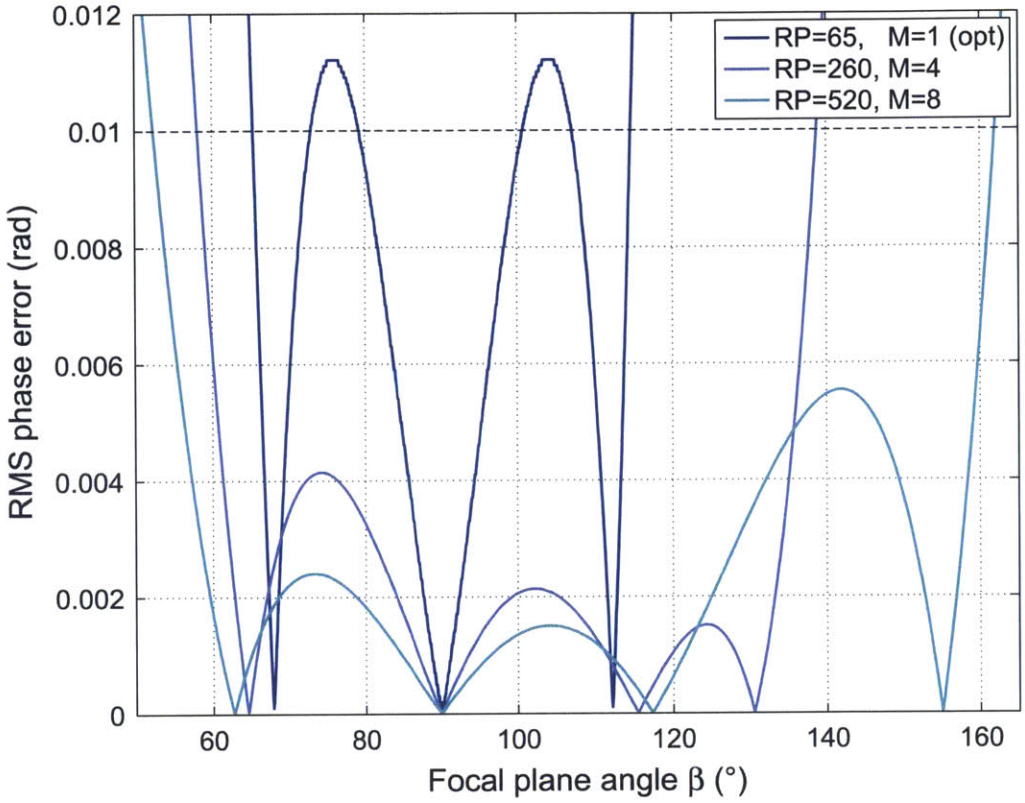

Figure 4.13: The RMS phase error for the two designs discussed in this section is compared to the optimized $\mathcal{R} = 65$ version presented in [61]. Adapted from [127].

The RMS phase error is shown in Fig. 4.13 for the two cases presented in this [section] and compared with that computed for the optimized $\mathcal{R} = 65$ version described in [61]. The new designs represent an improvement of no less than $\sim 64\%$ over the nominal spectral range indicated in Table 4.3. While the RMS phase error vanishes at the three imposed stigmatic points, it is worth noting the presence of a fourth stigmatic point for both designs at $\sim 130°$ and $\sim 155°$. It can be shown that, in general, the RMS phase error as defined in Eq. (4.20), is a fourth-order function of the focal plane angle, θ, and thus admits a maximum of 4 zeros. Here, equality constraints such as those in Eqs. (4.21) were only imposed on three points, leaving the fourth free because beyond the spectral range of interest. As a consequence, this does not affect the overall quality of the instrument for the specified requirements. Exploration of a configuration with 4 stigmatic points spanning a desired frequency range and such as to minimize the RMS phase error as defined in Eq. (4.20) is described in Sec. 4.5." [127]

4.4.3 Power coupling efficiency

The power coupling efficiency in the new design configurations was computed with the model described in [61, Sec. 4] as the ratio of the power received by the receiving antennas to the power emitted by the feed horns. The receiver spacing shown in Table 4.4 allows for Nyquist sampling, but the detailed coupling efficiency of the receiver feeds was not treated. For simplicity, the receiver port width is such that the feeds touch each other, thereby making the focal surface a continuous curve.

Figure 4.14 illustrates the values of the coupling efficiency for the $\mathcal{R} = 260$ (upper panel) and $\mathcal{R} = 520$ (top panel) designs over the spectral range of interest, i.e., 300–650 GHz. The bands covered by the receivers shown in Fig. 4.12 are indicated between vertical dashed lines and labeled with the order in use. By extending the receivers' coverage over the entire focal plane (i.e., $\theta_1 = -45°$, $\theta_2 = 45°$), it is possible to obtain a partial frequency overlap in different orders and a consequent increase in efficiency as well as a full spectral coverage. The coupling efficiency reaches its maximum values of $\sim 90\%$ when three peaks are simultaneously present on the focal plane. As the frequency shifts and the peaks rotate, one eventually leaves the focal plane and causes the efficiency to decrease to values as low as 30%. This behavior is expected by analogy with antenna phased arrays: as the angle is scanned, the main lobe of an order becomes the side lobe of an another, thereby decreasing the overall power captured by the receiver structures [131]. These low-efficiency gaps could be improved by redesigning the frequency bands associated with each order (see Table 4.4) and accounting for the detailed coupling efficiency of each single receiver.

4.4.4 Summary of findings

Section 4.4 discussed a design methodology for high-resolution configurations of the µ-Spec multimode region. The design procedure first maximizes the resolving power subject to constraints on geometry and operating frequency, thus determining the spectrometer's optimal order. In the second step, the RMS phase error on the instrument focal plane is minimized between three preselected stigmatic points. The two designs explored here achieve resolutions of 260 and 520 in fourth and eighth order, respectively, and exhibit a coupling efficiency of

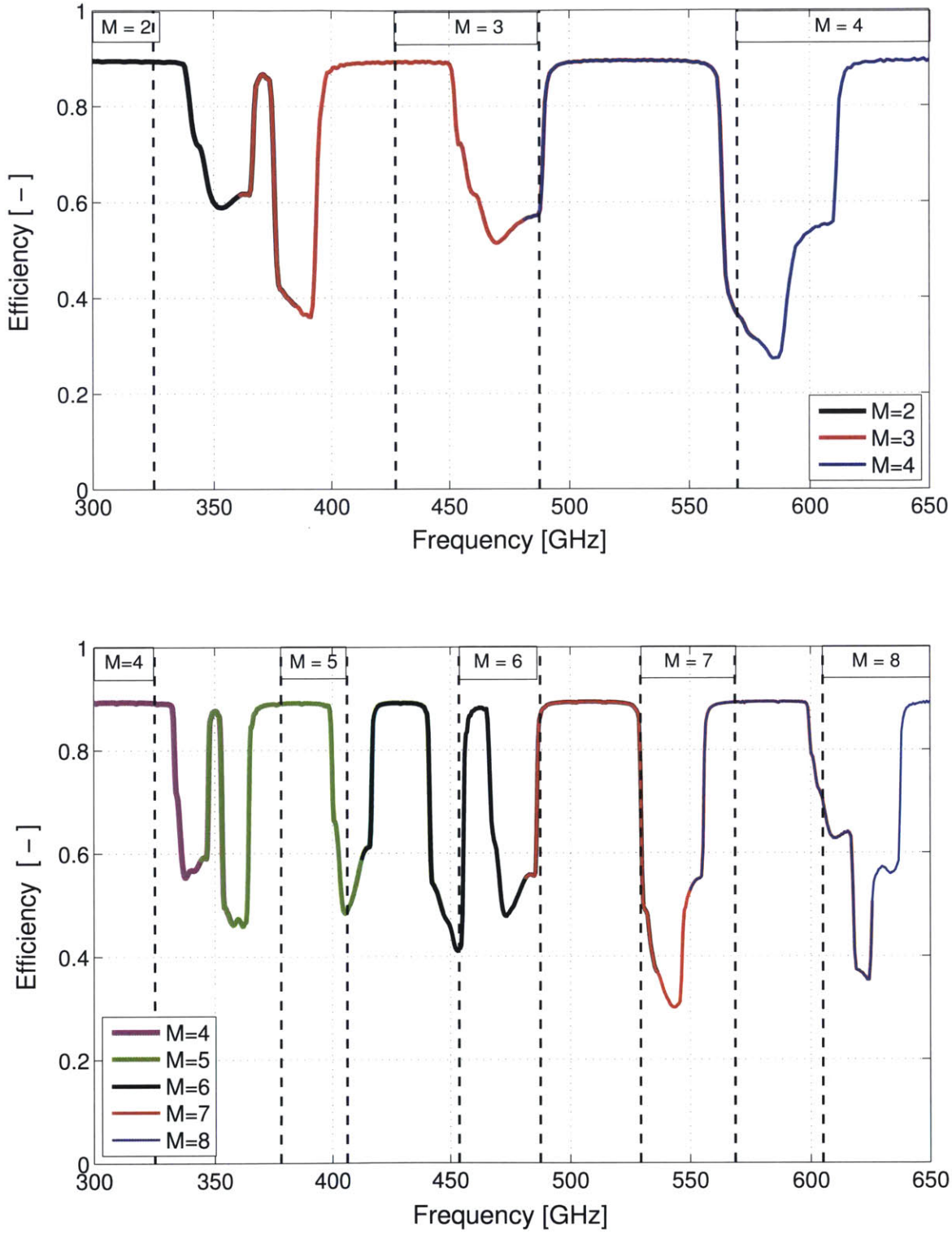

Figure 4.14: Coupling efficiency of the R260 and R520 designs. Frequency overlap in different orders was realized by extending the receivers' coverage over the entire focal plane. The low-efficiency gaps are expected by analogy with the behavior of antenna phased arrays.

$\sim 90\%$. The RMS phase error between the three stigmatic points is less than 0.005 radians for both designs and a fourth stigmatic point was observed beyond the angular range in use.

4.5 Higher-resolution 4-stigmatic-point solution

It is the purpose of this section to show how to use this additional stigmatic point as a degree of freedom to increase the number of spectrometer channels and resolving power. Here, two designs are described with $\mathcal{R} = 260$ in first order and four stigmatic points. The first design is the result of an unconstrained optimization and is described in [132]; it is reported in the remainder of this section with minor edits made to improve clarity. The second design constrains the maximum frequency to be associated with a specific point on the focal plane that ensures full coverage of the spectrum being analyzed.

4.5.1 Problem formulation

Following the same steps as in Sec. 4.4, "the formulation of the mixed integer non-linear problem is as follows:

$$\begin{aligned}
\max \mathcal{R}_{max}(M,\eta) &= M/\eta \cdot R/\lambda_{avg} && (4.22)\\
\text{subject to} \quad H_e(M,\eta) &\leq R && (4.23)\\
H_r(M,\eta) &\leq \pi R && (4.24)\\
\mathcal{R}_{max}(M,\eta) &> 200 && (4.25)\\
\eta &> 0 && (4.26)\\
M &\geq 1, \quad M \text{ integer} && (4.27)
\end{aligned}$$

Equation (4.23) imposes that the width of the emitter array, H_e, be less than or equal to the radius so that there is no aberration; Eq. (4.24) lets the receiver array be as large as the focal plane to maximize its utilization by spreading the stigmatic points over a larger space; and Eq. (4.25) sets a minimum value for the required maximum resolving power, $\mathcal{R}_{max}$, thereby eliminating solutions in which we are not interested. Finally, we note that, to enlarge the

tradespace, the constraint of equal emitter and receiver pitch, used in the designs previously described, was removed. The entire problem was solved with a Branch and Bound algorithm using the Interior Point OPTimizer (IPOPT) and Coin-or Branch and Cut (CBC) solvers.

Table 4.5 shows the requirements on spectrometer size and spectral range used for this problem. The minimum and maximum frequencies are no longer associated with any stigmatic point and they fall within the spectral range defined in Table 2.2. The average frequency was computed as their geometric mean.

The objective spaces as a function of M and η are shown in Fig. 4.15. On the left (Fig. 4.15a), it is possible to visualize the feasible objective space of the optimization problem described above for $\mathcal{R}_{max}$ along with the active constraint, Eq. (4.24) (blue area). The feasible solution of Eq. (4.22) populate that part of the contour plot above the blue area, whereas the optimal solutions lie at the intersection of the active constraint with the largest $\mathcal{R}_{max} \sim 275$, one for each value of M. We decided to investigate the first-order case as an example of simple and robust system. Higher-resolution instruments will certainly require higher-order

Table 4.5: Requirements on spectrometer size and spectral range (Adapted from [132])

Parameter	**Symbol**	**Unit**	**Value**
Multimode region radius	R	cm	1.25
Minimum frequency	f_{min}	GHz	430.0
Maximum frequency	f_{max}	GHz	650.0
Average frequency	f_{avg}	GHz	528.7

Table 4.6: Optimal solution of Equation (4.22) for $M = 1$ (Adapted from [132])

Variable	**Symbol**	**Unit**	**Value**
Spectrometer order	M	-	1
Relative emitter diameter	η	-	0.2916
Maximum resolving power	$\mathcal{R}_{max}$	-	275
Emitter array width	H_e	cm	1.2452
Receiver array width	H_r	cm	3.5674
Emitter pitch	p	cm	0.0048
Receiver pitch	s	cm	0.0167
Number of emitters	N_e	-	257
Number of receivers	N_r	-	149
Resolving power	$\mathcal{R}$	-	**257**

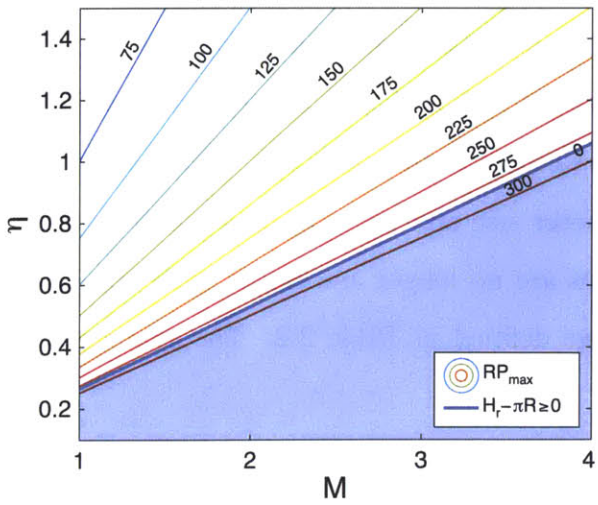

(a) The contour plot depicts all the feasible values of $\mathcal{R}_{max}$ associated with different values of M and η. For $M = 1$ and $\eta = 0.2916$, the optimal solution is $\mathcal{R}_{max} = 275$.

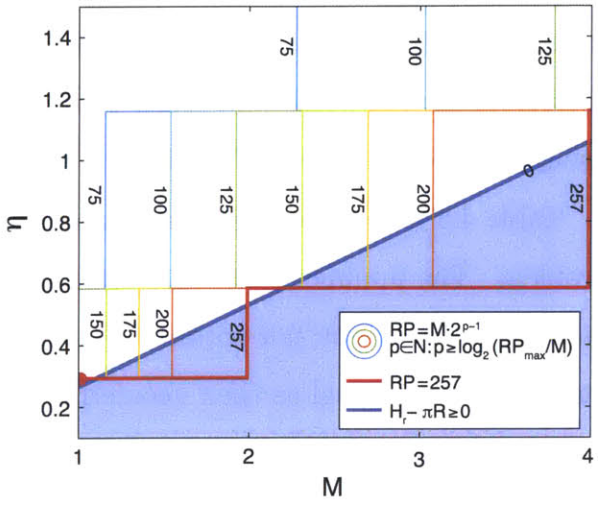

(b) The contour plot represents the feasible values of $\mathcal{R}$ for all orders given as powers of 2. The optimal solution for $M = 1$ and $\eta = 0.2916$ is associated with a resolving power $\mathcal{R} = 257$.

Figure 4.15: Objective spaces of Problem (4.22). The blue area represents the infeasible region corresponding to the active constraint in Eq. (4.24). Both plots show that, for each order M, several feasible solutions exist for different values of η. Adapted from [132].

operations. Table 4.6 shows the values of the design variables associated with this particular optimal solution as well as the values of Eqs. (4.23)-(4.27), which satisfy these constraints.

After solving this problem, it was possible to compute the number of emitters, $N_e = \mathcal{R}_{max}/M$, and round it down to a power of 2. The plot in Fig. 4.15b shows the values of $\mathcal{R}$ (red line) and the values of M and η that would make such realizations possible. In particular, for a first-order design ($M = 1$), the optimal solution corresponds to a resolving power $\mathcal{R} = 257$ with a relative emitter diameter $\eta = 0.2916$.

The second step toward determining the optimal solution in terms of the above-mentioned design variables consists in minimizing the overall RMS phase error, φ_{RMS}, through Eq. (4.20), a figure of merit representing the area subtended by φ_{RMS} on the focal plane. When setting Eq. (4.20) equal to zero, its analytical expression is a fourth-order function of the focal plane angle, β, which implies that at most four stigmatic points can be obtained. By solving the minimization problem present by Eq. (4.20) over the entire focal plane, i.e., $0 \leq \beta \leq \pi$, one could in principle find these four solutions, provided they are not degenerate." [132]

4.5.2 Optimization results

"The solution to the minimization problem defined in Eq. (4.20) was found with a quasi-Newton algorithm [133] and can be seen in Fig. 4.16. The emitters' positions are indicated in red and present several characteristics similar to those found and discussed in Sec. 4.4. First, they do not lie on the grating circle but on a curve that is tilted leftwards and intersects the grating circle at the central emitter before ending up inside the multimode region. In the case presented here, this is caused by the absence of constraints on all stigmatic points. The imposition of zero RMS phase error on a third stigmatic point (the blaze point) also caused a similar tilting effect [127], unless the emitters could be constrained to lie within a small distance (e.g., $\lambda_1/8$) from the $2R$ circle, as shown in Sec. 4.3 and [61].

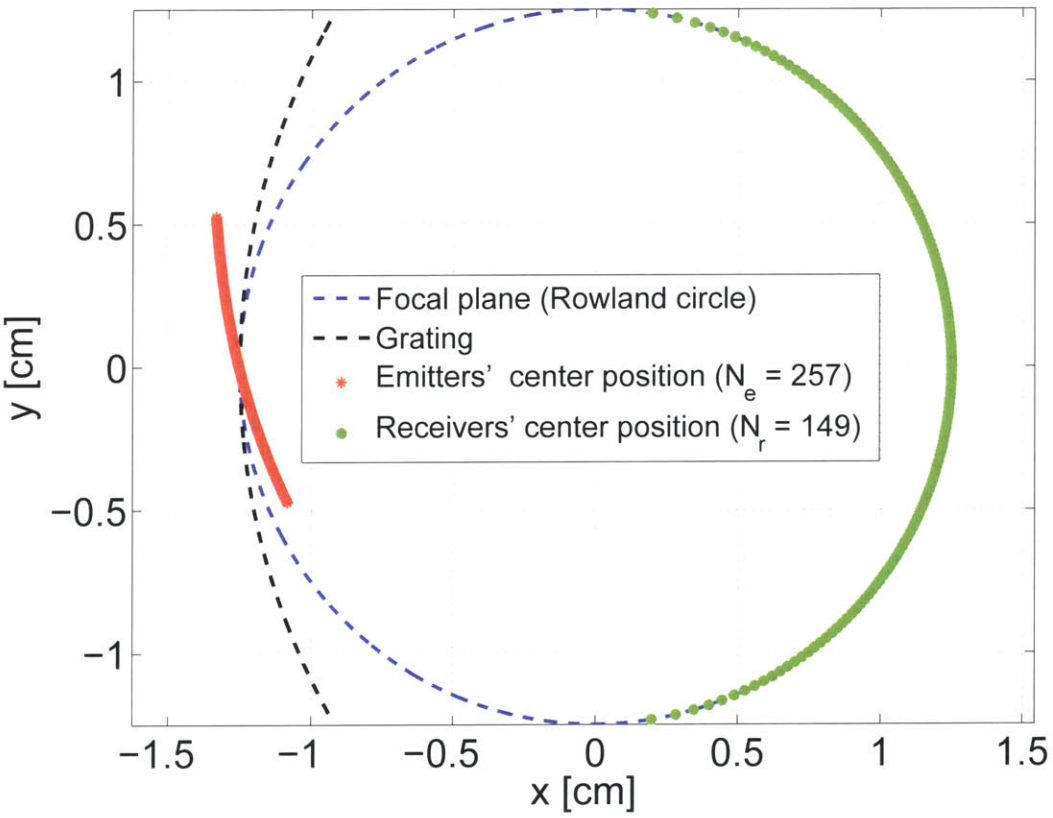

Figure 4.16: Optimized multimode region design with a resolving power $\mathcal{R} = 257$ and order $M = 1$. Adapted from [132].

The RMS phase error is shown in Fig. 4.17. Its values remain below 0.1 radians over an angular range spanning from approximately 16° to 176°. This phase error does not lead to a significant defocus of the light in the spectrometer [134] and represents a $\sim$ 30% improvement in the focal plane utilization over the previous designs [61, 127]. Four stigmatic points are visible, but they are no longer associated with a predefined frequency, given the absence of constraints on them. In Fig. 4.17 it can be seen to what frequencies they correspond in this design. The nominal spectral range indicated in Table 4.5 is only partially covered down to $\sim$ 510 GHz at 0°, while above 130° frequencies higher than 650 GHz show up, where the dispersion on the superconducting niobium's reactance is no longer negligible. A slightly larger multimode region could be employed to reduce these tensions." [132]

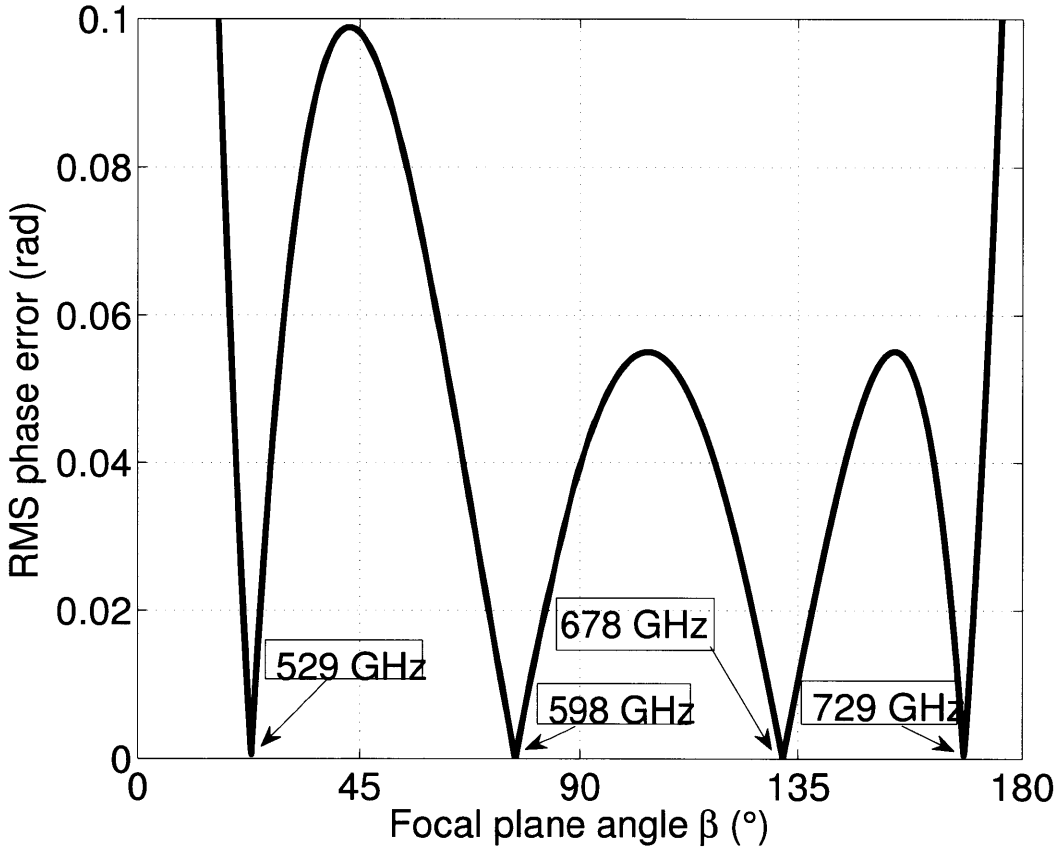

Figure 4.17: RMS phase error distribution on the focal plane. The worst peak value is 0.1 radians at almost 45° and four stigmatic points can be seen over a 160° angular range. Adapted from [132].

4.5.3 Power coupling efficiency

"The power coupling efficiency in the new design configuration was computed with the model described in [61, Sec. 4]. The ratio of the power emitted by the feed horns to the power received by the antennas is approximately equal to unity. This high efficiency is the result of the absence of any higher-order diffraction peaks in the multimode region due to the relative emitter diameter, η, being smaller than 1/2 [135].

The detailed coupling efficiency of the receiver feeds was not treated. For simplicity, the individual feed structures were mathematically modeled as if the focal surface were subdivided into apertures of equal size. The current configuration outperforms all those in first order in terms of efficiency, while simultaneously providing the desired resolving power." [132]

4.5.4 Summary of findings

"This section discussed a particular design achieved without constraining the RMS phase error to vanish at preselected stigmatic points on the focal plane. This led to a configuration with four stigmatic points on the focal plane, a feature which can be used to increase the number of spectrometer channels as the phase error is reduced over a larger angular and spectral bandwidth. This design achieves a maximum RMS phase error equal to 0.1 radians, near-unity coupling, and a resolution of 257 in first order. Future work will be aimed at employing this design methodology to generate higher-resolution ($\mathcal{R} > 500$) configurations." [132]

4.5.5 Revised higher-resolution 4-stigmatic-point solution

To avoid losing track of the wavelengths on the focal plane, the same minimization problem described in Sec. 4.5.1 was solved by: 1) increasing the spectrometer radius by a factor of 2 (the maximum allowed, given the chip size constraints) to allow the light reflected at large angles to be captured on the focal plane and 2) by associating the first stigmatic point with a frequency slightly higher than the minimum frequency, $f_1 = 450$ GHz, at an angle $\beta_1 < 40°$. This ensures an approximately even spectral distribution over the focal plane. The

preselection of the first stigmatic point is accomplished through the following mathematical constraint, which was added to Eq. (4.20) when minimizing the overall RMS phase error:

$$\varphi_{i1}(x_i, y_i, R_i^e, \beta_1) = 0, \quad i = 1, ..., N_e \tag{4.28}$$

The choice of $\beta_1 = 40°$ with an associated frequency of approximately 460 GHz results in a geometry similar to the one illustrated in the previous section (which therefore will not be shown again) and in an improvement of the RMS phase error and focal plane utilization as can be seen in Fig. 4.18. The entire spectral range is now recovered over 100°, which is equivalent to a focal plane utilization greater than 55%.

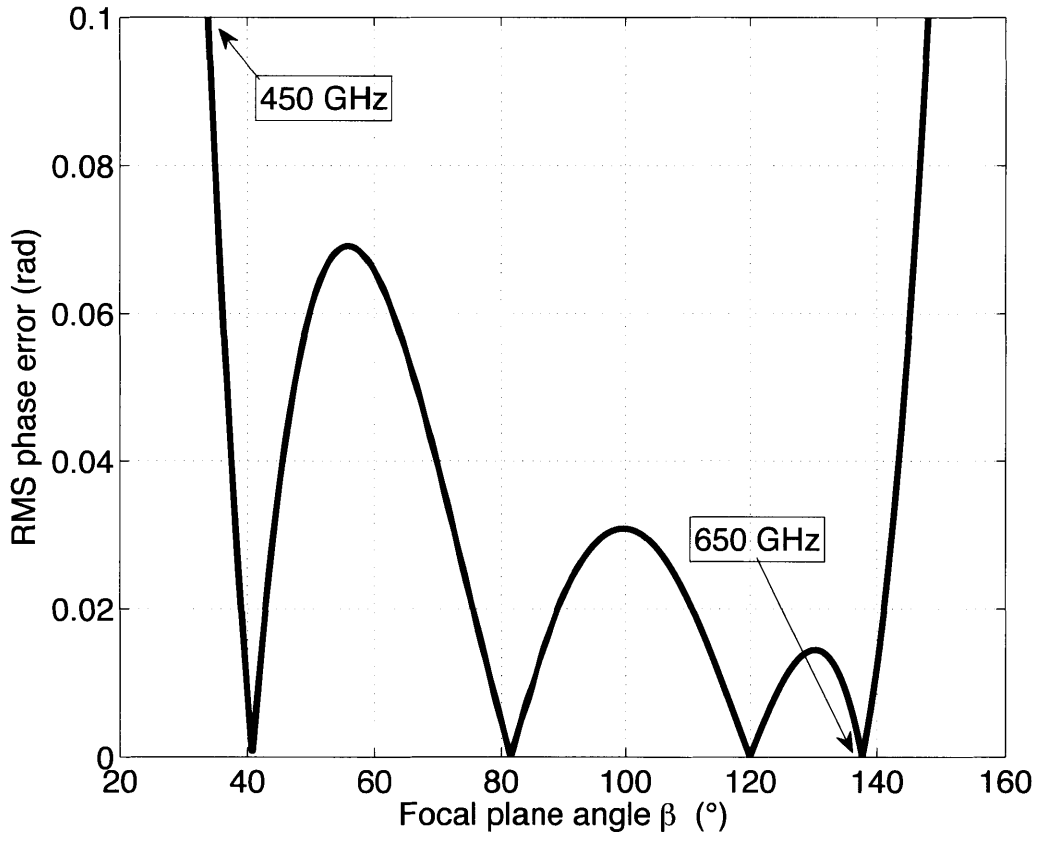

Figure 4.18: RMS phase error. Four stigmatic points can be seen over a 100° angular range and the frequencies of interest are recovered with an RMS phase error less than 0.1 rad over more than 55% of the focal plane.

Chapter 5

μ-Spec detectors: modeling of superconductors' response

Question 3: What are the propagation properties of the microstrip transmission lines made of superconductors such as molybdenum nitride and niobium? These parameters are needed for the design of the detectors and read-out system. Can the determination and accuracy of these parameters be improved, and how?

5.1 Microwave kinetic inductance detectors

The type of detectors under investigation for μ-Spec are microwave kinetic inductance detectors (MKIDs). MKIDs measure the change in kinetic inductance caused by the absorption of photons in a thin strip of superconducting material. Kinetic inductance is the manifestation of the inertial mass of mobile charge carriers in alternating electric fields as an equivalent series inductance. Kinetic inductance is observed in high carrier mobility conductors such as superconductors and at very high frequencies. The variation in kinetic inductance can be measured via the change in resonant frequency of a microwave resonator, in which the inductance is combined with a capacitor [136].

Figure 5.1a shows a lumped-element representation of an MKID. The incident far-IR/sub-millimeter radiation with energy $E = h\nu > 2\Delta$ (with h Planck's constant, ν the radiation

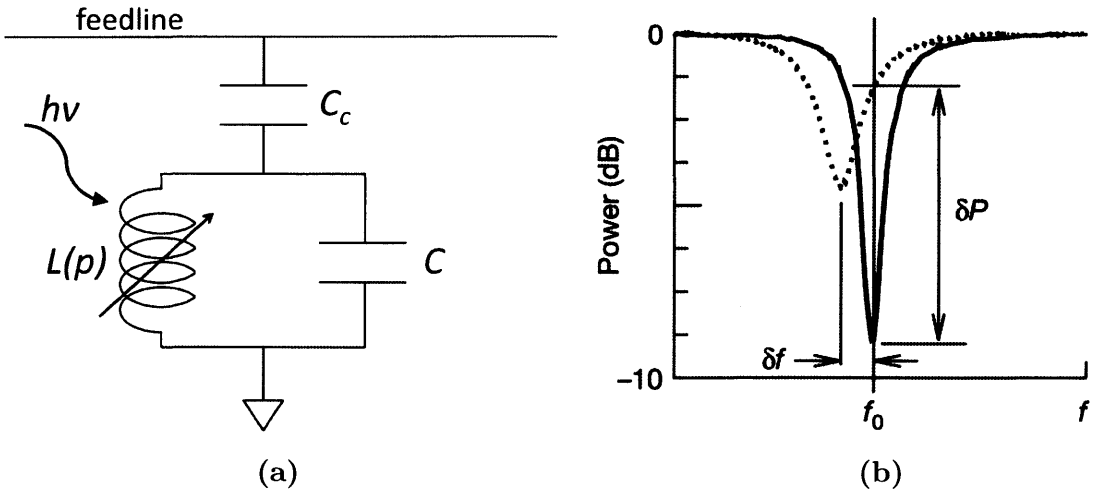

Figure 5.1: **(a)** A lumped-element circuit representation of a MKID. The incident radiation ($h\nu$) is absorbed through a superconducting film deposited over a dielectric and breaks Cooper pairs. The increase in quasiparticle density modifies the surface impedance, represented as a variable inductor, $L(p)$. In parallel with a capacitor, C, the inductor forms a microwave resonator coupled to a feedline through a coupling capacitor, C_c. **(b)** The increase in quasiparticle density moves the resonance to lower frequencies and changes the amplitude and phase of the signal. These variations can then be read out and analyzed. Adapted from [137].

frequency, and Δ the superconducting gap energy), is absorbed by a superconducting microstrip line cooled to temperatures well below the superconductor's critical temperature, T_c. The impinging radiation breaks Cooper pairs and creates a number of quasiparticle excitations equal to $\eta h\nu/\Delta$, where the efficiency η accounts for the energy that ends up as vibrations in the lattice called phonons. The increase in quasiparticle density changes the surface impedance, represented as a variable inductor, $L(p)$, dominated by the kinetic inductance. In parallel with a capacitor, C, it forms a microwave resonator coupled to a feedline through a coupling capacitor, C_c, for read-out. The working principle of a MKID is illustrated in Fig. 5.1b, which shows that at resonance the LC circuit exhibits a dip in its transmission. The quasiparticles generated by the photon shift the resonance to lower frequencies while simultaneously making the dip shallower and broader and changing the phase of the signal. These effects due to variations in kinetic inductance can thus be read out via frequency-domain multiplexing [137]. In practice, the capacitor and inductor are respectively realized through etching of a parallel-plate and meander structure on a thin superconducting film laid on top of a dielectric substrate.

For μ-Spec, the use of single-crystal silicon as the microstrip substrate is highly recommended to reduce dielectric losses and the noise associated with two-level systems (TLSs), which commonly present in amorphous (non-crystalline) materials but also at the interfaces (surfaces or defect sites) of crystalline materials. A TLS is a localized low-energy excitation, in which an electron or an ion tunnels between two spatial quantum states. This phenomenon is caused by the presence of defects in the dielectric's crystal structure or polar impurities such as OH^-. TLSs are charged in nature and have a dipole moment that can interact with electromagnetic fields, including those generated by low-temperature systems such as MKIDs, superconducting qubits, and many other electronic devices [138]. This interaction acts as a source of noise as it produces phase fluctuations that negatively affect the performance of such systems by increasing their losses [139].

As mentioned in Chapter 2, the main difficulty in producing the μ-Spec modules is to generate sufficiently low loss in the microstrip lines over the desired frequency band and to demonstrate that the MKIDs operate at the required NEP. The loss in terms of total end-to-end coupling efficiency for the system will likely have to be less than 1 dB, but this is only an estimate and will need further refinements as the instrument design improves and becomes more detailed.[1] To understand what type of superconducting materials is capable of enabling this kind of high-sensitivity detectors required for ultra-low-noise far-IR instrumentation such as μ-Spec, an analysis of their response over the spectral range under investigation is necessary.

"The resonator's transmission amplitude and phase can be characterized with a vector network analyzer (VNA). Ideally, the VNA calibration reference plane or "test port" would be directly connected to the device under test (DUT); however, a cryogenic setting typically necessitates the use of additional transmission line structures to realize a thermal break between 300 K and the cold stage (e.g., 0.3 K in this work, see Fig. 5.2). Other ancillary microwave components – directional couplers, circulators, isolators, amplifiers, attenuators, and associated interconnecting cables – may be required to appropriately prepare, excite, read

[1]For instance, one cannot use the entire loss budget in the microstrip, as there would be reflection mismatches, optical coupling losses, and detection absorption efficiencies. As explained in Chapter 3, for the microstrip one should estimate a maximum path length and derive an allowable loss per unit length or, equivalently, the allowed absorption index in the medium.

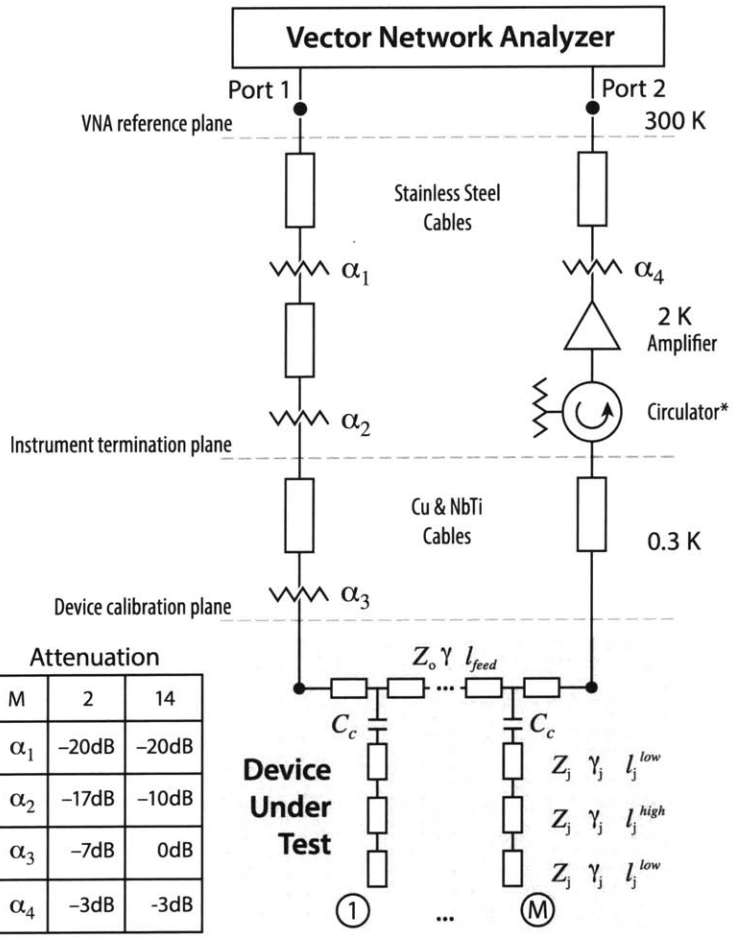

Figure 5.2: Schematic of the experimental apparatus and devices under test. The resonators are coupled to a CPW feedline through coupling capacitors and their response is observed through a VNA connected to the DUT. Summary of the attenuators employed in each measurement can be found in the table. The circulator indicated by a * was only present for the 2-resonator test configuration. Adapted from [72].

Attenuation

M	2	14
α_1	-20dB	-20dB
α_2	-17dB	-10dB
α_3	-7dB	0dB
α_4	-3dB	-3dB

out, and bias the device of interest. The phase velocities and dimensions of such components change in cooling from room temperature and therefore affect the observed response at the device calibration plane. These intervening components between the instrument and the device calibration plane influence the complex gain and need to be appropriately accounted for in the interpretation of the measured response.

Ideally, a scheme is desired that places the reference plane of the measurement at the DUT which is identical to that used during calibration. A flexible and *in-situ* calibration procedure is desired for multiple resonators over a frequency range wide compared to the resonator line width and inter-resonator spacing." [72] This approach provides answers to Question 3 presented at the beginning of this chapter and a detailed explanation thereof can be found in [72], which will be reported in the remainder of this chapter with minor edits to improve clarity.

5.2 Literature review of resonator response modeling techniques

"In the context of MKID physics [140], as well as quantum computing [141] and the determination of low-temperature materials properties [142, 143], precision measurements of the quality factors, Q, of superconducting resonators become important. At sub-kelvin temperatures the quality factors are generally determined by measuring and fitting the transmission data over the relatively narrow bandwidth defined by the response of a single resonator [144]. In this setting, the fidelity of the observed response can be limited by the intervening instrumentation between the device under test and the measurement reference plane.

In physically modeling the electrical response of these circuits, a lumped-element approximation can be applied when the electrical size of the elements and their interconnections is small compared to a wavelength. This consideration ensures that the structures are not self-resonant. More generally, a transmission line approximation enables one to treat distributed elements with one dimension greater than a fraction of a wavelength in scale. However, when the electromagnetic fields and phases within the circuit elements are uniform and uncoupled, the lumped and distributed approaches are identical [145]. It is not uncommon for "lumped elements" to have a significant internal phase delay in practical microwave devices. For "capacitive" elements synthesized from electrically small transmission line lengths this effect can be small, but "inductive" elements inherently possess a finite internal phase delay by design. The utility of this iconic lumped picture primarily resides in its conceptual simplicity as opposed to the end accuracy and fidelity of the physical representation.

This being said, analytical methods based on lumped-element approximations are commonly used to analyze scattering parameters of resonators and compute their Q factors [146–151]. These expressions are derived from LCR circuit representations and are based on the assertion of weak coupling between resonators to simplify the analysis. These formulations employ simplified functional forms for the transmission, S_{21}, and are suited for approximating the response near resonance for high-quality-factor lumped circuits.

A detailed review of fitting methods is offered in [144], where several methods are pre-

sented for fitting the S_{21} magnitude to different models which neglect the measured phase. These methods do not deal with the alterations that the data incur in the real measurement scenario, such as crosstalk between cables and/or coupling structures, the resonator coupling ports not being coincident with the reference plane of the measurements, and the presence of and coupling to nearby resonators. Many of the methods described, which attempt to correct for these effects on S_{21}, remain sensitive to the details of fitting in the complex plane [144, 152, 153]. This work strives to address these issues by using a transmission line representation to simultaneously analyze multiple coupled resonators and present a calibration methodology to remove non-ideal instrument artifacts." [72]

5.3 Analysis and calibration of superconducting resonators

5.3.1 VNA transmission data calibration

"For a single resonator or multiple well-separated resonators, the response can be well reproduced by a Lorentzian line shape. In the presence of multiple resonances, their mutual interaction as well as the interaction with the continuum can result in a Fano spectral response [154–158]. This effect can also be experimentally observed as an interaction between the resonators with the relatively broad Fabry-Perot resonances resulting from standing waves in the system. Such reflections produce the dominant spectral variation in the observed instrument baseline and can be mitigated by minimizing the transmission line lengths and suitably terminating the reflections with matched attenuators and circulators at the instrument termination plane. In calibrating the spectra, an unbiased removal of these artifacts is desired.

As an example of the calibration process, we use the data from the CPW feedline coupled to the two molybdenum-nitride (Mo_2N) resonators. Figure 5.3a shows the real and imaginary components of the transmission, S_{21}, at the VNA reference plane as a function of frequency. It can be seen that the characteristic scale of the baseline variations is much larger than the

resonator response in frequency. To calibrate the VNA data *in-situ*, the following steps are performed:

1. fit of the complex baseline (Fig. 5.3c);

2. normalization of the transmission's real and imaginary parts (Fig. 5.3c-d);

3. correction for variations in gain and relocation of the reference plane at the DUT by ratioing out the complex baseline fit (Fig. 5.3e-f).

In general, the baseline can have an unpredictable shape as determined by the details of the reflections occurring throughout the instrument and its components. The complex baseline, $S_{21,bas}$, was modeled analytically and a Fourier series was found to be a convenient and physically motivated representation of its response:

$$S_{21,bas} = \sum_{j=1}^{n} A_j \cdot \exp\left(i d_j \omega\right). \tag{5.1}$$

In Eq. (5.1) A_j is a complex coefficient, d_j a time delay, and ω the angular frequency. In the case presented, $n = 4$ terms were found to be sufficient to adequately sample the baseline and appropriately constrain its properties. A fit to the 30 000 measured data points resulted in a reduced $\chi^2 = 0.9973$. Differences in experimental configuration or changes in the desired calibration spectral range may lead to alternative forms for Eq. (5.1).

The second step in data calibration consists of uniquely specifying the complex gain amplitude between the VNA reference plane and the device calibration plane so that the S_{21} real and imaginary components in Fig. 5.3a lie between ± 1. This normalization factor was found to be approximately 6.32 by forcing the transmission amplitude to be equal to unity far from the resonator response. The normalized measurements and modeled data are presented in the Smith chart in Fig. 5.3d.

Finally, the complex baseline, $S_{21,bas}$, was removed from the data through Eq. (5.1) to eliminate the influence of reflections and move the reference plane to the DUT. By looking at the topology of the instrument, the error matrices introduced by the connections between the reference plane and the device under test in the cryostat are in series. From the properties

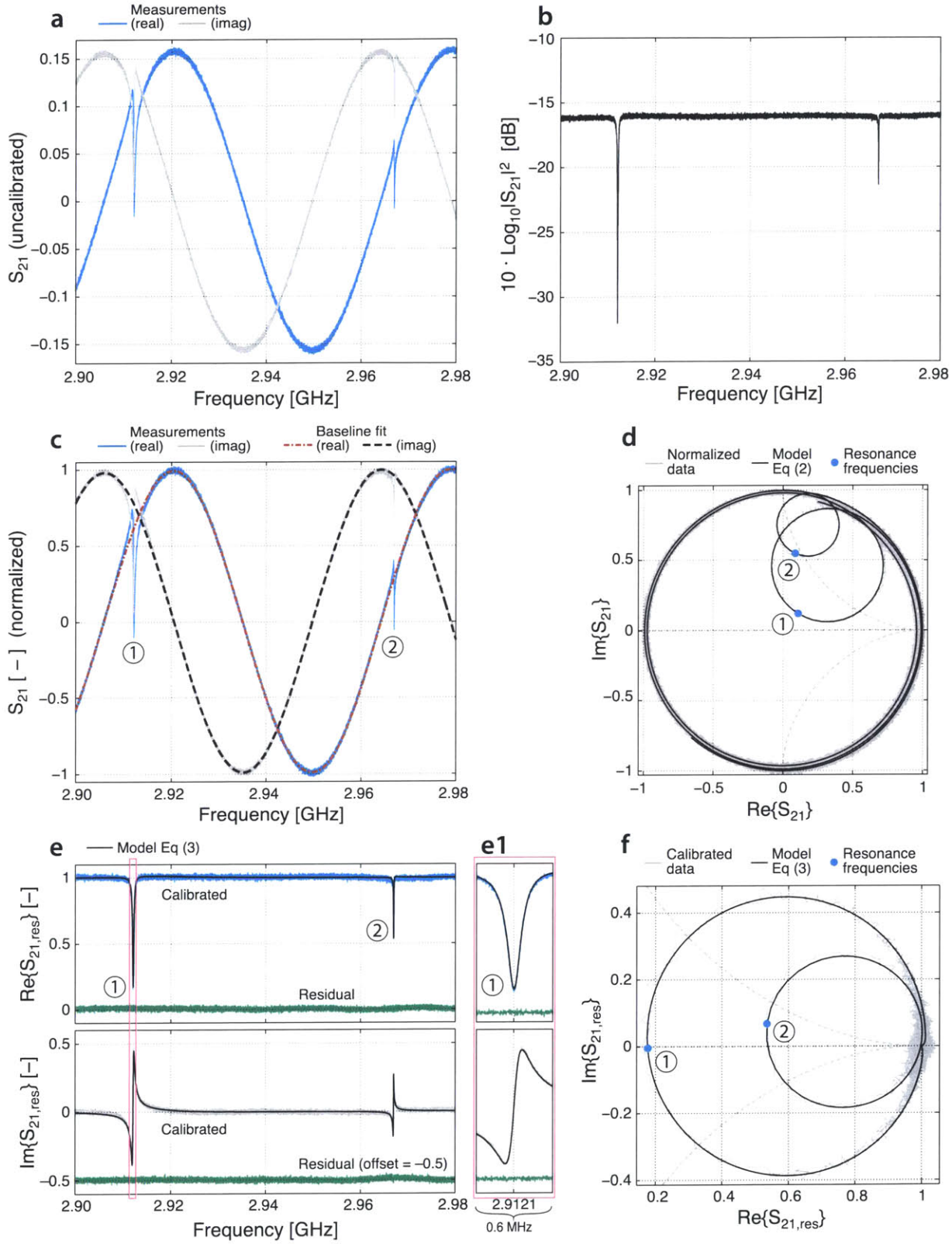

Figure 5.3: Measurement calibration overview. a) Complex S_{21} data for the DUT as observed at the VNA reference plane. b) From the perspective of the DUT, the magnitude of the response is uncalibrated due to the amplifiers, attenuators, and other microwave elements in the system. c) The measured transmission spectrum is normalized by forcing its amplitude to be equal to unity far from the resonator responses. The baseline fit is displayed for ease of comparison. d) The normalized transmission data are shown on a Smith chart. The baseline variation with frequency can be seen as a deviation in the S_{21} from unity far from the resonator response. e) After removing the complex baseline and specifying the device-calibration-plane phase, the calibrated data are used to fit an analytical model, and the residuals are shown. f) The Smith chart shows the two resonance loops going through (1,0) after calibration. Adapted from [72].

of signal flow graphs [65, 159], the uncalibrated transmission coefficient, S_{21}, at the VNA reference plane is therefore the product of the following scattering matrix elements:

$$S_{21} = S_{21,bas} \cdot S_{21,res}, \tag{5.2}$$

where $S_{21,res}$ refers to the desired calibrated response of the resonator device under test." [72]

5.3.2 Phenomenological resonator model

"With the baseline correction applied, the calibrated data (Figure 5.3e) were modeled in order to extract the characteristic resonant frequencies and line widths. The feedline and resonator model for the packaged device can be represented as a realizable causal filter as follows:

$$S_{21,res} = 1 + \sum_{j=1}^{M} \frac{a_{0,j} + a_{1,j}x_j + a_{2,j}x_j^2 + \ldots}{1 + ix_j + b_{2,j}x_j^2 + \ldots}, \tag{5.3}$$

where, for each $j = 1, ..., M$ (M being the total number of resonators), $x_j = Q_{tot,j} \cdot (\omega/\omega_{o,j} - \omega_{o,j}/\omega)$ and $Q_{tot,j}$ is the total loaded quality factor defined as $Q_{tot,j} = \omega_{o,j}/\Gamma_j$. For each resonator, therefore, the fitting parameters are: the $a_{k,j}$ and $b_{k,j}$ complex coefficients ($k = 0, 1, 2, ...$, $j = 1, ..., M$), the resonance frequency $\omega_{o,j}$, and the full width at half power Γ_j. Here, we use $k = 2$ in specifying the order of the polynomial.

The functional form of Eq. (5.3) exhibits several features. First, its second-order terms in both the numerators and denominators allow for reproduction of the resonator responses, thereby enabling the representation of a physically realizable, distributed circuit network [160]. Second, its causality is assured by the degree of the numerator not being greater than that of the denominator, which allows the functional form to satisfy the Kramers-Kronig relations [161]. Far removed from the resonators, $S_{21,res} \rightarrow 1 + i\,0$ and the transmission represents an ideal thru line. It was verified that our second-order model approached this limit without additional terms to avoid increasing the number of parameters and the computational effort. Finally, this functional form enables one to simultaneously fit any number of resonators while formally taking into account their physical interactions.

Rewriting x_j in the equivalent form, $x_j = Q_{tot} \cdot (\omega_{o,j}/\omega) \cdot (\omega/\omega_{o,j} + 1) \cdot (\omega/\omega_{o,j} - 1)$, reveals

a commonly employed approximation, $x_j \approx 2Q_{tot} \cdot (\omega/\omega_{o,j} - 1)$, near resonance. This form can be viewed as an asymptotic expansion in powers of $1/Q_{tot}$ which modifies the position of the resonant frequency in the complex plane [162]. When Eq. (5.3) is evaluated in this limit, the expressions reduce to the first-order lumped-circuit treatments described in the literature for a single resonator in transmission [146, 147, 163]. However, we find that to faithfully reproduce the interactions between resonators over a wide spectral bandwidth the full functional form presented here is required." [72]

Analysis of the 2-resonator dataset

"Equation (5.3) was used to fit the calibrated data by means of a least-squares curve fitting routine based on a trust-region reflective Newton method [164, 165]. Constraints were given in the form of global lower and upper bounds for each $\Gamma > 0$ and ω_o. The starting guess for each Γ was chosen close to the actual value, which can be readily determined by estimating each resonator's spectral width. The initial guess for the resonance frequency, on the other hand, corresponds to the frequency values where the observed S_{21} has minima. The results are shown in Fig. 5.3e (black line) for both components. The residuals on the real and imaginary parts are comparable to the normally distributed noise level in the measured data with a reduced $\chi^2 = 0.9987$ and a standard deviation of $\sigma = 0.0155$. A Smith chart is provided in Fig. 5.3f, which shows that the two circles touch each other in $(1, 0)$ with a relative rotation of about 7° caused by the phase delay in the feedline length between the two resonators. Because of the noise in the measured data and the residual systematic errors in the baseline fit, the data around $(1, 0)$ converge to this point within a radius of 0.04. The estimated values for the fitting parameters of each resonator are summarized in Table 5.1.

Table 5.1: Parameter summary for the 2-resonator analytical model (Adapted from [72])

j [−]	$a_{0,j}$ [−]	$a_{1,j}$ [−]	$a_{2,j}$ [−]	$b_{2,j}$ [−]
1	$-0.7345 + i\,0.1029$	$-0.0440 + i\,0.0879$	$-0.0008 - i\,0.0009$	$-0.0120 - i\,0.0048$
2	$-0.5496 - i\,0.0463$	$-0.4737 + i\,2.1868$	$-2.1104 - i\,2.4638$	$30.0366 - i\,13.2458$

j [−]	$\omega_{o,j}/(2\pi)$ [GHz]	$\Gamma_j/(2\pi)$ [kHz]
1	$2.9121\ldots \pm 7 \times 10^{-9}$	139.02 ± 0.01
2	$2.9670\ldots \pm 60 \times 10^{-9}$	50 ± 2

The internal and coupling Q factors were calculated using the following equations [166, 167]:

$$Q_{i,j} = \frac{Q_{tot,j}}{1 - D_j}, \tag{5.4}$$

$$Q_{c,j} = \frac{Q_{tot,j}}{D_j}, \tag{5.5}$$

where D_j represents the diameter of the circle associated with each resonator (Fig. 5.3f). The Q-factor values are shown in Table 5.2." [72]

Table 5.2: Q factors for the 2-resonator analytical model (Adapted from [72])

j [−]	$Q_{tot,j}$ [−]	$Q_{i,j}$ [−]	$Q_{c,j}$ [−]
1	$20,948 \pm 1$	$107,583 \pm 2$	$26,013 \pm 1$
2	$59,400 \pm 180$	$109,500 \pm 330$	$129,800 \pm 390$

Analysis of the 14-resonator dataset

"A 14-resonator CPW dataset was also studied (see Figs. 5.4a-b). In this example, the resonators span a spectral range of about 45 MHz with two pairs of resonators strongly interacting with each other, namely, resonators 5-6 and 9-10. The analysis of this dataset was challenging because, for high values of Q_{tot}, the denominator of Eq. (5.3) approaches an

indeterminate form of the type $[0 \cdot \infty]$, which can result in numerical instability. In addition, the parameters of interest span 6 orders of magnitude leading to an ill-conditioned Hessian matrix for the system.

Equation (5.3) was used to fit the calibrated data by means of a least-squares curve fitting routine based on a trust-region reflective Newton method with a diagonal preconditioning of the conjugate gradient. To help the algorithm with convergence, all Γ_j and $\omega_{o,j}$ $(j = 1, \ldots, 14)$ were provided with lower and upper bounds, namely, $0 < \Gamma_j \leq \Gamma_{max}$ and $\omega_{min} \leq \omega_{o,j} \leq \omega_{o,max}$ for $j = 1, \ldots, 14$. Here, $\Gamma_{max} = 10$ MHz, well above the largest Γ_1 (≈ 1.6 MHz). The minimum angular frequency is $\omega_{min} = 2.5040$ GHz and the maximum resonance frequency, $\omega_{o,max}$, was set not to exceed a distance of $10 \times \Gamma_{14}$ from the last resonance frequency. For the highest-Q resonators (i.e., the highest frequencies in the recorded transmission spectra) the model is more sensitive to changes in $\omega_{o,j}$. This choice for the bounds helped the algorithm in identifying solutions within the desired range of parameters and converged after < 300 iterations.

The model represented by Eq. (5.3) recovers the calibrated data within an accuracy of $< 1\%$ (Figs. 5.4c-d) with a reduced $\chi^2 = 0.9985$ and a standard deviation $\sigma = 0.0027$, thus proving to be a robust method to analyze numerous, strongly coupled resonators. In this dataset, the range of quality factors spans more than two orders of magnitude, e.g., $2,300 < Q_c < 630,000$. A particular challenge noted in this existing dataset was that the observed spectral range was suboptimal. From an experimental design perspective, the phase variation of the DUT and the baseline need to be appropriately sampled and to possess differing spectral signatures to enable independent reconstruction from the measured dataset. By using the modeled response as noiseless input to the fitting algorithm, it was found that the spectral range of this dataset should have been extended by 30% to minimize the calibration error with this algorithm. This increase in spectral range would enable the responses of the resonator wings and the baseline to be sufficiently decoupled to achieve an unbiased amplitude calibration." [72]

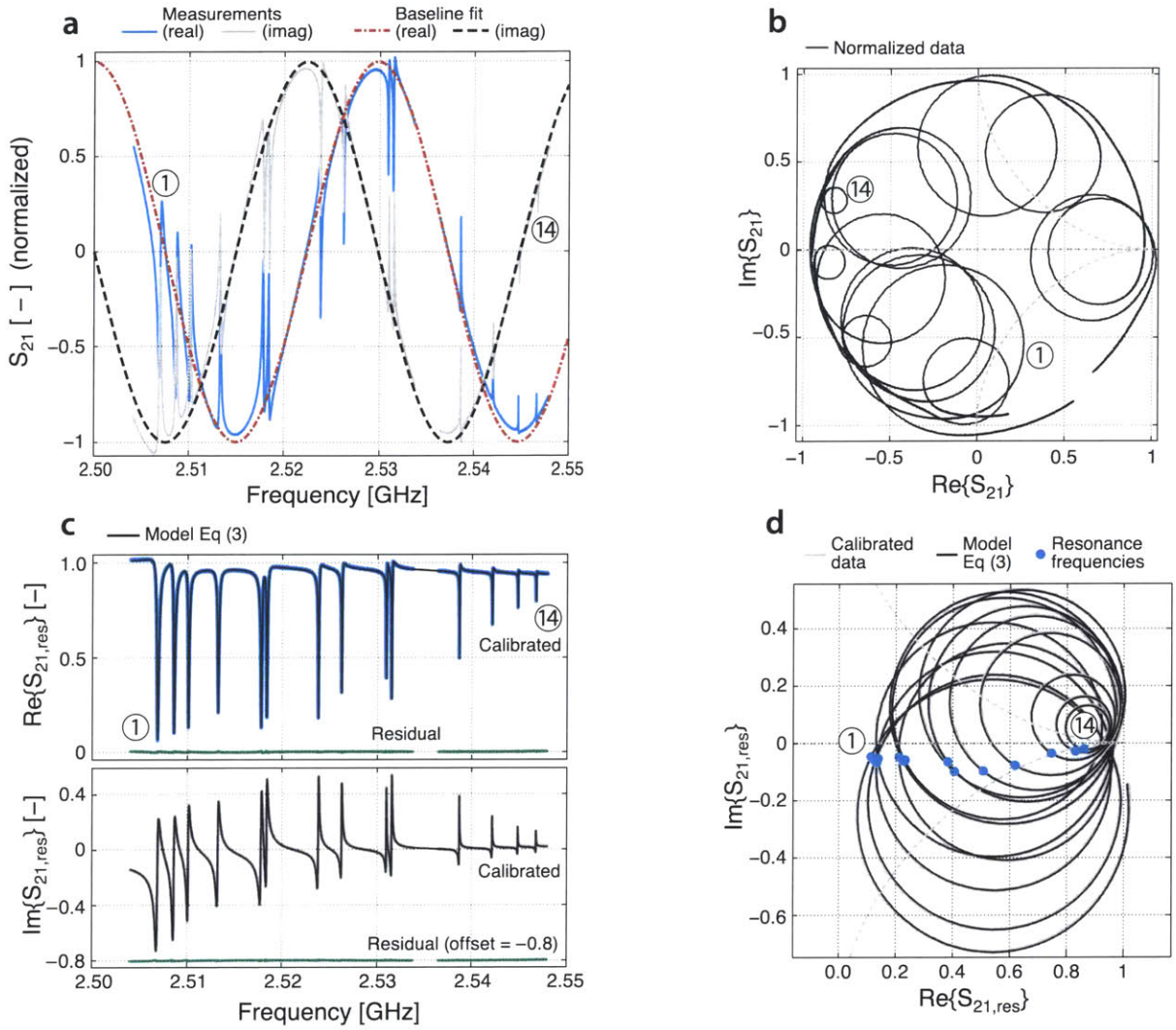

Figure 5.4: Results for the 14-resonator CPW dataset. a) Normalized transmission data and baseline fit. b) Smith chart representation of the normalized transmission data. c) Calibrated transmission data and analytical model. The achieved residuals are smaller than 1%. d) Smith chart showing the calibrated 14-resonator data wrapping around (1,0). Note: The 14-resonator CPW dataset was acquired in two discrete sections and a small gap in the measured transmission spectra is present at $\approx 2.535\,\mathrm{GHz}$. Adapted from [72].

5.3.3 ABCD-matrix model

"The phenomenological resonator model based on Eq. (5.3) and discussed in Sec. 5.3.2 is useful and sufficient if one needs to know the center frequencies and the resonators' Q factors. Clearly, there are many quasi-TEM structures such as microstrip, CPW, or other transmission line types which can lead to the observed response. Since the phenomenological resonator model is blind to the details of the realization, a distributed transmission line representation

needs to be employed in order to probe the internal structure of the circuit. Here, the impedance, propagation constant, and lengths are used to characterize the circuit response in an ABCD or chain-matrix formulation. In this process, specifically, the impedance and propagation constant are used as parameters to fit the transmission data.

Although coupling to higher-order modes (e.g., losses to radiation, surface waves, and parasitic coupling between elements) can influence the underlying network topology, in the formulation used here, we assume single-mode propagation and rely upon the specification of the circuit network. This process is related to "de-embedding" or the process of inferring the response of a device under test when electrical properties of the intervening structure (in this case, the feedline coupling structure) are known [168]. Elegant implementations of such concepts in the context of scalar millimeter-wave circuit metrology are described in [169,170].

To model the 2-resonator device response below the instrument termination plane (Fig. 5.2), 29 transmission line elements were used. For each line section, the physical lengths, l, were known to a micron accuracy from the photolithographic mask, while the characteristic impedances, Z_o, and the propagation constant, γ, were simulated with HFSS (High Frequency Structure Simulator). For simplicity, the two coupling capacitors were modeled as lumped elements and their capacitances also simulated with HFSS ($C_{c_1} \approx 53\,\mathrm{fF}$ and $C_{c_2} \approx 23\,\mathrm{fF}$). The detailed description of the ABCD-matrix model can be found in the Appendix at the end of this chapter.

Substituting the numerical values of each transmission line element into Eq. (5.14) and cascading through Eq. (5.13) yields the ABCD parameters of the entire transmission line circuit. These parameters were used in Eq. (5.12) to evaluate the modeled transmission response, S_{21}. A challenge of this method lies in the difficulty in fully specifying the elements of the system at cryogenic temperatures. To simplify the extent of the system to be characterized, the instrument calibration plane was chosen to approximate a matched termination as close as feasible to the packaged device under test.

In addition, as a cross-check of the baseline correction obtained by fitting, the elements leading to this instrumental response were computed with the ABCD-matrix model and agreed to within a 5% accuracy with the measured transmission line coaxial-cable lengths

given nominal literature values for the Teflon dielectric. Experimental investigation revealed that the superconducting NbTi thermal break cable was the limiting element in the uncorrected baseline response. In fitting, it was found that the characteristic impedance of this line was approximately $60\,\Omega$. This section of cable was subsequently inspected and a gap in the Teflon dielectric was noted to be consistent with these observations." [72]

Transmission line parameter extraction

"For the transmission line structures, the characteristic impedance, Z_o, and propagation constant, γ, are functions of the effective permittivity, $\varepsilon_{r,\text{eff}}$, and permeability, $\mu_{r,\text{eff}}$, in the medium. In particular, Z_o is a function of the transmission line geometry proportional to the relative wave impedance in the medium, $Z_n \equiv (\mu_{r,\text{eff}}/\varepsilon_{r,\text{eff}})^{1/2}$, and γ is defined such that

$$\gamma^2 \equiv -\left(\frac{\omega}{c}\right)^2 \cdot (\varepsilon_{r,\text{eff}} \cdot \mu_{r,\text{eff}}) = -\left(\frac{\omega}{c}\right)^2 \cdot n_{\text{eff}}^2, \tag{5.6}$$

where ω is the angular frequency, c the speed of light in vacuum, and n_{eff} the effective index in the medium. For microstrip, the effective permittivity and permeability are explicitly defined as

$$\varepsilon_{r,\text{eff}} \equiv \frac{C(\varepsilon_1, \varepsilon_2)}{C(\varepsilon_o, \varepsilon_o)}, \quad \mu_{r,\text{eff}} \equiv \frac{L(\mu_1, \mu_2)}{L(\mu_o, \mu_o)}, \tag{5.7}$$

where the capacitance, C, and the inductance, L, per unit length are measures of the electromagnetic energy stored in the transmission line [66,171]. To find the effective constitutive relations, these functions are evaluated in the presence and absence of the dielectric and superconducting media, respectively. Here, ε_2 refers to the monocrystalline silicon substrate, ε_1 to the superstrate dielectric, μ_1 to the centerline, μ_2 to the ground plane metallization, and ε_o and μ_o are the permittivity and permeability of free space (see Fig. 5.5). For other transmission line structures, analogous formulations of Eq. (5.7) can be defined for the constitutive parameters.

This parameterization results in $\varepsilon_{r,\text{eff}}$ and $\mu_{r,\text{eff}}$ becoming implicit functions of the line's materials properties and cross-sectional geometry. The imaginary component of $\mu_{r,\text{eff}}$ was taken as zero. An effective dielectric loss tangent $\approx 1.8 \times 10^{-5}$ was observed in fitting the

observed microstrip resonator spectra. This is consistent with the bound on the dielectric loss tangent, $< 5 \times 10^{-5}$, at 2.2 K for a similar (1.45-μm-thick) silicon sample used as a Nb microstrip ring resonator at 4.7 GHz. As discussed in [74], upon cooling to cryogenic temperatures, the bulk resistivity silicon ($\rho \geq 1\,\mathrm{k}\Omega - \mathrm{cm}$ for these samples) freezes out and the intrinsic loss mechanisms in silicon dominate at microwave frequencies. The achievable thicknesses and high uniformity (±0.013 μm) of the monocrystalline silicon wafers [172] employed in this investigation enable its use as an ultra-low-loss controlled-impedance microwave substrate. The observed loss in the circuit can have contributions from the bulk properties of the silicon layers, the bisbenzocyclobutene (BCB) wafer bonding agent, two-level systems in the silicon oxide layer, and conversion to surface and radiation modes. In addition, residual coupling to the electromagnetic environment could contribute to the observed loss, in particular for higher Q factors. Although a detailed breakdown of the contributions to the observed loss is possible by investigating the performance as a function of geometry and temperature, this was not attempted here. Thus, in ascribing the entire observed loss to the dielectric, the above-mentioned loss tangent represents a conservative upper bound to that of monocrystalline silicon.

In fitting, for each transmission line type (high or low) a global characteristic impedance and phase velocity were employed. The low-impedance lines have a width of 60 μm, whereas the high-impedance lines have a width of 18μm. Electromagnetic simulations were performed with HFSS for the CPW and microstrip configurations shown in Fig. 5.5." [72]

"To study the resonator circuit's response in detail, a fit of the S_{21} data depicted in Fig. 5.3c to Eq. (5.12) was performed. The fitting parameters were Z_o, n_{eff}, and C_c for each of the two resonators' transmission line sections. From Z_o, the medium's relative wave impedance, Z_n, can be determined as follows:

$$Z_n \equiv \left(\frac{\mu_{r,\mathrm{eff}}}{\varepsilon_{r,\mathrm{eff}}}\right)^{1/2} = \frac{Z_o}{Z_{o,\mathrm{HFSS}}} \tag{5.8}$$

for each of the transmission lines used in the resonator realization. Here, $Z_{o,\mathrm{HFSS}}$ represents the transmission line characteristic impedance simulated using HFSS with perfect E-field boundaries for conductors and the permittivity of free space for dielectrics.

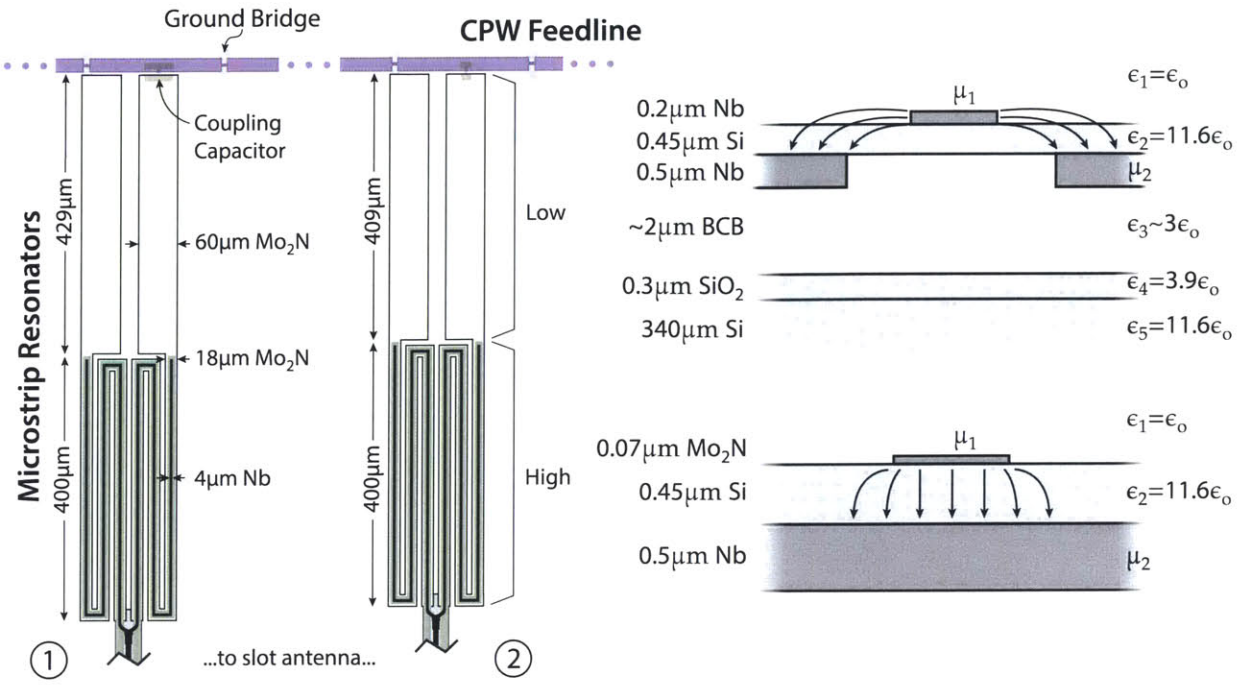

Figure 5.5: Left: Layout for the 2-resonator chip. The stepped-impedance resonators are coupled to a CPW feedline and are realized from low- and high-impedance microstrip transmission lines. The "ground bridge" prevents excitation of the asymmetric slotline mode on the CPW feedline structure. The 4-μm Nb microstrip line uses SiO_2 as a dielectric insulator (0.1-μm thick) from the Mo_2N layer. This transmission line structure is not explicitly used at microwave frequencies but enables millimeter wave coupling to a dual-slot antenna [173]. Right: A simplified cross-sectional view of the coplanar waveguide (top) and microstrip transmission line (bottom) geometries used in modeling the electromagnetic response. The permittivity for the dielectric layers and the permeability for the lines are indicated. The arrows indicate the electric field and its dominant modal symmetry. The microwave dielectric substrate (0.450 ± 0.025 μm thick, 100-mm diameter) is monocrystalline silicon [172]. Adapted from [72].

From Eq. (5.6) and Eq. (5.8) it follows that the effective permittivity and permeability are related by

$$\varepsilon_{r,\mathrm{eff}} = n_{\mathrm{eff}}/Z_n, \quad \mu_{r,\mathrm{eff}} = n_{\mathrm{eff}} \cdot Z_n. \tag{5.9}$$

These scaling relationships between $\varepsilon_{r,\mathrm{eff}}$ and $\mu_{r,\mathrm{eff}}$ were enforced by the algorithm during fitting. The resulting transmission response computed with this methodology [see Eq. (5.12)] agrees with the measured data within 1%, similarly to the accuracy previously found through the evaluation of Eq. (5.3). This analysis approach is analogous to that implemented in [174] to explicitly link the transmission line parameters which depend upon the detailed sample geometry to the interaction of the fields in a homogeneous bulk material sample in an electromagnetically self-consistent manner. For example, a non-physical dielectric function would

be encountered if $\mu_{r,\text{eff}} \equiv 1$ was tacitly adopted for the superconducting material [175, 176].

A parameter of interest for superconducting resonator-based detectors is the kinetic inductance fraction [177], α, which is defined as the ratio of the transmission line's kinetic inductance, $L(\mu_1, \mu_2) - L(\mu_o, \mu_o)$, relative to the total inductance, $L(\mu_1, \mu_2)$. With these definitions and through the use of Eq. (5.7), one obtains:

$$\alpha = 1 - \frac{1}{\mu_{r,\text{eff}}}. \tag{5.10}$$

The results found for α are in quantitative agreement with the values derived from the HFSS simulations (Table III in [72]) and can be found in Table 5.3, where the last significant digit computed in HFSS simulations is indicated with parentheses." [72]

Table 5.3: Transmission line parameter extraction – 2-resonator ABCD-matrix model (Adapted from [72])

Line	$Z_{o,\text{HFSS}}$ [Ω]	Z_o [Ω]	n_{eff} [−]	α [−]
1, low	2.7(0)	2.47 ± 0.01	10.697 ± 0.571	0.898 ± 0.008
1, high	8.5(0)	7.70 ± 0.10	11.143 ± 0.336	0.901 ± 0.007
2, low	2.7(0)	2.47 ± 0.01	10.701 ± 0.162	0.898 ± 0.004
2, high	8.5(0)	7.70 ± 0.03	11.147 ± 0.084	0.901 ± 0.003

5.4 Summary of findings

"This [chapter] presented a methodology to calibrate the transmission response of superconducting microwave resonators at cryogenic temperatures and described two methods to analyze the resulting dataset. The phenomenological and ABCD-matrix methods recovered the measured transmission data with the same 1% level of accuracy, thus providing a numerical validation of the general approach. The derived Q factors in either approach were statistically indistinguishable.

It is interesting to compare the number of parameters required by each method. The first analysis method employs a rational polynomial function of degree k with $2k$ complex and 2 real parameters for each resonator. A second-order function with 6 parameters per resonator

was shown to recover the measured data to within a 1% accuracy. The second method, based upon an analysis of the circuit's distributed network, was implemented via cascaded ABCD matrices. Here, 2 complex and 3 real parameters were necessary to compute the ABCD matrices of each transmission line section used to represent the resonator structure and the feedline. In addition, the line lengths were taken as known and the constraint between the wave impedance and the effective index was enforced in fitting. Broadly speaking the two approaches have comparable underlying complexity.

While the phenomenological model is useful in providing the values of the resonators' central frequencies and widths, the ABCD-matrix method provides insight into the circuit's internal structure when used in conjunction with electromagnetic simulation tools, to make an explicit linkage between the model and the underlying geometric details of the transmission media in use. This approach can be of particular value in extracting the line parameters required for precision circuit design. More importantly, the ABCD-matrix model naturally enables the treatment of distributed transmission line structures without the approximations typically employed in conventional lumped-circuit analysis. The accuracy of these analysis methods exceeds that of a simple lumped-circuit approximation over the frequency span and parameter range experimentally explored." [72]

Appendix: ABCD-matrix model

"The ABCD matrix for a two-port network is defined in terms of the total voltages and currents as follows [65, 178]:

$$\begin{bmatrix} V_{in} \\ I_{in} \end{bmatrix} = \begin{bmatrix} A & B \\ C & D \end{bmatrix} \begin{bmatrix} V_{out} \\ I_{out} \end{bmatrix}. \tag{5.11}$$

The scattering parameter S_{21}, also known as the transmission amplitude, t, can be directly related to the ABCD parameters as [178]:

$$S_{21} = \frac{2Z_l}{AZ_l + B + CZ_lZ_s + DZ_s}, \tag{5.12}$$

where Z_l and Z_s represent the load and source impedances, respectively. The ABCD matrix of the cascade connection of multiple networks is equal to the product of the ABCD matrices representing the individual two-ports, that is

$$\begin{bmatrix} A & B \\ C & D \end{bmatrix} = \prod_i \begin{bmatrix} A_i & B_i \\ C_i & D_i \end{bmatrix}_i . \tag{5.13}$$

Here, the subscript i is used to indicate the different matrices as well as the ABCD parameters of each matrix.

In particular, the ABCD parameters of a two-port circuit represented by a transmission line are [65, 178]:

$$\begin{bmatrix} A & B \\ C & D \end{bmatrix}_{TL} = \begin{bmatrix} \cosh(\gamma l) & Z_o \cdot \sinh(\gamma l) \\ 1/Z_o \cdot \sinh(\gamma l) & \cosh(\gamma l) \end{bmatrix} . \tag{5.14}$$

In Eq. (5.14), Z_o is the characteristic impedance, γ the propagation constant, and l the line length. The determinant of this matrix is unity.

Each resonator is made of a low-, high-, and low-impedance transmission line connected to a coupling capacitor (Fig. 5.5). The resonator's low-impedance transmission line section termination was modeled as an open-circuited line, i.e., $Z_{in,1} = Z_1 \coth(\gamma_1 l_1)$, while the high- and second low-impedance transmission lines were specified by [65]:

$$Z_{in,j} = Z_j \frac{Z_{in,j-1}\cosh(\gamma_j l_j) + Z_j \sinh(\gamma_j l_j)}{Z_{in,j-1}\sinh(\gamma_j l_j) + Z_j \cosh(\gamma_j l_j)}, \quad j = 2, 3. \tag{5.15}$$

Finally, the total impedance as seen through the coupling capacitors is $Z_{tot} = 1/(i\omega C_c) + Z_{in,3}$. Here, the index j specifies the internal lines in the stepped-impedance resonator. The ABCD matrix associated with the complete resonator structure is therefore:

$$\begin{bmatrix} A & B \\ C & D \end{bmatrix}_{res} = \begin{bmatrix} 1 & 0 \\ 1/Z_{tot} & 1 \end{bmatrix} . \tag{5.16}$$

The individual resonators are connected to the feedline via a T-junction at their respective

electrical delays. The following expression,

$$\begin{bmatrix} A & B \\ C & D \end{bmatrix}_{T-junc} = \begin{bmatrix} A & B \\ C & D \end{bmatrix}_{TL} \begin{bmatrix} A & B \\ C & D \end{bmatrix}_{res} \begin{bmatrix} A & B \\ C & D \end{bmatrix}_{TL}, \tag{5.17}$$

allows the resonators to be cascaded with the feedline sections, whose ABCD matrices are expressed through Eq. (5.14). The resulting two-port circuit is used to compute the frequency response of the chip. The wire bonds, transition board, connectors, and coaxial cables between the device reference and the instrument termination planes were added in a similar fashion to investigate the baseline response. For simplicity, we do not explicitly treat the parasitic reactance at the transmission line junctions; however, this detail can readily be incorporated in the formulation and can be of importance at higher frequencies. The complex phase velocity and kinetic inductance fraction of the transmission line configuration employed can be extracted from the response of this composite ABCD-matrix for the system." [72]

Chapter 6

Conclusions

6.1 Thesis summary

This work aims to fill some of the gaps existing in the technology currently employed for far-infrared and submillimeter astronomy by developing μ-Spec, an ultracompact (10–cm^2) spectrometer with ultra-low-noise detectors (NEP $< 10^{-20}$ W/$\sqrt{\text{Hz}}$) integrated on a silicon chip. This dramatic size reduction and increased sensitivity relative to prior art make this instrument a powerful capability for space telescopes and high-altitude ballon-borne payloads operating in the far-IR and microwave regions of the electromagnetic spectrum. μ-Spec can therefore become a unique tool to probe a wide range of environments in the universe and provide answers to fundamental questions regarding galactic, stellar, and planetary formation. In this work, the feasibility of this novel technology was studied with particular regard to its diffractive multimode region and the materials to employ in its transmission lines and detectors.

Chapter 1 offered a general overview of the importance of infrared astrophysics and the need for space telescopes. It is known that much of the visible and ultraviolet light released billions of years ago has been stretched into the far-infrared and microwave region of the electromagnetic spectrum. In addition, many of the objects of interest to astronomers and astrophysicists emit most strongly in the infrared but are obscured to our view by interstellar dust. The uniqueness of infrared instruments lies in the capability of infrared wavelengths

to detect and observe the dust emission, thereby enabling the observation of such astrophysical phenomena otherwise impossible with visible light. Because of the Earth atmosphere's absorption bands, however, most infrared radiation is blocked out and the atmosphere itself emits strongly in the infrared. Space telescopes or high-altitude ballon-borne payloads can get above as much of the atmosphere as possible and enable the exploration of the physical processes in the early universe.

The ability to fully study the far-IR region of the universe has been limited by the size and cost of the cryogenic spectrometers required to carry out these measurements. Chapter 2 presented a comparison between the current state of the art and the technology required to perform this type of science. μ-Spec is proposed as a new technology concept that resolves these issues and can become a powerful capability for several future far-IR and submillimeter missions. The μ-Spec structure and operating principles were presented in detail, describing each of its subsystems. This was followed by the questions concerning the μ-Spec feasibility that this work attempted to answer. The chapter ended with this thesis' objectives and an outline of the entire work.

Chapter 3 addressed the problem of finding low-loss dielectric materials for the transmission line substrates. The dielectric properties of two different amorphous silicon compounds were analyzed and compared with those of single-crystal silicon. Two mathematical models were developed and used to analyze laboratory transmission data of silicon nitride and silicon oxide films. The complex dielectric functions of these two materials were extracted with an accuracy of less than 4% and show that their imaginary parts, representing the loss in the materials, can reach values on the order of 10. In contrast, the loss in single-crystal silicon samples previously analyzed by the same author or found in the literature never exceeds values of 10^{-3}. This makes single-crystal silicon the ideal candidate for the transmission line substrates.

Chapter 4 presented a design methodology developed for the μ-Spec diffractive region, given specific requirements on size and spectral range. This methodology was used to explore the entire design space and find the optimal solutions that maximize the instrument coupling efficiency and minimize the phase error on its focal plane. Five designs were described with

different requirements and performance, the best having four stigmatic points that maximize the utilization of the focal plane with a coupling efficiency close to unity and a spectral resolution of about 260.

Chapter 5 presented analysis and calibration techniques that were elaborated to study the properties of the superconducting materials employed in the instrument transmission lines and detectors. These techniques were applied to cryogenic laboratory data of molybdenum nitride and niobium resonators. The parameters of interest of such resonators, such as the quality factors, central frequencies and widths, and the kinetic inductance fraction, were derived with an accuracy of about 1%.

Finally, this chapter summarizes the thesis and highlights its primary research contributions. Perspectives for future research based on this work are given in the final section.

6.2 Contributions

The specific contributions of this work can be summarized as follows:

1. **Development of an optical design methodology for an ultracompact (10–cm^2) far-IR spectrometer-on-a-chip.** This methodology generates designs for the spectrometer diffractive region given requirements on chip size and spectral range through a two-step optimization process.

    - First, the instrument resolving power is maximized as a function of the spectrometer's operating order and the non-dimensionalized pitch of the internal emitter feed structures. This enables a complete exploration of the design space as a function of these two parameters, which relate to the complexity of the instrument operations and amount of diffraction in its multimode region.
    - Once the desired values of these two parameters are chosen, the optimal values of the design variables can be obtained by optimizing specific figures of merit, such as the RMS phase error.
    - **Generation of 4-stigmatic-point solutions**. By minimizing the RMS phase

error on the focal plane, unprecedented solutions with 4 stigmatic points are found and used to maximize the utilization of the focal plane.

- **Development of a numerically-efficient model for the analysis of the electric field.** A classical phased-array analysis approach is used to calculate the electric field and power distributions within the multimode region. This method is more efficient than electromagnetic simulation tools, whose computational burden can grow rapidly. The multimode region is discretized with a mesh that can easily be adapted to accommodate different instrument shapes and grid densities, depending on the level of accuracy desired for the analysis. The model also enables the computation of the coupling efficiency and beam directivity.

2. **Development of novel analysis and calibration techniques to characterize superconducting resonators.**

   - An *in-situ* calibration procedure is formulated which removes non-ideal instrument artifacts between the device under test and the measurement plane. The transmission data thus calibrated can be analyzed with a phenomenological model to derive the values of the resonators' central frequencies and widths.

   - A transmission line model is assembled through an ABCD-matrix method, which is useful in providing insight into a circuit's internal structure when used with electromagnetic simulation tools. This analysis method enables the treatment of distributed transmission line structures without the approximations adopted in conventional lumped-circuit analysis and with an accuracy that exceeds such approximations over the spectral range explored.

3. **Development, verification, and validation of a mathematical model for the analysis of dielectric materials.** The model enables a recovery of the materials' spectral lines within a 4% accuracy and provides a high-resolution database of infrared dielectric properties of silicon-based materials with applications in instrument microfabrication and optics.

6.3 Future work

This research points to a number of possible future directions. Below are suggestions for follow-on research or applications.

Applications of the dielectric function models to various materials

The mathematical models developed to extract the dielectric functions of silicon-based materials can be used for any dielectric material over a wide range of frequencies. The algorithm developed to implement these models can easily be updated with other models, such as the Drude and Debye models for metals, or to account for dielectric mixtures, i.e., samples made of a number of materials with different filling fractions. In addition, the material's reflection and absorption, as well as other parameters of interest such as the optical constants, can be computed for analysis and interpretation of astrophysical data.

Use of the design tools for different spectrometer concepts

The design methodology developed for μ-Spec can readily be adapted to a variety of circumstances. Some examples are: new size constraints, different wavelength ranges, higher spectral resolutions, etc. In addition, the electric field distribution at the output of the internal phased array can be changed to account for different types of feed structures. This makes this tool versatile and capable of generating multiple designs as well as carrying out trade-off studies with varying parameters.

Applications of the analysis techniques for superconducting resonators

The phenomenological model and ABCD-matrix method can in principle deal with a large number of resonators. The algorithms were also written to optimize computational performance and process large complex datasets or systems of equations. An example of future application of these tools is the analysis of the response of the μ-Spec resonators with a larger number of resolving channels.

Bibliography

[1] J. Byrnes, *Unexploded Ordnance Detection and Mitigation.* Springer, 2009.

[2] International Organization of Standards, "ISO 20743:2007, Optics and photonics – Spectral bands," 2007.

[3] C. Ibarra-Castanedo, *Quantitative subsurface defect evaluation by pulsed phase thermography: depth retrieval with the phase.* PhD thesis, Laval University, 2005.

[4] E. P. Hubble, "The law of red shifts (George Darwin Lecture)," *Monthly Notices of the Royal Astronomical Society*, vol. 113, p. 658, 1953.

[5] G. Hasinger, "X-ray astronomy: Peeking into the obscured Universe," *Nature*, vol. 404, pp. 443–446, 2000.

[6] C. F. Bohren and D. R. Huffman, *Absorption and Scattering of Light by Small Particles.* New York: Wiley, 1983.

[7] E. P. Ney, "Star dust," *Science*, vol. 195, pp. 541–546, 1977.

[8] R. A. Bernstein, W. L. Freedman, and B. F. Madore, "The First Detections of the Extragalactic Background Light at 3000, 5500, and 8000 Å. III. Cosmological Implications," *The Astrophysical Journal*, vol. 571, no. 1, pp. 107–128, 2002.

[9] B. D. Savage and J. S. Mathis, "Observed properties of interstellar dust," *Annual Review of Astronomy and Astrophysics*, vol. 17, pp. 73–111, 1979.

[10] N. C. Wickramasinghe and K. Nandy, "The shape of the interstellar absorption band," *Astrophysics and Space Science*, vol. 6, no. 1, pp. 154–156, 1972.

[11] P. A. Aannestad and E. M. Purcell, "Interstellar grains," *Annual Review of Astronomy and Astrophysics*, vol. 11, pp. 309–362, 1973.

[12] D. R. Huffman, "Interstellar grains: the interaction of light with a small-particle system," *Advances in Physics*, vol. 26, pp. 129–230, 1977.

[13] P. G. Martin, *Cosmic Dust.* Oxford University Press, London, 1978.

[14] K. L. Day and D. R. Huffman, "Measured Extinction Efficiency of Graphite Smoke in the Region 1200-6000 Å," *Nature Physical Science*, vol. 243, pp. 50–51, 1973.

[15] G. H. Herbig, "The diffuse interstellar bands: IV. The region 4400-6850 Å," *The Astrophysical Journal*, vol. 196, no. 1, pp. 129–160, 1975.

[16] T. P. Snow Jr., D. G. York, and D. E. Welty, "Catalogue of diffuse interstellar band measurements," *The Astronomical Journal*, vol. 82, no. 2, pp. 113–128, 1977.

[17] D. P. Gilra, "Collective excitations and dust particles in space," *The Scientific Results from the Orbiting Astronomical Observatory OAO-2*, vol. NASA SP-310, pp. 295–319, 1972.

[18] D. P. Gilra, *Collective excitations in small solid particles and astronomical applications.* PhD thesis, University of Wisconsin, 1972.

[19] K. L. Day, "Further measurements of amorphous silicates," *The Astrophysical Journal*, vol. 210, pp. 614–617, 1976.

[20] W. Krätschmer and D. R. Huffman, "Infrared extinction of heavy ion irradiated and amorphous olivine, with applications to interstellar dust," *Astrophysics and Space Science*, vol. 61, no. 1, pp. 195–203, 1979.

[21] A. Li and B. T. Draine, "Infrared Emission from Interstellar Dust. II. The Diffuse Interstellar Medium," *The Astrophysical Journal*, vol. 554, no. 2, pp. 778–802, 2001.

[22] A. G. G. M. Tielens, S. Hony, C. van Kerckhoven, and E. Peeters, "Interstellar and Circumstellar PAHs," in *The Universe as Seen by ISO* (P. Cox and M. Kessler, eds.), vol. 427 of *ESA Special Publication*, pp. 579–587, Mar 1999.

[23] J. C. B. Papaloizou and C. Terquem, "Planet formation and migration," *Reports on Progress in Physics*, vol. 69, pp. 119–180, 2006.

[24] G. M. Kennedy and S. J. Kenyon, "Planet Formation Around Stars of Various Masses: The Snow Line and the Frequency of Giant Planets," *The Astrophysical Journal*, vol. 673, no. 1, pp. 502–512, 2008.

[25] S. J. Kenyon and B. C. Bromley, "Terrestrial Planet Formation. I. The Transition from Oligarchic Growth to Chaotic Growth," *The Astronomical Journal*, vol. 131, no. 3, pp. 1837–1850, 2006.

[26] J. J. Lissauer, "Planet Formation," *Annual Review of Astronomy and Astrophysics*, vol. 31, pp. 129–174, 1993.

[27] R. E. Kinzer, Jr., S. Rinehart, D. Benford, E. Dwek, R. Henry, J. Nuth, R. Silverberg, C. Wheeler, and E. Wollack, "Optical properties of astronomical silicates with infrared techniques," in *Millimeter, Submillimeter, and Far-Infrared Detectors and Instrumentation for Astronomy V*, vol. 7741 of *Proceedings of SPIE*, pp. 774128–774128–11, 2010.

[28] H. J. Habing and H. Olofsson, *Asymptotic Giant Branch Stars*. Springer, 2004.

[29] V. Zubko, E. Dwek, and R. G. Arendt, "Interstellar dust models consistent with extinction, emission, and abundance constraints," *The Astrophysical Journal Supplement Series*, vol. 152, no. 2, pp. 211–249, 2004.

[30] E. van Dishoeck, "ISO spectroscopy of gas and dust: from molecular clouds to protoplanetary disks," *Annual Review of Astronomy and Astrophysics*, vol. 42, pp. 119–167, 2004.

[31] G. Kirchhoff, "Über das Verhältniss zwischen dem Emissionsvermögen und dem Absorptionsvermögen der Körper für Wärme und Licht," *Annalen der Physik und Chemie*, vol. 109, no. 2, pp. 275–301, 1860.

[32] S. A. Rinehart, D. J. Benford, G. Cataldo, E. Dwek, R. Henry, J. Raymond E. Kinzer, J. Nuth, R. Silverberg, C. Wheeler, and E. Wollack, "Measuring the optical properties of astrophysical dust analogues: instrumentation and methods," *Applied Optics*, vol. 50, no. 21, pp. 4115–4123, 2011.

[33] C. R. Richey, R. E. Kinzer, G. Cataldo, E. J. Wollack, J. A. Nuth, D. J. Benford, R. F. Silverberg, and S. A. Rinehart, "Optical properties of iron silicates in the infrared to millimeter as a function of wavelength and temperature," *The Astrophysical Journal*, vol. 770, no. 1, pp. 46–57, 2013.

[34] T. Sudo, "Short communication: A geometrical approach to the structure of noncrystalline silica precipitates," *Structural Chemistry*, vol. 11, pp. 15–17, 2000.

[35] J. A. Nuth, F. J. M. Rietmeijer, S. L. Hallenbeck, P. A. Withey, and F. Ferguson, "Nucleation, Growth, Annealing and Coagulation of Refractory Oxides and Metals: Recent Experimental Progress and Applications to Astrophysical Systems," *Thermal Emission Spectroscopy and Analysis of Dust, Disks, and Regoliths*, vol. 196, pp. 313–332, 2000.

[36] M. W. Werner, T. L. Roellig, F. J. Low, G. H. Rieke, M. Rieke, W. F. Hoffmann, E. Young, J. R. Houck, B. Brandl, G. G. Fazio, J. L. Hora, R. D. Gehrz, G. Helou, B. T. Soifer, J. Stauffer, J. Keene, P. Eisenhardt, D. Gallagher, T. N. Gautier, W. Irace, C. R. Lawrence, L. Simmons, J. E. Van Cleve, M. Jura, E. L. Wright, and D. P. Cruikshank, "The Spitzer Space Telescope Mission," *The Astrophysical Journal Supplement Series*, vol. 154, no. 1, pp. 1–9, 2004.

[37] R. D. Gehrz, E. E. Becklin, I. de Pater, D. F. Lester, T. L. Roellig, and C. E. Woodward, "A new window on the cosmos: The Stratospheric Observatory for Infrared Astronomy (SOFIA)," *Advances in Space Research*, vol. 44, no. 4, pp. 413–432, 2009.

[38] J. P. Gardner, J. C. Mather, M. Clampin, R. Doyon, M. A. Greenhouse, H. B. Hammel, J. B. Hutchings, P. Jakobsen, S. J. Lilly, K. S. Long, J. I. Lunine, M. J. Mccaughrean, M. Mountain, J. Nella, G. H. Rieke, M. J. Rieke, H.-W. Rix, E. P. Smith, G. Sonneborn, M. Stiavelli, H. S. Stockman, R. A. Windhorst, and G. S. Wright, "The James Webb Space Telescope," *Space Science Reviews*, vol. 123, no. 4, pp. 485–606, 2006.

[39] M. F. Kessler, J. A. Steinz, M. E. Anderegg, J. Clavel, G. Drechsel, P. Estaria, J. Faelker, J. R. Riedinger, A. Robson, B. G. Taylor, and S. Ximénez de Ferrán, "The Infrared Space Observatory (ISO)," *Astronomy & Astrophysics*, vol. 315, no. 2, pp. L21–L27, 1996.

[40] G. L. Pilbratt, J. R. Riedinger, T. Passvogel, G. Crone, D. Doyle, U. Gageur, A. Heras, C. Jewell, L. Metcalfe, S. Ott, and M. Schmidt, "Herschel Space Observatory, an ESA facility for far-infrared and submillimeter astronomy," *Astronomy & Astrophysics*, vol. 518, no. L1, pp. 1–6, 2010.

[41] A. Wootten and A. R. Thompson, "The Atacama Large Millimeter/Submillimeter Array," *Proceedings of the IEEE*, vol. 97, no. 8, pp. 1463–1471, 2009.

[42] J. W. M. Baars, R. N. Martin, J. G. Mangum, J. P. McMullin, and W. L. Peters, "The Heinrich Hertz Telescope and the Submillimeter Telescope Observatory," *Publications of the Astronomical Society of the Pacific*, vol. 111, no. 759, pp. 627–646, 1999.

[43] P. T. P. Ho, J. M. Moran, and K. Y. Lo, "The Submillimeter Array," *The Astrophysical Journal Letters*, vol. 616, no. 1, p. L1, 2004.

[44] J. E. Carlstrom, P. A. R. Ade, K. A. Aird, B. A. Benson, L. E. Bleem, S. Busetti, C. L. Chang, E. Chauvin, H.-M. Cho, T. M. Crawford, A. T. Crites, M. A. Dobbs, N. W. Halverson, S. Heimsath, W. L. Holzapfel, J. D. Hrubes, M. Joy, R. Keisler, T. M. Lanting, A. T. Lee, E. M. Leitch, J. Leong, W. Lu, M. Lueker, D. Luong-Van, J. J. McMahon, J. Mehl, S. S. Meyer, J. J. Mohr, T. E. Montroy, S. Padin, T. Plagge, C. Pryke, J. E. Ruhl, K. K. Schaffer, D. Schwan, E. Shirokoff, H. G. Spieler, Z. Staniszewski, A. A. Stark, C. Tucker, K. Vanderlinde, J. D. Vieira, and R. Williamson, "The 10

Meter South Pole Telescope," *Publications of the Astronomical Society of the Pacific*, vol. 123, no. 903, pp. 568–581, 2011.

[45] Z. Staniszewski, R. Aikin, M. Amiri, S. Benton, C. Bischoff, J. Bock, J. Bonetti, J. Brevik, B. Burger, C. Dowell, L. Duband, J. Filippini, S. Golwala, M. Halpern, M. Hasselfield, G. Hilton, V. Hristov, K. Irwin, J. Kovac, C. Kuo, M. Lueker, T. Montroy, H. Nguyen, I. Ogburn, R.W., R. O?Brient, A. Orlando, C. Pryke, C. Reintsema, J. Ruhl, R. Schwarz, C. Sheehy, S. Stokes, K. Thompson, G. Teply, J. Tolan, A. Turner, A. Vieregg, P. Wilson, D. Wiebe, and C. Wong, "The Keck Array: A Multi Camera CMB Polarimeter at the South Pole," *Journal of Low Temperature Physics*, vol. 167, no. 5-6, pp. 827–833, 2012.

[46] B. Rabii, C. D. Winant, J. S. Collins, A. T. Lee, P. L. Richards, M. E. Abroe, S. Hanany, B. R. Johnson, P. Ade, A. Balbi, J. J. Bock, J. Borrill, R. Stompor, A. Boscaleri, E. Pascale, P. de Bernardis, P. G. Ferreira, V. V. Hristov, A. E. Lange, A. H. Jaffe, C. B. Netterfield, G. F. Smoot, and J. H. P. Wu, "MAXIMA: A balloon-borne cosmic microwave background anisotropy experiment," *Review of Scientific Instruments*, vol. 77, no. 7, pp. 071101–1–25, 2006.

[47] S. Masi, P. D. Bernardis, G. D. Troia, M. Giacometti, A. Iacoangeli, F. Piacentini, G. Polenta, P. A. R. Ade, P. D. Mauskopf, J. J. Bock, J. R. Bond, C. R. Contaldi, D. Pogosyan, S. Prunet, J. Borrill, A. Boscaleri, E. Pascale, K. Coble, P. Farese, T. Montroy, J. E. Ruhl, B. P. Crill, V. V. Hristov, W. C. Jones, A. E. Lange, P. Mason, G. D. Gasperis, P. Natoli, K. Ganga, E. Hivon, N. Vittorio, A. H. Jaffe, L. Martinis, F. Scaramuzzi, A. Melchiorri, C. B. Netterfield, F. Pongetti, and G. Romeo, "The BOOMERanG Experiment and the Curvature of the Universe," *Progress in Particle and Nuclear Physics*, vol. 48, no. 1, pp. 243–261, 2002.

[48] E. Pascale, P. A. R. Ade, J. J. Bock, E. L. Chapin, J. Chung, M. J. Devlin, S. Dicker, M. Griffin, J. O. Gundersen, M. Halpern, P. C. Hargrave, D. H. Hughes, J. Klein, C. J. MacTavish, G. Marsden, P. G. Martin, T. G. Martin, P. Mauskopf, C. B. Netterfield, L. Olmi, G. Patanchon, M. Rex, D. Scott, C. Semisch, N. Thomas, M. D. P. Truch,

C. Tucker, G. S. Tucker, M. P. Viero, and D. V. Wiebe, "The Balloon-borne Large Aperture Submillimeter Telescope: BLAST," *The Astrophysical Journal*, vol. 681, no. 1, pp. 400–414, 2008.

[49] A. Kogut, P. A. R. Ade, D. Benford, C. L. Bennett, D. T. Chuss, J. L. Dotson, J. R. Eimer, D. J. Fixsen, M. Halpern, G. Hilton, J. Hinderks, G. F. Hinshaw, K. Irwin, C. Jhabvala, B. Johnson, J. Lazear, L. Lowe, T. Miller, P. Mirel, S. H. Moseley, S. Rodriguez, E. Sharp, J. G. Staguhn, C. E. Tucker, A. Weston, and E. J. Wollack, "The Primordial Inflation Polarization Explorer (PIPER)," in *Millimeter, Submillimeter, and Far-Infrared Detectors and Instrumentation for Astronomy VI*, vol. 8452 of *Proceedings of SPIE*, pp. 84521J1–11, 2012.

[50] National Research Council of the National Academies, "New Worlds, New Horizons in Astronomy and Astrophysics," 2010. The National Academies Press.

[51] Science Definition Team (SDT) and WFIRST Project, "Wide-Field InfraRed Survey Telescope - Astrophysics Focused Telescope Assets WFIRST-AFTA Final Report," tech. rep., NASA, 2013.

[52] NASA, "http://explorers.gsfc.nasa.gov." Retrieved 2015.

[53] T. Nakagawa, H. Matsuhara, Y. Kawakatsu, and the SPICA Team, "The next-generation infrared space telescope SPICA," in *Space Telescopes and Instrumentation 2012: Optical, Infrared, and Millimeter Wave*, vol. 8442 of *Proceedings of SPIE*, pp. 84420O1–9, 2012.

[54] Cosmic Origins Program Office, "Cosmic Origins Program Annual Technology Report," tech. rep., NASA, 2013.

[55] M. Harwit, "Origins of the Zodiacal Dust Cloud," *Journal of Geophysical Research*, vol. 68, no. 8, pp. 2171–2180, 1963.

[56] R. H. Giese and B. Kneißel, "Three-dimensional models of the zodiacal dust cloud: Ii. compatibility of proposed infrared models," *Icarus*, vol. 82, no. 2, pp. 369–378, 1989.

[57] R. D. Barney, J. J. Bauman, L. D. Feinberg, D. J. Mccleese, U. N. Singh, and H. P. Stahl, "NASA's DRAFT Space Technology Roadmap – Science Instruments, Observatories, and Sensor System Roadmap, Technology Area 08," tech. rep., NASA, 2012.

[58] P. L. Richards, "Bolometers for infrared and millimeter waves," *Journal of Applied Physics*, vol. 76, no. 1, pp. 1–24, 1994.

[59] C. Nones, S. Marnieros, A. Benoit, L. Bergé, A. Bideaud, P. Camus, L. Dumoulin, A. Monfardini, and O. Rigaut, "High-impedance NbSi TES sensors for studying the cosmic microwave background radiation," *Astronomy & Astrophysics*, vol. 548, p. A17, 2012.

[60] G. Rieke, *Detection of light - From the Ultraviolet to the Submillimeter.* Cambridge University Press, Second ed., 2003.

[61] G. Cataldo, W.-T. Hsieh, W.-C. Huang, S. H. Moseley, T. R. Stevenson, and E. J. Wollack, "Micro-Spec: an ultra-compact high-sensitivity spectrometer for far-infrared and submillimeter astronomy," *Applied Optics*, vol. 53, no. 6, pp. 1094–1102, 2014.

[62] S. McHugh, B. Mazin, B. A.and Serfass, K. Meeker, S. R.and O'Brien, R. Duan, R. Raffanti, and D. Werthimer, "A readout for large arrays of Microwave Kinetic Inductance Detectors," *Review of Scientific Instruments*, vol. 83, no. 4, pp. 044702–1–9, 2012.

[63] B. A. Mazin, S. R. Meeker, M. J. Strader, P. Szypryt, D. Marsden, J. C. van Eyken, G. E. Duggan, A. B. Walter, G. Ulbricht, M. Johnson, B. Bumble, K. O'Brien, and C. Stoughton, "ARCONS: A 2024 Pixel Optical through Near-IR Cryogenic Imaging Spectrophotometer," *Publications of the Astronomical Society of the Pacific*, vol. 125, pp. 1348–1361, 2013.

[64] G. Cataldo, S. H. Moseley, E. J. Wollack, W.-T. Hsieh, W.-C. Huang, and T. R. Stevenson, "Optimization of Micro-Spec, an Ultra-Compact High-Performance Spectrometer for Far-Infrared Astronomy," in *Bulletin of the American Astronomical Society*, no. 402.05 in Meeting no. 222, June 2013.

[65] D. M. Pozar, *Microwave Engineering.* John Wiley and Sons, Inc., Fourth ed., 2011.

[66] R. K. Hoffmann, *Handbook of microwave integrated circuits*, ch. 2. Artech House, 1987.

[67] J. Zmuidzinas, "Thermal noise and correlations in photon detection," *Applied Optics*, vol. 42, no. 25, pp. 4989–5008, 2003.

[68] M. W. Pospieszalski, "Extremely Low-Noise Amplification with Cryogenic FETs and HFETs: 1970–2004," *IEEE Microwave Magazine*, vol. 6, no. 3, pp. 62–75, 2005.

[69] M. W. Pospieszalski, "Modeling of noise parameters of MESFET's and MODFET's and their frequency and temperature dependence," *IEEE Transactions on Microwave Theory and Techniques*, vol. 37, no. 9, pp. 1340–1350, 1989.

[70] N. Oukhanski, M. Grajcar, E. Il'ichev, and H.-G. Meyer, "Low noise, low power consumption high electron mobility transistors amplifier, for temperatures below 1 K," *Review of Scientific Instruments*, vol. 74, no. 2, pp. 1145–1146, 2003.

[71] G. Cataldo, "Optical properties of astronomical silicates in the infrared," Master's thesis, Institut Supérieur de l'Aéronautique et de l'Espace - SUPAERO, Politecnico di Milano, Politecnico di Torino, 2010.

[72] G. Cataldo, E. J. Wollack, E. M. Barrentine, A.-D. Brown, S. H. Moseley, and K. U-Yen, "Analysis and calibration techniques for superconducting resonators," *Review of Scientific Instruments*, vol. 86, no. 1, pp. 013103–1–11, 2015.

[73] D. F. Edwards, "Silicon (Si)," in *Handbook of Optical Constants of Solids* (E. D. Palik, ed.), pp. 547–569, Burlington: Academic Press, 1997.

[74] R. Datta, C. Munson, M. Niemack, J. McMahon, J. Britton, E. Wollack, J. Beall, M. Devlin, J. Fowler, P. Gallardo, J. Hubmayr, K. Irwin, L. Newburgh, J. Nibarger, L. Page, M. Quijada, B. Schmitt, S. Staggs, R. Thornton, and L. Zhang, "Large-aperture wide-bandwidth antireflection-coated silicon lenses for millimeter wavelengths," *Applied Optics*, vol. 52, no. 36, pp. 8747–8758, 2013.

[75] G. Cataldo, J. A. Beall, H.-S. Cho, B. McAndrew, M. D. Niemack, and E. J. Wollack, "Infrared dielectric properties of low-stress silicon nitride," *Optics Letters*, vol. 37, no. 20, pp. 4200–4202, 2012.

[76] G. Cataldo, E. J. Wollack, and A.-D. Brown, "Infrared dielectric properties of silicon oxide membranes," *Optics Letters*, in prep.

[77] F. Gervais, "High-temperature infrared reflectivity spectroscopy by scanning interferometry," in *Electromagnetic Waves in Matter* (K. J. Button, ed.), vol. 8 of *Infrared and Millimeter Waves*, pp. 284–287, London: Academic Press, 1983.

[78] A. D. Rakić, A. B. Djurišić, J. M. Elazar, and M. L. Majewski, "Optical properties of metallic films for vertical-cavity optoelectronic devices," *Applied Optics*, vol. 37, no. 22, pp. 5271–5283, 1998.

[79] T. S. Eriksson, S. Jiang, and C. G. Granqvist, "Dielectric function of sputter-deposited silicon dioxide and silicon nitride films on the thermal infrared," *Applied Optics*, vol. 24, no. 6, pp. 745–746, 1985.

[80] E. A. Taft, "Characterization of Silicon Nitride Films," *Journal of the Electrochemical Society*, vol. 118, no. 8, pp. 1341–1346, 1971.

[81] H. R. Philipp, "Silicon Nitride (Si_3N_4) (Noncrystalline)," in *Handbook of Optical Constants of Solids* (E. D. Palik, ed.), pp. 771–774, Burlington: Academic Press, 1997.

[82] D. J. Goldie, A. V. Velichko, D. M. Glowacka, and S. Withington, "Ultra-low-noise MoCu transition edge sensors for space applications," *Journal of Applied Physics*, vol. 109, no. 8, pp. 084507–1–9, 2011.

[83] G. Wang, V. Yefremenko, V. Novosad, A. Datesman, J. Pearson, R. Divan, C. L. Chang, L. Bleem, A. T. Crites, J. Mehl, T. Natoli, J. McMahon, J. Sayre, J. Ruhl, S. S. Meyer, and J. E. Carlstrom, "Thermal Properties of Silicon Nitride Beams Below One Kelvin," *IEEE Transactions on Applied Superconductivity*, vol. 21, no. 3, pp. 232–235, 2011.

[84] J. M. Martinis, K. B. Cooper, R. McDermott, M. Steffen, M. Ansmann, K. D. Osborn, K. Cicak, S. Oh, D. P. Pappas, R. W. Simmonds, and C. C. Yu, "Decoherence in Josephson Qubits from Dielectric Loss," *Physical Review Letters*, vol. 95, no. 21, pp. 210503–1–4, 2005.

[85] H. Paik and K. D. Osborn, "Reducing quantum-regime dielectric loss of silicon nitride for superconducting quantum circuits," *Applied Physics Letters*, vol. 96, no. 7, pp. 072505–1–3, 2010.

[86] C. C. Kim, J. W. Garland, H. Abad, and P. M. Raccah, "Modeling the optical dielectric function of semiconductors: Extension of the critical-point parabolic-band approximation," *Physical Reviews B*, vol. 45, no. 20, pp. 11749–11767, 1992.

[87] P. Yeh, *Optical waves in layered media*, pp. 102–111. New York: John Wiley & Sons, Inc., 1988.

[88] M. C. Biggs, "Constrained Minimization Using Recursive Quadratic Programming," in *Towards Global Optimization* (L. C. W. Dixon and G. P. Szergo, eds.), pp. 341–349, North-Holland, 1975.

[89] M. J. D. Powell, "Variable Metric Methods for Constrained Optimization," in *Mathematical Programming: The State of the Art* (M. G. A. Bachem and B. Korte, eds.), pp. 288–311, Springer Verlag, 1983.

[90] L. D. Landau and E. M. Lifshitz, *Electrodynamics of Continuous Media*, vol. 8, pp. 253–262. Pergamon Press, 1960.

[91] A. V. Tikhonravov, P. W. Baumeister, and K. V. Popov, "Phase properties of multilayers," *Applied Optics*, vol. 36, no. 19, pp. 4382–4392, 1997.

[92] M. Mori and T. Ooura, "Double Exponential Formulas for Fourier Type Integrals with a Divergent Integrand," in *Applicable Analysis*, vol. 2, pp. 301–308, World Scientific Series, 1993.

[93] R. Nitsche and T. Fritz, "Determination of model-free Kramers-Kronig consistent optical constants of thin absorbing films from just one spectral measurement: Application to organic semiconductors," *Physical Review B*, vol. 70, no. 19, pp. 195432–1–14, 2004.

[94] W. H. Press, S. A. Teukolsky, W. T. Vetterling, and B. P. Flannery, *Numerical Recipes - The Art of Scientific Computing*, pp. 799–806. Cambridge University Press, 2007.

[95] R. Kitamura, L. Pilon, and M. Jonasz, "Optical constants of silica glass from extreme ultraviolet to far infrared at near room temperature," *Applied Optics*, vol. 46, no. 33, pp. 8118–8133, 2007.

[96] H. A. Rowland, "On concave gratings for optical purposes," *Philosophical Magazine*, vol. 16, no. 99, pp. 197–210, 1883.

[97] H. W. Yen, H. R. Friedrich, R. J. Morrison, and G. L. Tangonan, "Planar Rowland spectrometer for fiber-optic wavelength demultiplexing," *Optics Letters*, vol. 6, no. 12, pp. 639–641, 1981.

[98] R. März and C. Cremer, "On the Theory of Planar Spectrographs," *Journal of Lightwave Technology*, vol. 10, no. 12, pp. 2017–2022, 1992.

[99] M. Wu and Y. J. Chen, "Design Considerations for Rowland Circle Gratings Used in Photonic Integrated Devices for WDM Applications," *Journal of Lightwave Technology*, vol. 12, no. 11, pp. 1939–1942, 1994.

[100] P. Muñoz, D. Pastor, J. Capmany, and A. Martínez, "Geometrical optimization of the transmission and dispersion properties of arrayed waveguide gratings using two stigmatic point mountings," *Optics Express*, vol. 11, no. 19, pp. 2425–2432, 2003.

[101] C. M. Bradford, "Direct-Detection Spectroscopy at the CSO with Z-Spec and ZEUS - Probing galaxies near and far with new bolometers-based grating spectrometers," 2008.

[102] B. J. Naylor, *Broadband Millimeter-Wave Spectroscopy with Z-Spec: An Unbiased Molecular-Line Survey of the Starburst Galaxy M82.* PhD thesis, California Institute of Technology, 2008.

[103] C. M. Bradford, B. J. Naylor, J. Zmuidzinas, J. J. Bock, J. Gromke, H. Nguyen, M. Dragovan, M. Yun, L. Earle, J. Glenn, H. Matsuhara, P. A. R. Ade, and L. Duband, "WaFIRS, a waveguide far-IR spectrometer: enabling spectroscopy of high-z galaxies in the far-IR and submillimeter," in *IR Space Telescopes and Instruments*, vol. 4850 of *Proceedings of SPIE*, pp. 1137–1148, 2003.

[104] C. M. Bradford, P. A. R. Ade, J. Aguirre, J. J. Bock, L. Duband, L. Earle, J. Glenn, H. Matsuhara, B. J. Naylor, H. Nguyen, M. Yun, and J. Zmuidzinas, "Z-Spec: a broadband millimeter-wave grating spectrometer - design, construction, and first cryogenic measurements," in *Millimeter and Submillimeter Detectors for Astronomy II*, vol. 5498 of *Proceedings of SPIE*, pp. 257–267, 2004.

[105] L. Earle, P. A. R. Ade, J. Aguirre, R. Aikin, J. Battle, J. J. Bock, C. M. Bradford, M. Dragovan, L. Duband, J. Glenn, G. Griffin, V. Hristov, P. Maloney, H. Matsuhara, B. J. Naylor, H. Nguyen, M. Yun, and J. Zmuidzinas, "Z-Spec: a broadband, direct-detection, millimeter-wave spectrometer - instrument status and first results," in *Millimeter and Submillimeter Detectors and Instrumentation for Astronomy III*, vol. 6275 of *Proceedings of SPIE*, pp. 1–9, 2006.

[106] C. M. Bradford, M. Kenyon, W. Holmes, J. Bock, T. Koch, and the BLISS study team, "Sensitive far-IR survey spectroscopy: BLISS for SPICA," in *Millimeter and Submillimeter Detectors and Instrumentation for Astronomy IV*, vol. 7020 of *Proceedings of SPIE*, pp. 70101O1–12, 2008.

[107] W. Rotman and R. F. Turner, "Wide-Angle Microwave Lens for Line Source Applications," *IEEE Transactions on Antennas and Propagation*, vol. 11, no. 6, pp. 623–632, 1963.

[108] T. Katagi, S. Mano, and S. I. Sato, "An Improved Design Method of Rotman Lens Antennas," *IEEE Transactions on Antennas and Propagation*, vol. AP-32, no. 5, pp. 524–527, 1984.

[109] R. C. Hansen, "Design Trades for Rotman Lenses," *IEEE Transactions on Antennas and Propagation*, vol. 39, no. 4, pp. 464–472, 1991.

[110] C. M. Rappaport and A. I. Zaghloul, "Multifocal Bootlace Lens Design Concepts: a Review," in *IEEE Antennas and Propagation Society International Symposium*, vol. 2B of *Institute of Electrical and Electronics Engineers (IEEE)*, pp. 39–42, 2005.

[111] A. Kovács, P. S. Barry, C. M. Bradford, G. Chattopadhyay, P. Day, S. Doyle, S. Hailey-Dunsheath, M. Hollister, C. McKenney, H. G. LeDuc, N. Llombart, D. P. Marrone, P. Mauskopf, R. C. O'Brient, S. Padin, L. J. Swenson, and J. Zmuidzinas, "SuperSpec: design concept and circuit simulations," in *Millimeter, Submillimeter, and Far-Infrared Detectors and Instrumentation for Astronomy VI*, vol. 8452 of *Proceedings of SPIE*, pp. 84522G1–10, 2012.

[112] E. Shirokoff, P. S. Barry, C. M. Bradford, G. Chattopadhyay, P. Day, S. Doyle, S. Hailey-Dunsheath, M. I. Hollister, A. Kovács, H. G. Leduc, C. McKenney, P. Mauskopf, R. O'Brient, S. Padin, T. Reck, L. J. Swenson, C. E. Tucker, and J. Zmuidzinas, "Design and Performance of SuperSpec: An On-Chip, KID-based, mm-Wavelength Spectrometer," *Journal of Low Temperature Physics*, vol. 176, no. 5-6, pp. 657–662, 2014.

[113] S. Hailey-Dunsheath, P. S. Barry, C. M. Bradford, G. Chattopadhyay, P. Day, S. Doyle, M. Hollister, A. Kovacs, H. G. LeDuc, N. Llombart, P. Mauskopf, C. McKenney, R. Monroe, H. T. Nguyen, R. O'Brient, S. Padin, T. Reck, E. Shirokoff, L. Swenson, C. E. Tucker, and J. Zmuidzinas, "Optical Measurements of SuperSpec: A Millimeter-Wave On-Chip Spectrometer," *Journal of Low Temperature Physics*, vol. 176, no. 5-6, pp. 841–847, 2014.

[114] A. Endo, P. van der Werf, R. M. J. Janssen, P. J. de Visser, T. M. Klapwijk, J. J. A. Baselmans, L. Ferrari, A. M. Baryshev, and S. J. C. Yates, "Design of an Integrated Filterbank for DESHIMA: On-Chip Submillimeter Imaging Spectrograph Based on Superconducting Resonators," *Journal of Low Temperature Physics*, vol. 167, no. 3-4, pp. 341–346, 2012.

[115] A. Endo, C. Sfiligoj, S. J. C. Yates, J. J. A. Baselmans, D. J. Thoen, S. M. H. Javadzadeh, P. P. van der Werf, A. M. Baryshev, and T. M. Klapwijk, "On-chip filter bank spectroscopy at 600-700 GHz using NbTiN superconducting resonators," *Applied Physics Letters*, vol. 103, p. 032601, 2013.

[116] C. N. Thomas, S. Withington, R. Maiolino, D. J. Goldie, E. de Lera Acedo, J. Wagg, R. Blundell, S. Paine, and L. Zeng, "The CAMbridge Emission Line Surveyor (CAMELS)," *ArXiv e-prints*, 2014.

[117] S. Bryan, G. Che, C. Groppi, P. Mauskopf, and M. Underhill, "A compact filter-bank waveguide spectrometer for millimeter wavelengths," *arXiv preprint arXiv:1502.02735*, 2015.

[118] F. W. Gembicki, *Vector Optimization for Control with Performance and Parameter Sensitivity Indices.* PhD thesis, Case Western Reserve University, Cleveland, Ohio, 1974.

[119] A. R. Kerr, "Surface Impedance of Superconductors and Normal Conductors in EM Simulators," Millimeter Array (MMA) Technical Report 245, National Radio Astronomy Observatory, January 1999.

[120] R. E. Collin, *Foundations for Microwave Engineering*, ch. 5.19, pp. 383–386. McGraw-Hill, 1992.

[121] R. P. Hecken, "A near-optimum matching section without discontinuities," *IEEE Transactions on Microwave Theory and Techniques*, vol. 20, no. 11, pp. 734–739, 1972.

[122] G. Matthaei, L. Young, and E. M. T. Jones, *Microwave Filters, Impedance-Matching Networks and Coupling Structures*, pp. 290–291. McGraw-Hill, 1964.

[123] S. Silver, *Microwave Antenna Theory and Design*, pp. 439–448, 453–457. McGraw-Hill, 1949.

[124] S. H. Moseley, E. J. Wollack, and G. Hinshaw, "Limits to the Efficiency of Imaging Systems," in *Proceedings of the far-infrared, sub-mm, and mm Detector Technology*

Workshop (J. Wolf, J. Farhoomand, and C. R. McCreight, eds.), vol. NASA/CP-211408, pp. 388–391, 2002.

[125] J. C. Mather, "Broad-band flared horn with low sidelobes," *IEEE Transactions on Antennas and Propagation*, vol. 29, no. 6, pp. 967–969, 1981.

[126] J. C. Slater and N. H. Frank, *Introduction to Theoretical Physics*, p. 317. McGraw-Hill, 1933.

[127] G. Cataldo, W.-T. Hsieh, W.-C. Huang, S. H. Moseley, T. R. Stevenson, and E. J. Wollack, "Micro-Spec: an integrated direct-detection spectrometer for far-infrared space telescopes," in *Space Telescopes and Instrumentation 2014: Optical, Infrared, and Millimeter Wave*, vol. 9143 of *Proceedings of SPIE*, pp. 91432C1–9, 2014.

[128] G. L. Nehmauser and L. A. Wolsey, *Integer and Combinatorial Optimization.* New York, NY, USA: Wiley-Interscience, 1988.

[129] A. Wächter and L. T. Biegler, "On the Implementation of a Primal-Dual Interior-Point Filter Line-Search Algorithm for Large-Scale Nonlinear Programming," *Mathematical Programming*, vol. 106, no. 1, pp. 25–57, 2006.

[130] E. Balas, S. Ceria, and G. Cornuéjols, "Mixed 0-1 Programming by Lift-and Project in a Branch-and-Cut Framework," *Management Science*, vol. 42, no. 9, pp. 1229–1246, 1996.

[131] A. W. Rudge and M. J. Withers, "New technique for beam steering with fixed parabolic reflectors," in *Reflector Antennas* (A. W. Love, ed.), vol. 118 of *Proceedings of IEE*, pp. 857–863, 1971.

[132] G. Cataldo, S. H. Moseley, and E. J. Wollack, "A four-pole power-combiner design for far-infrared and submillimeter spectroscopy," *Acta Astronautica*, accepted.

[133] R. Fletcher, *Practical Methods of Optimization.* Hoboken, NJ: Wiley, 2013.

[134] J. Ruze, "Antenna Tolerance Theory – A Review," *Proceedings of the IEEE*, vol. 54, no. 4, pp. 633–640, 1966.

[135] R. C. Hansen, *Phased Array Antennas*, p. 15. Wiley, 1998.

[136] P. K. Day, H. G. LeDuc, B. A. Mazin, A. Vayonakis, and J. Zmuidzinas, "A broadband superconducting detector suitable for use in large arrays," *Nature*, vol. 425, pp. 817–821, 2003.

[137] B. Mazin, *Microwave Kinetic Inductance Detectors*. PhD thesis, California Institute of Technology, Pasadena, California, 2005.

[138] W. D. Oliver and P. B. Welander, "Materials in superconducting quantum cubits," *MRS Bulletin*, vol. 38, no. 10, pp. 816–825, 2013.

[139] M. Von Schickfus and S. Hunklinger, "Saturation of the dielectric absorption of vitreous silica at low temperatures," *Physics Letters*, vol. 64A, no. 1, pp. 144–146, 1977.

[140] J. Zmuidzinas, "Superconducting Microresonators: Physics and Applications," *Annual Review of Condensed Matter Physics*, vol. 3, pp. 169–214, 2012.

[141] R. Vijay, D. H. Slichter, and I. Siddiqi, "Observation of Quantum Jumps in a Superconducting Artificial Atom," *Physical Review Letters*, vol. 106, no. 11, pp. 110502–1–4, 2011.

[142] J. Krupka, K. Derzakowski, M. Tobar, J. Hartnett, and R. G. Geyer, "Complex permittivity of some ultralow loss dielectric crystals at cryogenic temperatures," *Measurement Science and Technology*, vol. 10, no. 5, pp. 387–392, 1999.

[143] D. E. Oates, A. C. Anderson, and P. M. Mankiewich, "Measurement of the Surface Resistance of $YBa_2Cu_3O_{7-x}$ Thin Films Using Stripline Resonators," *Journal of Superconductivity*, vol. 3, no. 3, pp. 251–259, 1990.

[144] P. J. Petersan and S. M. Anlage, "Measurement of resonant frequency and quality factor of microwave resonator: Comparison of methods," *Journal of Applied Physics*, vol. 84, no. 6, pp. 3392–3402, 1998.

[145] I. J. Bahl, *Lumped Elements for RF and Microwave Circuits*. Artech House, 2003.

[146] J. Gao, *The Physics of Superconducting Microwave Resonators.* PhD thesis, California Institute of Technology, Pasadena, California, 2008.

[147] M. S. Khalil, M. J. A. Stoutimore, F. C. Wellstood, and K. D. Osborn, "An analysis method for asymmetric resonator transmission applied to superconducting devices," *Journal of Applied Physics*, vol. 111, no. 5, pp. 054510–1–6, 2012.

[148] K. Geerlings, S. Shankar, E. Edwards, L. Frunzio, and M. H. Devoret, "Improving the quality factor of microwave compact resonators by optimizing their geometrical parameters," *Applied Physics Letters*, vol. 100, no. 19, pp. 192601–1–3, 2012.

[149] A. Megrant, C. Nelli, R. Barends, B. Chiaro, Y. Chen, L. Feigt, J. Kelly, E. Lucero, M. Mariantoni, P. J. J. O'Malley, D. Sank, A. Vainsencher, J. Wenner, T. C. White, Y. Yin, C. J. Zhao, J. Palmstrom, J. M. Martinis, and A. N. Cleland, "Planar superconducting resonators with internal quality factors above one million," *Applied Physics Letters*, vol. 100, no. 11, pp. 113510–1–4, 2012.

[150] M. O. C. Deng and A. Lupascu, "An analysis method for transmission measurements of superconducting resonators with applications to quantum-regime dielectric-loss measurements," *Journal of Applied Physics*, vol. 114, no. 5, pp. 054504–1–11, 2013.

[151] L. J. Swenson, P. K. Day, B. H. Eom, H. G. Leduc, N. Llombart, C. M. McKenney, O. Noroozian, and J. Zmuidzinas, "Operation of a titanium nitride superconducting microresonator detector in the nonlinear regime," *Journal of Applied Physics*, vol. 113, no. 10, pp. 104501–1–9, 2013.

[152] Z. Ma, "PhD thesis (Ginzton Labs Report No. 5298)." Stanford University, California, 1995.

[153] H. J. Snortland, "PhD thesis (Ginzton Labs Report No. 5552)." Stanford University, California, 1997.

[154] U. Fano, "Sullo spettro di assorbimento dei gas nobili presso il limite dello spettro d'arco," *Il Nuovo Cimento*, vol. 12, no. 3, pp. 154–161, 1935.

[155] U. Fano, "Effects of Configuration Interaction on Intensities and Phase Shifts," *Physical Review*, vol. 124, no. 6, pp. 1866–1878, 1961.

[156] M. V. Marquezini, P. Kner, S. Bar-Ad, J. Tignon, and D. S. Chemla, "Density dependence of the spectral dielectric function across a Fano resonance," *Physical Review B*, vol. 57, no. 7, pp. 3745–3748, 1998.

[157] R. Singh, I. Al-Naib, W. Cao, C. Rockstuhl, M. Koch, and W. Zhang, "The Fano Resonance in Symmetry Broken Terahertz Metamaterials," *IEEE Transactions on Terahertz Science and Technology*, vol. 3, no. 6, pp. 820–826, 2013.

[158] V. Giannini, Y. Francescano, H. Amrania, C. C. Phillips, and S. A. Maier, "Fano Resonances in Nanoscale Plasmonic Systems: A Parameter-Free Modeling Approach," *Nano Letters*, vol. 11, pp. 2835–2840, 2011.

[159] P. I. Somlo, J. D. Hunter, and I. of Electrical Engineers, *Microwave Impedance Measurement*, vol. 2 of *IEE Electrical Measurement Series*, pp. 25–31. Peter Peregrinus Limited, 1985.

[160] A. H. Zemanian, "An N-Port Realizability Theory Based on the Theory of Distributions," *IEEE Transactions on Circuit Theory*, vol. 10, no. 2, pp. 265–274, 1963.

[161] J. S. Toll, "Causality and the Dispersion Relation: Logical Foundations," *Physical Review*, vol. 104, no. 6, pp. 1760–1770, 1956.

[162] J. D. Jackson, *Classical Electrodynamics*, ch. 8.8. Wiley, 1975.

[163] S. Probst, F. B. Song, P. A. Bushev, A. V. Ustinov, and M. Weides, "Efficient and robust analysis of complex scattering data under noise in microwave resonators," 2014.

[164] T. F. Coleman and Y. Li, "An Interior, Trust Region Approach for Nonlinear Minimization Subject to Bounds," *SIAM Journal on Optimization*, vol. 6, no. 2, pp. 418–445, 1996.

[165] T. F. Coleman and Y. Li, "On the Convergence of Reflective Newton Methods for Large-Scale Nonlinear Minimization Subject to Bounds," *Mathematical Programming*, vol. 67, no. 2, pp. 189–224, 1994.

[166] D. Kajfez and E. J. Hwan, "Q-Factor Measurement with Network Analyzer," *IEEE Transactions on Microwave Theory and Techniques*, vol. 32, no. 7, pp. 666–670, 1984.

[167] A. J. Canos, J. M. Catala-Civera, F. L. Penaranda-Foix, and E. Reyes-Davo, "A Novel Technique for Deembedding the Unloaded Resonance Frequency From Measurements of Microwave Cavities," *IEEE Transactions on Microwave Theory and Techniques*, vol. 54, no. 8, pp. 3407–3416, 2006.

[168] R. F. Bauer and P. Penfield, "De-Embedding and Unterminating," *IEEE Transactions on Microwave Theory and Techniques*, vol. 22, no. 3, pp. 282–288, 1974.

[169] A. Vayonakis, C. Luo, H. G. Leduc, R. Schoelkopf, and J. Zmuidzinas, "The millimeter-wave properties of superconducting microstrip lines," *AIP Conference Proceedings*, vol. 605, no. 1, pp. 539–542, 2002.

[170] T. M. Weller, L. P. Katehi, and G. M. Rebeiz, "A 250-GHz Microshield Bandpass Filter," *IEEE Microwave and Guided Wave Letters*, vol. 5, no. 5, pp. 153–155, 1995.

[171] R. F. Harrington, *Field Computation by Moment Methods*, ch. 5. IEEE Press, 1993.

[172] Soitec, "Smart Cut Silicon-On-Insulator (SOI) wafer," 2014.

[173] A. Patel, A.-D. Brown, W.-T. Hsieh, T. R. Stevenson, S. H. Moseley, K. U-Yen, N. Ehsan, E. M. Barrentine, G. Manos, and E. J. Wollack, "Fabrication of MKIDs for the MicroSpec Spectrometer," *IEEE Transactions on Applied Superconductivity*, vol. 23, no. 3, pp. 2400404–1–4, 2013.

[174] D. T. Chuss, E. J. Wollack, R. Henry, H. Hui, A. J. Juarez, M. Krejny, S. H. Moseley, and G. Novak, "Properties of a variable-delay polarization modulator," *Applied Optics*, vol. 51, no. 2, pp. 197–208, 2012.

[175] K. K. Mei and G.-C. Liang, "Electromagnetics of Superconductors," *IEEE Transactions on Microwave Theory and Techniques*, vol. 39, no. 9, pp. 1545–1552, 1991.

[176] Z.-Y. Shen, *High Temperature Superconducting Microwave Circuits*, sec. 3.3.3. Boston, Massachusetts: Artech House, 1994.

[177] A. Porch, P. Mauskopf, S. Doyle, and C. Dunscombe, "Calculation of the Characteristics of Coplanar Resonators for Kinetic Inductance Detectors," *IEEE Transactions on Applied Superconductivity*, vol. 15, no. 2, pp. 552–555, 2005.

[178] P. F. Goldsmith, *Quasioptical Systems: Gaussian Beam Quasioptical Propagation and Applications*, pp. 231–235. IEEE Press, 1998.